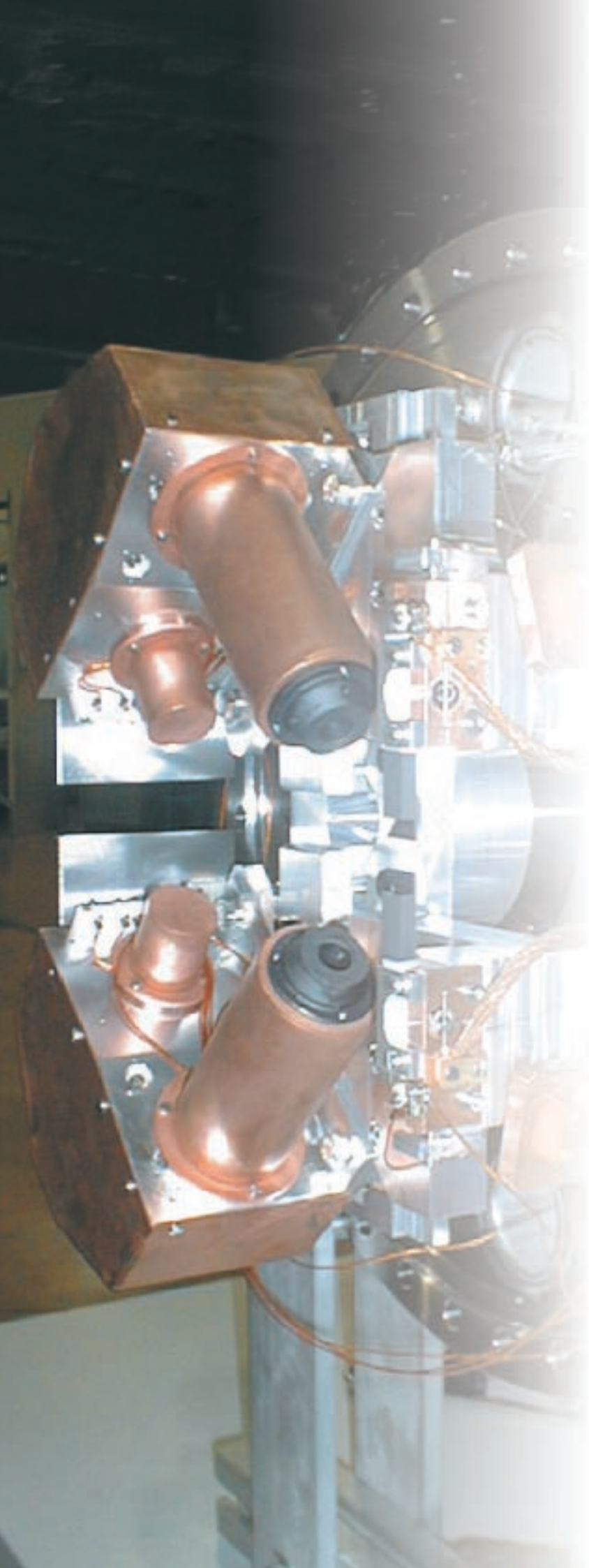

ELETTRA
HIGHLIGHTS
1999 - 2000

Printing & Graphic Design
Tipografia Alabarda, Trieste

HIGHLIGHTS 1999-2000

TABLE OF CONTENTS

Introduction

I am pleased to introduce one more edition of the Elettra Highlights, and I wish to thank all the Elettra staff members, the members of the associated research groups and the users of the facility who contributed to this report.

The scientific and technical achievements reported here cover a wide range of scientific disciplines. It is easy to notice that, in keeping with a world wide trend, life sciences are taking a larger and larger role in the use of the Elettra synchrotron light. Partly as a response to this growing demand, it was decided to operate the machine at 2.4 GeV during a significant fraction of the beam time, and also to launch the construction of a second crystallography beamline, which is now well under way. Nonetheless, activities in surface physics, atomic and molecular physics, photoemission spectroscopy and spectromicroscopy are also expanding. This overall output increase is explained by the opening of new beamlines. This growth of the facility was made possible, to a large extent, by the partnership with Italian and foreign research institutions, to which we are grateful for the concrete display of confidence and enthusiasm for Elettra represented by their investment of financial and human resources.

The new beamlines expand the possibilities of Elettra in several directions, some which were already present, and some which are new.

The field of electronic structure and magnetism is an example of vigorous growth, with the Circular Polarisation beamline (built in collaboration with CNR, the Italian National Research Council) leaving the commissioning phase and starting its operation, and the APE, BACH and XMOSS beamlines, financed by INFM, the Italian National Institute for the Physics of Matter, entering into commissioning. The first three are powered by variable polarisation insertion devices, the last is on a bending magnet source, and they altogether provide access to different dichroic spectroscopies. We therefore anticipate a surge of activity in the area of magnetism and of the electronic properties of strongly correlated systems, which are one of the most challenging frontiers of condensed matter research.

At the same time, the area of absorption spectroscopy, both in the VUV and soft x-ray regime and in the harder x-ray XAFS mode, is starting at Elettra with the Materials Science beamline (in partnership with the Czech Academy of Science) which is already in an advanced stage of commissioning, with the already mentioned XMOSS, and with the XAFS beamline. We hope that absorption spectroscopy, a research tool traditionally popular among Italian synchrotron users, will attract a large number of physicists, chemists, geologists and industrial scientists.

The new Nanospectroscopy beamline is a powerful multi-technique tool for the analysis of surfaces and nanostructures. It replaces and by far improves the LEEM-PEEM microscope of the University of Clausthal, which produced an impressive array of results during its stay at Elettra.

The list of newcomers includes two bending magnet beamlines in the commissioning phase with a strong applied and technological character: they are devoted to microfabrication techniques, one to proximity photolithography (LILIT, financed by INFM) and one to deep lithography. We intend to expand the contacts already established within a strategy of active promotion of development projects in collaboration with industrial users.

There is every reason to expect that this effective doubling of the number of available beamlines, and the high quality of the instrumentation will attract a large number of new users. We try to make their stay at Elettra not only scientifically productive, but also as comfortable and problem-free as possible. While a few rooms on site have recently been made available for "emergency" accommodation of users and visitors, our goal still is to provide cheap and efficient accommodation for most of them within walking distance of the facility. Efforts are also being made to accelerate and streamline the procedure for the reimbursement of our European users' expenses.

A quantitatively and qualitatively strong user community is one of the three pillars on which the success of a synchrotron source rests. The other two are a state-of-the art machine and instrumentation, and a vigorous and productive in-house research program (without which, in my opinion, neither of the other two can be achieved and maintained).

The objective of securing a machine with state of-the-art performance is being pursued first of all by optimising and intensifying all preventive and routine maintenance operations which are needed to preserve the performance of equipment as time goes by (at the rate of 5 000 to 6 000 hours of operation per year!). But just to keep the original performances from degrading is by far not enough, in the fast moving world of synchrotron light sources. There are therefore ambitious projects under way, such as the new full-energy injection system. The Council of Sincrotrone Trieste recently authorised the first financial commitments for the booster synchrotron. Further important projects aiming at improved beam stability are shortly described in these Highlights.

As to the development of a vigorous in-house research program, the most important action is the continuing recruitment of scientific personnel, pursued by Elettra, through open international competition, and by the associated research groups. At a time when government authorities and the media are deprecating the ongoing "brain drain" of talented Italian scientists to foreign laboratories, Elettra is definitely at variance with respect to this general trend. Not only it has been possible to convince many brilliant Italian scientists to return home from Europe or the US, but in several instances foreign scientists (from Germany, France, Austria, etc.) have accepted positions at Elettra, attracted by the opportunity to work with this extraordinary instrument. This is for us a reason for encouragement and a challenge to keep the facility in the forefront of research for years to come.

Furthermore, every possible step has been taken to optimise the collaboration and synergy between the Elettra and the associated research groups, as well as with the other Trieste research institutions, in the pursuit of common scientific objectives.

I hope the readers will find these "Highlights" interesting and pleasant to read.

Massimo Altarelli

Research Highlights

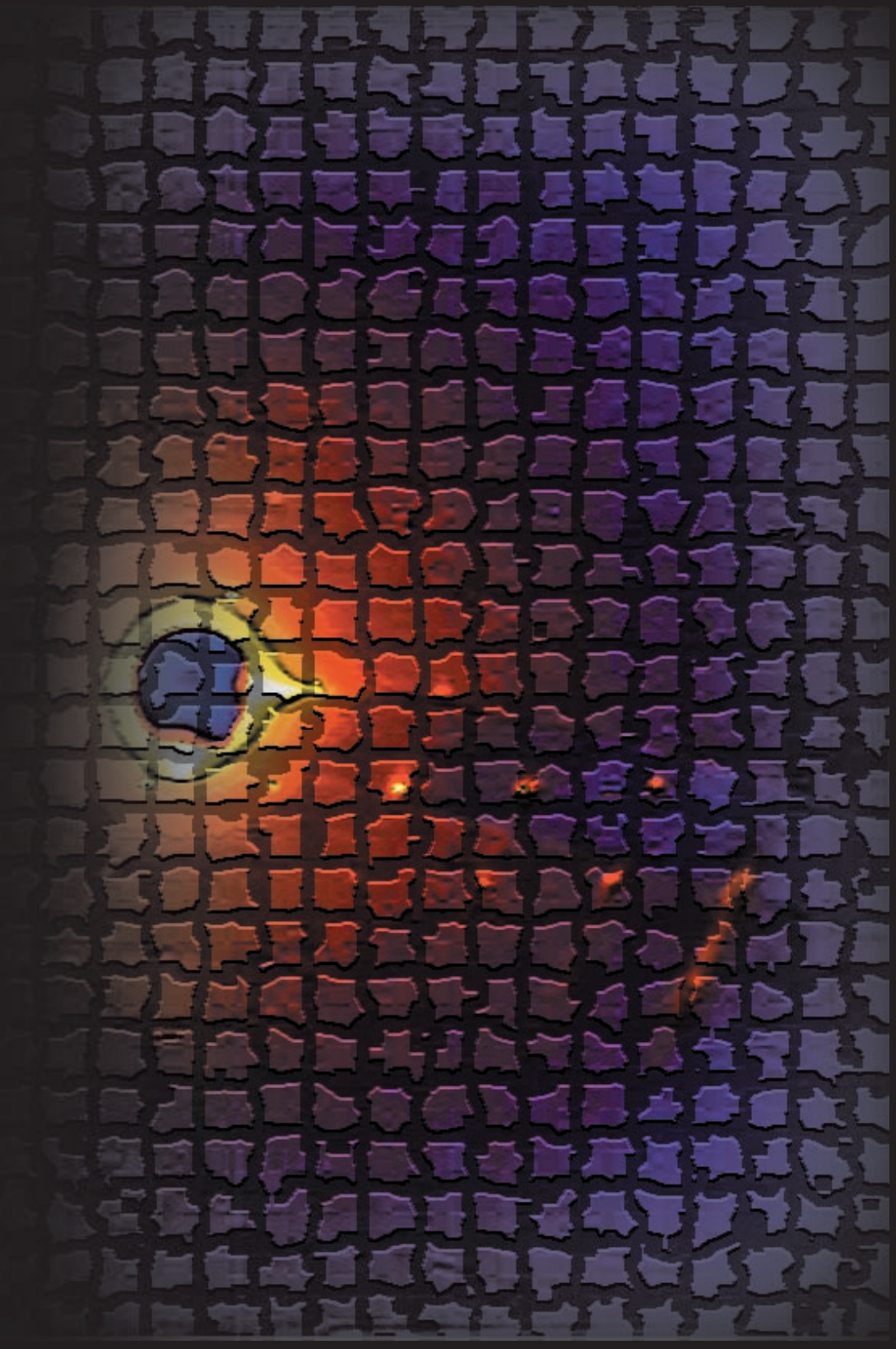

Biomedical Sciences

Materials and Surfaces

Structural Studies

Electronic Structure of Surfaces

Atomic Physics

Magnetic Systems

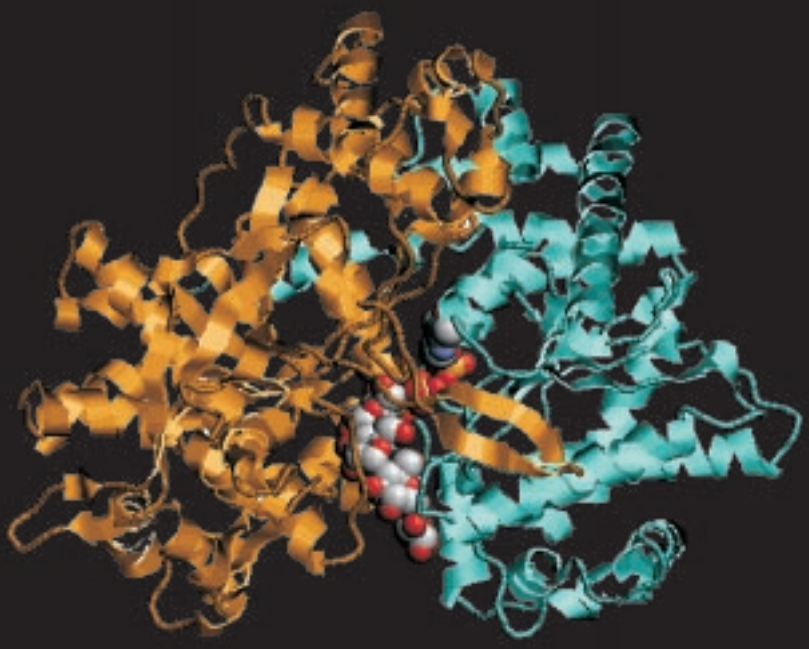

Biomedical Sciences

Native and bromine-modified 5S rRNA minihelices: crystal data in comparison

Marco Vallazza, Corinna Lippmann, Volker A. Erdmann,
Freie Universität Berlin, Institut für Biochemie, Thielallee 63, 14195 Berlin, Germany

Sankaran Banumathi, Markus Perbandt, Christian Betzel,
Institut für Physiologische Chemie, Arbeitsgruppe Makromolekulare Strukturanalyse, c/o DESY, Notkestraße 85, 22603 Hamburg, Germany

INTRODUCTION

The discovery of new functions of ribonucleic acids gave rise to an increasing interest in RNA technology in recent years. Catalytic features of ribozymes or the high-specific binding capability of aptamers opened new fields in medical diagnostics & therapy, molecular biology and environmental sensorics. For the functional design of such RNA molecules knowledge about their structure is necessary. Till now a few RNA structures are solved in detail [1].

We have chosen structural domains of ribosomal 5S RNA as model substances.

With a length of 120 nucleotides the 5S rRNA represents the smallest ribosomal RNA. The omnipresence of 5S rRNA and its high degree of conservation, implies that it plays an essential role in the ribosome [2]. However, due to the far distance from the peptidyl transferase center the 5S rRNA is not directly involved in interactions with ribosomal ligands. Instead, the protein-mediated interactions between the ribosomal 5S RNA and the 23S RNA of which domain V represents the catalytic center of the ribozyme are particularly extensive. Is 5S rRNA assisting the assembly of ribosome only? Yet, its significance during protein biosynthesis remains unclear [3].

In recent years our lab has screened several 5S rRNAs on their crystallization behavior. Best crystals of *Thermus flavus* one provided resolution data up to 7.5 Å at Elettra. Both the low resolution and a solvent content of 54 % are grounds for

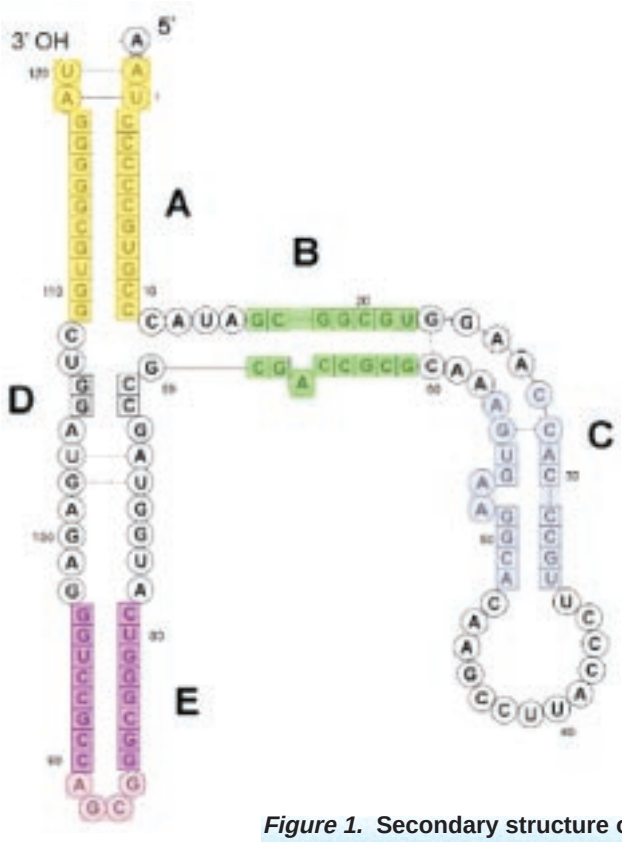

Figure 1. **Secondary structure of wildtype *Thermus flavus* 5S rRNA.** The domains which have been crystallized and subsequently measured at Elettra are marked. Structure solutions are available for the domains A, B and E [4], it is just in progress for C.
By choosing these helical regions we were able to improve structural refinement of key water molecules, G:U wobble base pairs and ionic interactions.

assuming that the molecules are partly disordered in the crystal lattice causing an intrinsic flexibility. Nowadays 5S rRNA variants are being engineered in such a way that they maintain their biological activity while increasing the stability along with their suitability for crystallization [4]. For these purposes modified molecules have been created by introducing crystal promoting motifs, by replacing flexible parts or by reducing the molecule to more stable fragments (Fig. 1).

Here we present the crystallization data and structure solution of E-helix (E3) consisting of the nucleotides 79-86 & 90-97 (Fig. 1). In addition to the native sequence the base CYT84 has been modified with bromine in 5'-position.

MATERIAL & METHODS

Progresses in the chemical synthesis allow the production of RNA oligonucleotides in large quantities and at high purity as well as the

After computer-aided hybridization (*ALKABRID V. 3.0*) the crystallization was performed in the hanging drop applying self-developed screening protocols based on 2-methyl-2,4-pentanediol (MPD) precipitation [5].

Data collection occurred under cryogenic cooling conditions at the X-ray diffraction beamline 5.2 R at the Trieste synchrotron station Elettra. Data processing and determination of space group and unit cell were carried out with the programs *DENZO* and *SCALEPACK* [6].

RESULTS & DISCUSSION

Most crystals appeared in a couple of days at 18°C (Fig. 3). The conditions for crystallization as well as the X-ray diffraction data are given in Table 1.

Especially, the change of space group and axes system represents an interesting fact of which structural significance is still to be revealed.

The structure solution was obtained by

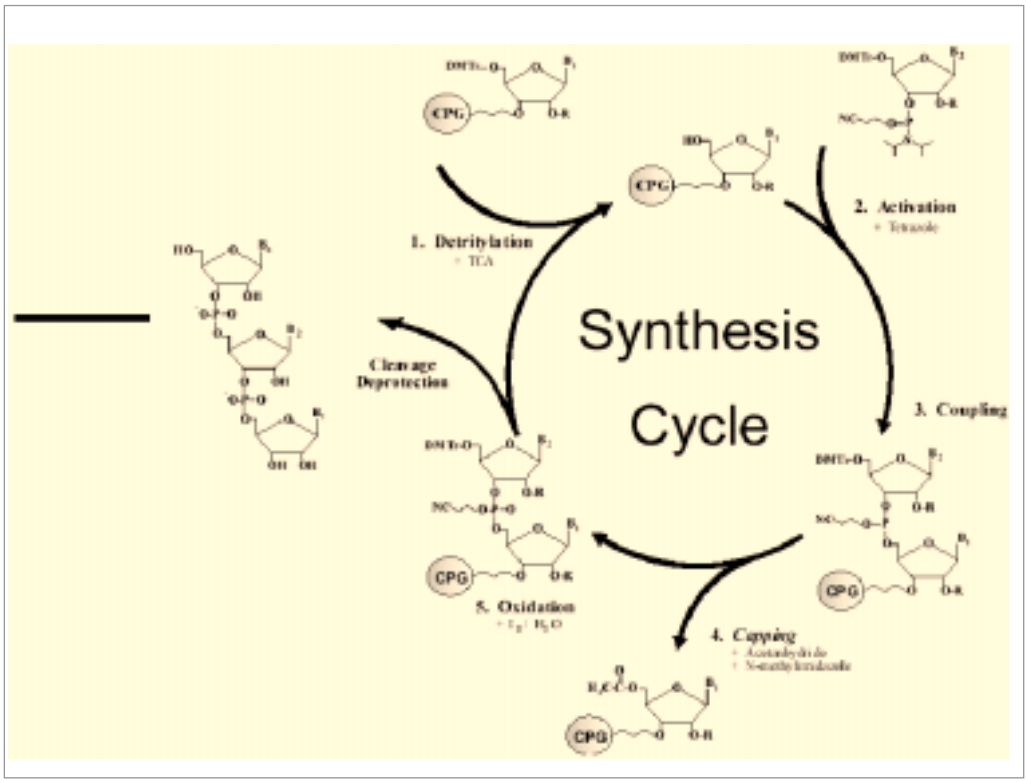

Figure 2. **Path of synthesis of RNA oligonucleotides for crystallization purposes.** The cycle starts with the acid cleavage of dimethoxytrityl at the first immobilized nucleoside (1). In the 2nd step tetrazole activates the phosphorus of the amidite enabling the coupling by cleavage of diisopropylamine (3). 5'-hydroxyl groups of polymer chain which have not reacted are acetylated (4) whereas the phoshittriester formed is oxidized by iodine (5). Afterwards next round begins. The final removal of protecting groups as well as the cleavage of the product happen in an alkaline milieu. RNA strands are further purified by rpHPLC.

molecular replacement using the program *AMoRe*. The native sequence r(CUGGGCGG)-r(CCGCCUGG) has already been solved up to 1.6 Å.

Water molecules in the major groove of the helix are stabilizing the entire RNA molecule by a network of hydrogen bonds. The tandem formation of G:U wobble base pairs, a frequent mismatch in RNA, is stabilized by three structural waters whose hydrogen bonds are offsetting the missing 3rd hydrogen bond of a G:C base pair [4, 5].

As a curiosity an unusual G:C base pair in non-Watson-Crick arrangement has been revealed (Fig. 4).

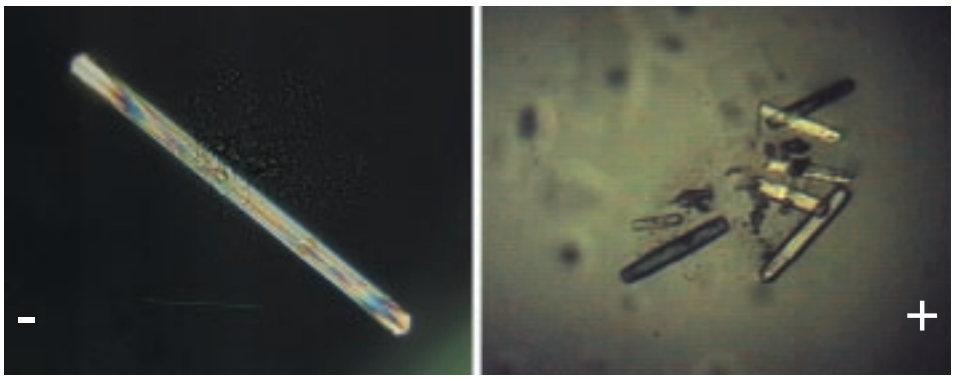

Fig. 3 Crystal pictures of the RNA minihelix E3 without (-) and with bromine (+)

Table 1 Crystallization and X-ray diffraction data of a RNA minihelix and its bromine derivate

RNA sample	8 bp helix E3	8 bp helix E3 ($^{5'\text{-Br}}$C84)		8 bp helix E3	8 bp helix E3 ($^{5'\text{-Br}}$C84)
Crystallization conditions			**X-ray diffraction data set**		
Sequence	5'CUGGGCGG 3' |||||||| 3'GGUCCGCC 5'	5'CUGGG^{Br}CGG 3' ||||| ||| 3'GGUCC GCC 5'	Cell axes	a = 41.94 Å b = 41.94 Å c = 127.09 Å	a = 39.805 Å b = 39.805 Å c = 35.578 Å
Concentration	0.25 mM	0.25 mM	Cell angles	alpha = 90.0° beta = 90.0° gamma = 120.0°	alpha = 90.0° beta = 90.0° gamma = 120.0°
Crystallization solution	NUC 12	NUC 20			
pH	6.0	7.0			
Buffer	40 mM sodium-cacodylate	40 mM sodium cacodylate	Space group	R32	P3
Precipitant	10 % (v/v) MPD	10 % (v/v) MPD	$V_{unit\ cell}$	223546.7 Å³	48818.9 Å
Polyamine	12 mM $SpCl_4$	12 mM $SpCl_4$	V_M value	2.35 Å³ / Da	2.68 Å /Da
Monovalent ion	80 mM KCl	80 mM NaCl	$Duplexes_{RNA}$ / asymmetric unit	1	1
Divalent ion	20 mM $BaCl_2$	20 mM $BaCl_2$			
Reservoir solution			Radiation source	Elettra / 5.2R	Elettra / 5.2R
pH	7.0	7.0	Wavelength	1.000 Å	1.000 Å
Buffer	none	none	Detector	IP 180 mm	MAR 345 mm
Precipitant	30 % (v/v) MPD	30 % (v/v) MPD	Temperature	100 K	100 K
Polyamine	none	none	Max. resolution	1.5 Å	1.6 Å
Monovalent ion	none	none	$Resolution_{data\ set}$	30.0 - 1.6 Å	30.0 - 1.6 Å
Divalent ion	none	none	Measurements	43171	2735
Crystal features			Unique reflections	5994	624
TempCrystallization	18°C	18°C	R_{symm}	6.6 %	4.9 %
Time of growth [d]	1	30	$R_{symm\ last\ resolution\ shell}$	29.2 %	14.2 %
Crystal size [mm] & shape	0.05 x 0.05 x 0.8 long rods	0.06 x 0.06 x 0.14 short rods	Completeness	96.1 %	97.8 %
			$Complet._{last\ resol.\ shell}$	89.1 %	98.0 %

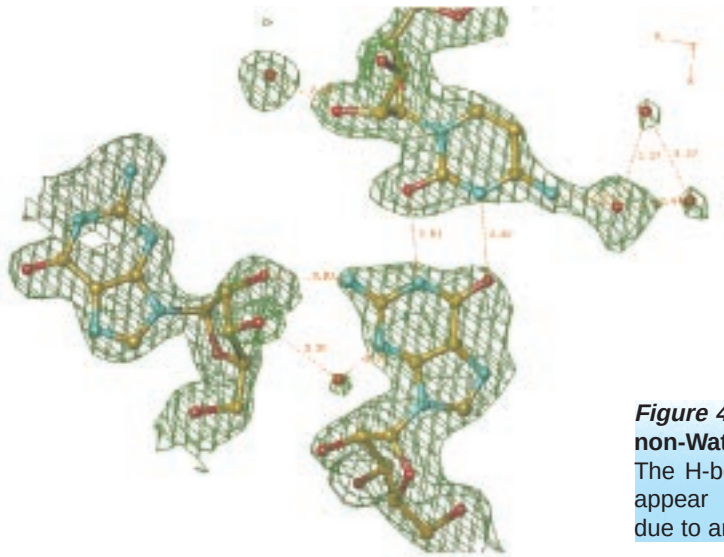

Figure 4. **Electron density map of a G:C base pair in non-Watson-Crick arrangement.**
The H-bond between N3 (CYT84) and N1(GUA92) could appear either in the case of imino form of cytosine or due to an additional protonation of the N3 atom.

The structure of the bromine-modified RNA helix has been refined up to 2.6 Å at the moment (Fig. 5). The present R-factor is 20 % and the R_{free} is 26 %. At this point special features are not to be displayed. A further refinement is just in progress. Particularly, due to a different (neutral) pH value in the crystallization buffer we expect a more detailed explanation of the mentioned non-Watson-Crick-formation.

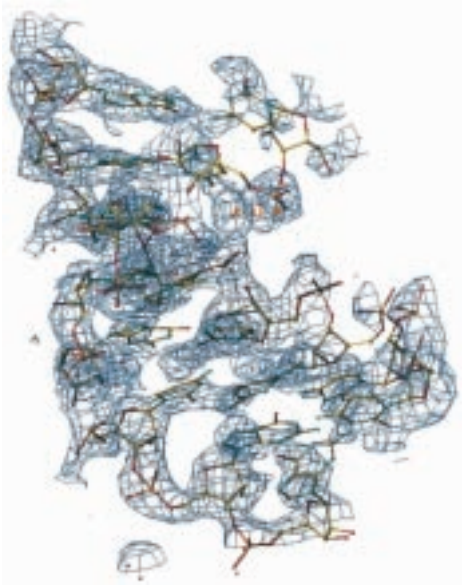

Figure 5. **Initial electron density map of a RNA helix which a bromine ion is coupled at the C5-position to.**
The bromine ion is already localized (left upper corner).

ACKNOWLEDGEMENTS

Thanks to Dr. Rolf Bald and his co-workers for RNA synthesis. Thanks to the staff at Sincrotrone Elettra, and special thanks to Dr. Luca Olivi for advice during measurement. Thanks to the Deutsche Forschungsgemeinschaft (DFG) for financial support.

References:

[1]V.A. Erdmann, S. Lorenz, C. Lippmann, S. Klussmann, A. Nolte, J.P. Fuerste, R. Bald, C. Betzel; *Proceedings of China-Germany Workshop on Microgravity Science*; (National Microgravity Laboratory, Bejing, 1996), p. 52
[2] P. Khaitovich and A.S. Mankin; *J. Mol. Biol.*; 291, 1025, (1999)
[3] N. Ban, P. Nissen, J. Hansen, P.B. Moore and T.A. Steitz; *Science*; 289, 905, (2000)
[4] M. Perbandt, S. Lorenz, M. Vallazza, V.A. Erdmann and C. Betzel; RNA Biochemistry and Biotechnology (J. Barciszewski and B.F.C. Clark (*eds.*), Kluwer Academic Publishers, Netherlands, 1999), p. 63
[5] M. Vallazza, A. Senge, C. Lippmann, M. Perbandt, C. Betzel, R. Bald and V.A. Erdmann; *J. Cryst. Growth*; in press, (2000)
[6] Z. Otwinski; *DENZO, XDISPLAYF, SCALEPACK. An Oscillation Data Processing Program for Macromolecular Crystallography* (Yale University, New Haven, CT, 1993)

Marco Vallazza, Sankaran Banumathi, Markus Perbandt, Corinna Lippmann, Christian Betzel, Volker A. Erdmann

Data Collection at λ = 2.6 Å at the ELETTRA X-ray diffraction beamline

T. Sicker, M.S. Weiss, R. Hilgenfeld
Institute of Molecular Biotechnology, Jena, Germany

Ever since the beginning of the 90s when soft X-rays were first employed in macromolecular crystallography, the interest in the use of soft X-rays to address various problems in biological crystallography has been continuously growing owing to a number of possible applications (for a recent review see [1]):

1. The M(V)-edge of some heavy elements such as uranium provides a very large anomalous signal for phase determination. The Δf'' can be up to 110 electrons at λ = 3.497 Å [2].
2. The increased sulfur signal may be a potential tool in single wavelength anomalous diffraction (SAS) experiments especially for small proteins with a high sulfur content. This could make heavy atom derivatization unnecessary [3].
3. Selectively enhancing the anomalous signal of some elements can help to distinguish them from others [4].

	Δf" in electrons at 1 Å	Δf" in electrons at 3 Å
oxygen	0.01	0.13
sulfur	0.24	1.82
calcium	0.59	3.89
uranium	6.90	33.0

Table 1: Anomalous scattering factor Δf' of selected elements in electrons at different wavelengths.

λ	Air absorption length in mm
1 Å	3177
2 Å	393
3 Å	116

Table 2: Air absorption length at different wavelengths.

The routine use of soft X-rays has so far been hampered by a number of problems, of which the most important one is absorption. For illustration, a few numbers of air absorption length, which is defined by the length of air in mm, over which the X-ray intensity is attenuated by a factor of e (2.718) are given in table 2.

We have attempted to collect a data set as close as possible to the calcium K-edge (3.070 Å) at the ELETTRA XRD-beamline in order to identify weak calcium binding sites in blood coagulation factor XIII and distinguish them from water molecules. Therefore a crystal of factor XIII (space group $P2_1$, a = 133.3 Å, b = 70.8 Å, c = 100.7 Å, ß = 105.8°) was soaked for 17 hours in a buffered solution containing 100 mM calcium chloride. Two calcium binding sites in factor XIII had previosly been identified [5,6], but these could not be linked to the observed biochemical effect - the transformation of the zymogen into the active enzyme with or even without thrombin.

Without any apparative changes to the beamline set-up, we managed to collect a complete data set to 2.9 Å resolution at a wavelength of 2.583 Å. At this wavelength the calcium shows an anomalous signal of about 3 electrons. Furthermore, sulfur atoms also exhibit a measurable signal (Δf'' = 1.4 electrons) at that wavelength. A second data set from the same crystal at λ = 0.861 Å was collected for the later use as a reference in scaling. The data sets have been processed using seven different protocols and the results have been compared in order to determine the best way to handle such data sets. The total data collection time was about 28 hours.

The set of the "best" anomalous differences was obtained using a combination of the programs DENZO [7] or MOSFLM [8] with SCALA [9]. The scaling program SCALEPACK [7] seems to be not the best choice for scaling data collected at long wavelengths, which can be explained by its rather simple scaling model.

Even though there are significant differences in the ΔF-values obtained, all anomalous difference Fourier maps clearly show the known calcium positions in the structure, as well as most of the sulfur positions. As an example the anomalous difference Fourier map based on ΔF-values obtained from MOSFLM/SCALA processing is shown in figure 1 together with a schematic representation of the structure of factor.

As a conclusion, our results suggest that data collection at λ = 2.6 Å is feasible with no changes to the set-up and could be performed on a routine basis at the X-ray diffraction beamline at ELETTRA.

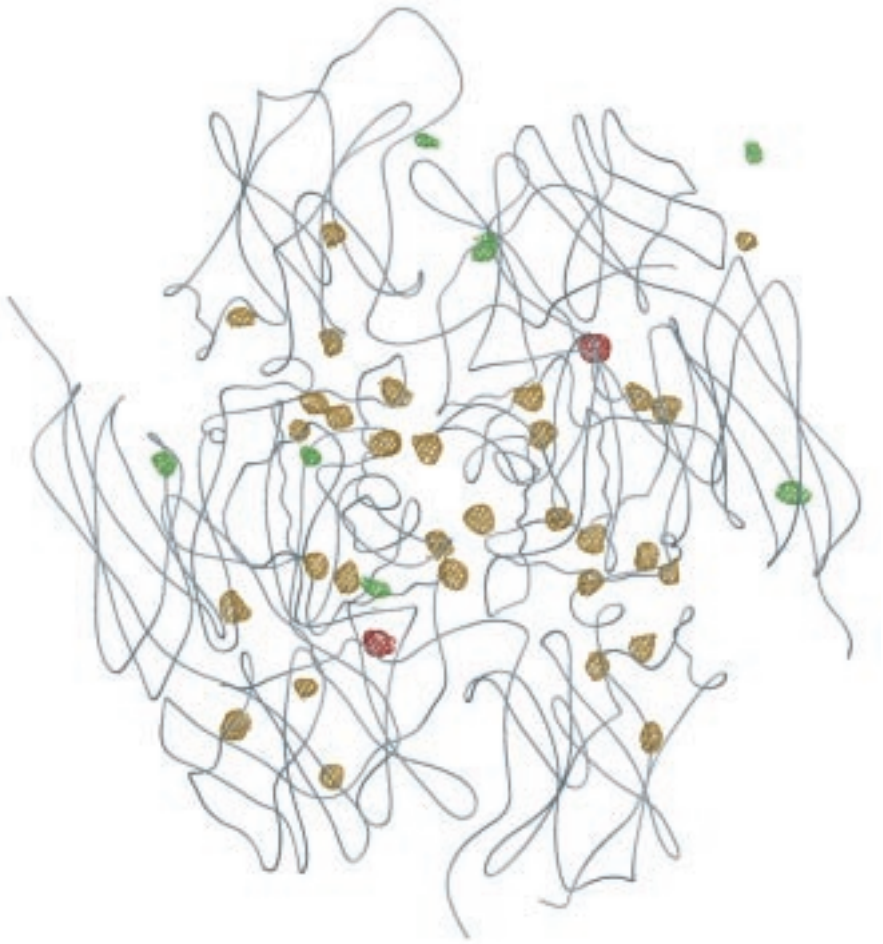

Figure 1: Structure of factor XIII with the 50 highest anomalous difference peaks calculated with the MOSFLM/SCALA protocol colored in red (known calcium ions), yellow (sulfur atoms), and green (unassigned) respectively and contoured at 2σ.

References:

[1] P. Carpentier et al, Cell Mol Biol **46**(5), 915-35 (2000).
[2] W.A. Hendrickson and C.M. Ogata, Meth. Enzymol. **276**, 494-523 (1997).
[3] W.A. Hendrickson and M.M. Teeter, Nature **290**, 107-113 (1981).
[4] H. Einspahr et al (1985), Acta Cryst **B41**, 336-341 (1985).
[5] T. Sicker, Diploma thesis, Jena (1999).
[6] B.A. Fox et al, J. Biol. Chem. **274**, 4917-4923 (1999).
[7] Z. Otwinowski and W. Minor, Meth. Enzymol. **276**, 307-326 (1997).
[8] A.G.W. Leslie, Joint CCP4 + ESF-EAMCB Newsletteron Protein Cyystallography, No. 26 (1992).
[9] Collaborative Computational Project, No. 4, «The CCP4 Suite: Programs for Protein Crystallography". Acta Cryst. **D50**, 760-763 (1994).

T. Sicker, M.S. Weiss, R. Hilgenfeld

The structure of maltodextrin phosphorylase with glucose-1-phosphate

S. Geremia,
Dip. di Scienze Chimiche, University of Trieste, Trieste, Italy

L.N. Johnson, K.A. Watson,
Dep. of Biochemistry, University of Oxford, Oxford UK

R. Schinzel,
Biozentrum, Universität Würzburg, Würzburg, Germany

Structural studies have provided explanations for almost all the key features of control and recognition of phosphorylase, but how does phosphorylase recognise an oligosaccharide substrate at the catalytic site is still an enigma. In order to gain a more complete understanding of carbohydrate recognition, we have studied a simpler enzyme than the mammalian system, the maltodextrin phosphorylase from *E. coli* (MalP). Comparisons between the structures of MalP and active and inactive forms of mammalian phosphorylase have provided explanations for the differences in their regulatory properties consistent with their biological roles. The studies have offered rationalisations towards understanding the evolutionary development, and mechanism of action of these enzymes.[1] Phosphorylase catalyses the phosphorolysis of an α(1-4) glycosidic bond at the non-reducing end of glycogen or oligosaccharides to release glucose-1-phosphate (G1P). We have succeeded in obtaining crystal structures of oligosaccharide bound across the catalytic site both binary and ternary enzyme-substrate complexes (Figure 1 and 2).[2]

In particular, we have determined the structures of the binary complexes of MalP with the natural pentasaccharide (G5) and of MalP complexed with a thiopentasaccharide (GSG4). The latter compound has the α(1-4) oxygen linking the non-reducing end terminal sugar and the adjacent sugar replaced by sulphur and provides an inactive substrate that cannot be phosphorylated. The inactive thio-pentasaccharide GSG4 offers the possibility of a ternary complex with phosphate. Thus we were able to determine the structure of the ternary complex (MalP-GSG4) in the presence of phosphate. These structures show the importance of the conformational change in the oligosaccharide substrate in the formation of ternary complexes and provide support for the previously identified role of the 5'-phosphate of pyridoxal phosphate in catalysis.

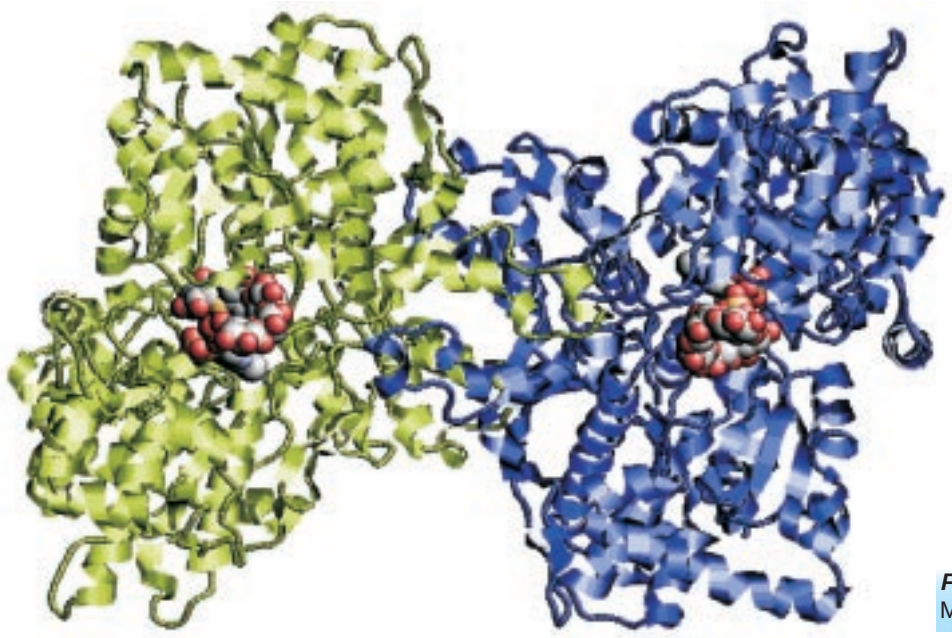

Figure 1. Dimeric structure of MalP-GSG4-P complex.

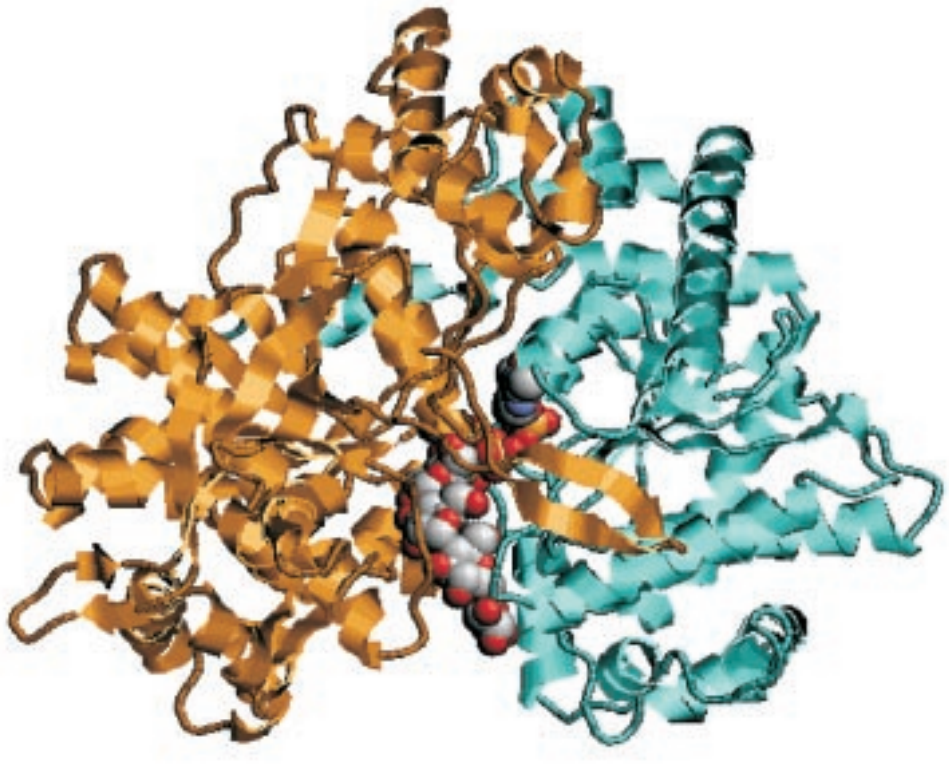

Figure 2. Monomeric structure of MalP-GSG4-P complex. The binding of the oligosaccharide is in a cleft between the two subunits of the monomer.

Further experimental proof of this hypothesis is important. In particular we have recently obtained crystals of the binary complex MalP glucose-1-phosphate (the reaction product) by co-crystallization experiments with the hanging-drop vapor diffusion method. In particular, single crystals of the complex grew from drops consisted of 2.0 µl of a 7 mg/ml protein solution, 0.4 µl of 100 mM G1P solution and 1.6 µl of well solution of composition 27% (w/v) 4K PEG, 0.1 M LiCl, 0.1 M Tris pH 8.5. Optimized crystallization trials typically produced rectangular plate-like morphology in 1-5 days having typical dimensions of about 300 x 50 x 10 μm^3. The resulting crystals were extremely fragile and sensitive to slight changes in temperature and mother liquor and decomposed quickly even upon gentle manipulation. X-ray diffraction experiments on these crystals were carried out at the Elettra Synchrotron Light Source, Trieste, Italy. Data were collected using a monochromatic radiation with wavelength of 1.000 Å and a MAR Research 345 mm imaging plate as detector. Crystals were harvested into mother liquor containing 20% MPD as cryoprotectant with a small loop of fine rayon fiber and flash-frozen in a stream of N_2 at 100 K. Analysis of the diffraction pattern revealed that the crystal belong to the space group $P2_12_12_1$ with unit-cell dimension a = 74.83, b = 105.28 and c = 218.62 Å. This crystal form is similar to that obtained for the MalP-G5, MalP-GSG4 and MalP-acarbose complex crystals grown under similar condition.[2, 3] A complete data set of the MalP-G1P complex was collected to 2.0 Å of resolution. Table 1 reports a summary of data-collection procedures and crystallographic statistics. The structure was determined using the atomic coordinates of the MalP-GSG4 isomorphous structure.[2] The rigid-body refinement of the two polypeptide chains gave an R factor of 0.31.

The G1P substrate was then easily located in an initial difference Fourier electron density map. Restrained positional and thermal factor refinement with non-crystallographic symmetry restrains improved the R and Rfree factors to 0.265 and 0.298 respectively. A subsequent difference Fourier map clearly revealed the presence of a Tris molecule near the G1P substrate in the catalytic site. The final R and Rfree factors are 18.8% and 22.9%, respectively. The refinement and the quality of the final model are summarized in Table 1. The G1P substrate, buried close to the essential cofactor pyridoxal phosphate (PLP), has a large number of hydrogen bonds with the enzyme (Figure 3).

S. Geremia, L.N. Johnson, K.A. Watson, R. Schinzel

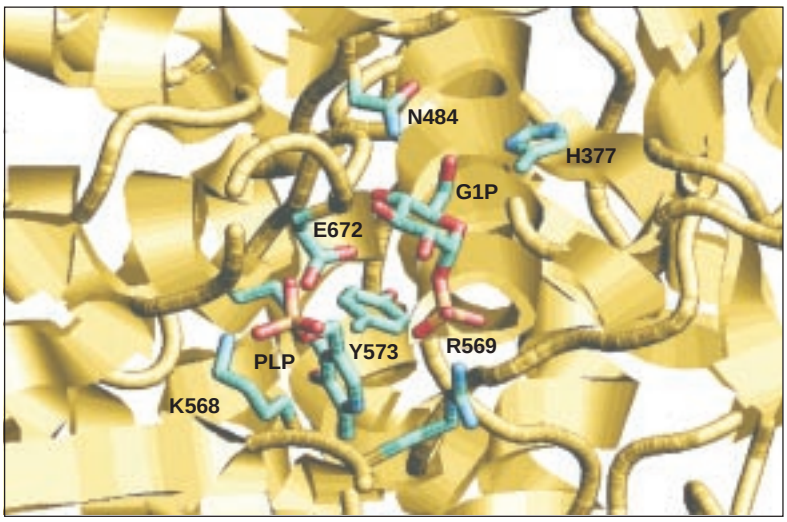

Figure 3. Catalytic site of MalP-GSG4-P complex.

Space group	$P2_12_12_1$
Cell dimensions *(Å)*	74.82, 105.21, 218.76
Resolution limits *(Å)*	50.0 – 2.0
No. of measurements used	423852
No. unique reflections	110577
Completeness (%)	94.7
Multiplicity	3.8
R_{merge} [a]	14.8
I/σ(I)	7.2
Final refinement parameters	
No. of reflection used	104907
No. of independent polypeptide chains	2
No. of protein atoms	12774
No. of cofactor atoms	30
No. of substrate atoms	32
No. of tris molecule atoms	16
No. of water molecules	1252
R factor[a]	0.196
R free[b]	0.242
Weighted r.m.s. deviation from ideal values	
Bond length (Å)	0.009
Angle (deg.)	2.2
B-factor statistics	
Main-chain (Å²)	20.2
Side-chain (Å²)	22.3
Cofactor group (Å²)	15.3
Substrate molecule (Å²)	17.8
Tris molecule (Å²)	18.3
Solvent molecules (Å²)	31.0
All atoms (Å²)	22.1

[a] $R_{fact} = \Sigma \left| Fobs - Fcalc \right| / \Sigma Fobs$

[b] R_{free} was calculated by randomly omitting 5% of the observed reflections from refinement

Table 1

In particular, the MalP-G1P contacts are dominated by contacts to an arginine residue, Arg569, where two phosphate oxygens contact the NE and NH2 atoms of the guanidine side chain. The 5'-phosphate of the PLP cofactor is close to the phosphate of the G1P substrate and is stabilized in this position by a lysine residue, Lys568.

References:

[1] Watson, K.A., Schinzel, R., Palm, D. and Johnson, LN. EMBO J. 1997, 16, 1.
[2] Watson, K.A., McCleverty, C. Geremia, S., Cottaz, S., Driguez, H. and Johnson, L.N. EMBO J. (1999), 18: 4619.
[3] O'Reilly, M., Watson, K.A., and Johnson, L.N. Biochemistry. (1999), 38: 5337.

S. Geremia, L.N. Johnson, K.A. Watson, R. Schinzel

The complement system is the major effector of the B cell-mediated branch of the immune system. Nearly 30 proteins found in the serum are members of the complex complement cascade. Upon activation, they interact in a highly regulated pathway to generate reaction products that ultimately lead to the clearance of virus, bacteria, or mutated cells. When CVF is added to human or mammalian serum, it activates the complement system and leads to its consumption. CVF binds in fact to the protein "Factor B" of the complement pathway, and thus behaves like another natural complement protein, called C3b. The functional similarity between CVF and the complement protein C3b in forming an active complex with Factor B, implies a structural similarity between these polypeptides. Hence, CVF can be used in medical research as a mimic of the human complement protein in highly relevant applications, such as the specific killing of tumor cells in vivo.

Structural Studies of the Cobra Venom Factor: Preliminary Crystallographic Analysis

Sujata Sharma, Pravindra Kumar, Talat Jabeen, Tej P. Singh,
Department of Biophysics, All India Institute of Medical Sciences, 110 029 New Delhi, India

Reinhard Bredehorst,
Department of Biochemistry and Molecular Biology, University of Hamburg, Martin-Luther King Pl. 6, 20146 Hamburg, Germany

Carl-Wilhelm Vogel,
Cancer Research Center of Hawaii, University of Hawaii, 1236 Lauhala St., Honolulu, HI 96813, USA

Markus Perbandt, Christian Betzel,
Institute of Medical Biochemistry and Molecular biology, c/o DESY, Build. 22a, Notkestraße 85, 22603 Hamburg, Germany

Cobra venom factor (CVF) is the complement-activating protein in cobra venom, causing complement consumption in human and mammalian serum [1]. CVF is a three-chain 149 kDa glycoprotein. The protein bears the potential of clinical relevance for xenotransplantation and as a conjugate with anti-tumour antibody for targeted complement activation to induce tumour cell killing. Furthermore, CVF can serve as a tool to investigate the multifunctionality of a protein called C3 which interacts specifically with more than 10 different plasma proteins and cell surface receptors. CVF is a three chain 149,000 Da glycoprotein [2,3]. It consists of three disulphide–linked chains with molecular masses of ~68,500 Da (α – chain), ~48,500 Da (β – chain), and ~32,000 Da (γ – chain). The γ–chain shows a size heterogeneity which appears to be due to differential processing at the C–terminus. CVF contains a carbohydrate component of approx. 7.4% (w/w). The oligosaccharide portion of CVF consists of three N–linked oligosaccharide chains of the complex type, of which two are in the α–chain and one is in the β–chain. The major oligosaccharide could be identified as a symmetric fucosylated biantennary complex type chain with an unusual α–galactosyl residue at its non–reducing end [4]. The molecule has also been used in numerous studies to deplete the plasma complement activity in order to investigate the role of complement in host defence or pathogenesis of disease. Further, CVF bears the potential for clinical relevance as it can be safely administered to laboratory animals [6]

In order to understand various roles of CVF and to exploit its potential clinical applications, it is important to elucidate the three-dimensional structures of CVF, its individual chains and its various complexes with components of the complement. Preliminary X-ray crystallographic experiments for CVF were performed on a rotating anode generator and at ELETTRA.

CVF was isolated from Indian cobra venom (*Naja naja naja*). The multi-chain gylcoyslated CVF appears to be a flexible and a extraordinarily complex molecule with potential difficulties for crystallization. However, native crystals were

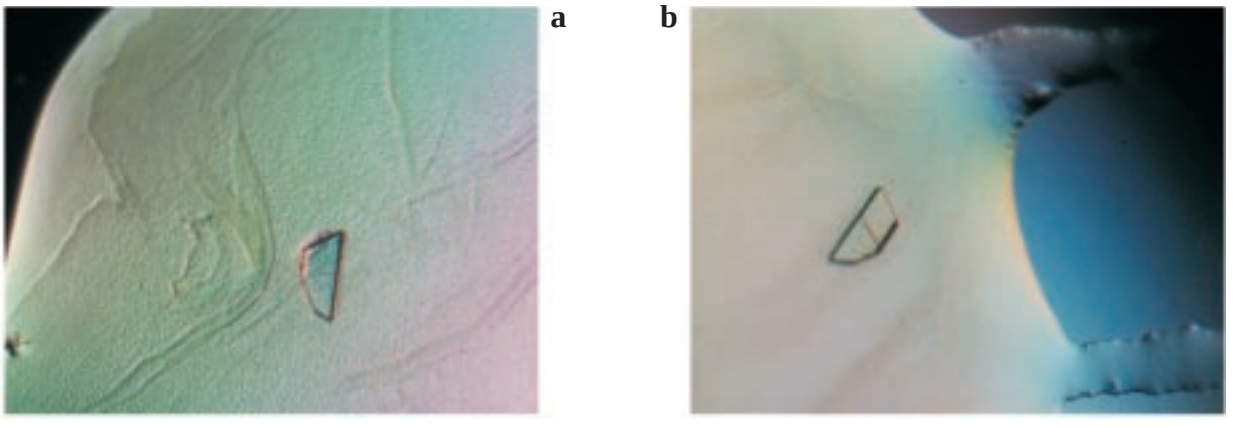

Figure 1: Crystals of irregular shape are shown in a and b. Crystals used for X-ray experiments at ELETTRA.

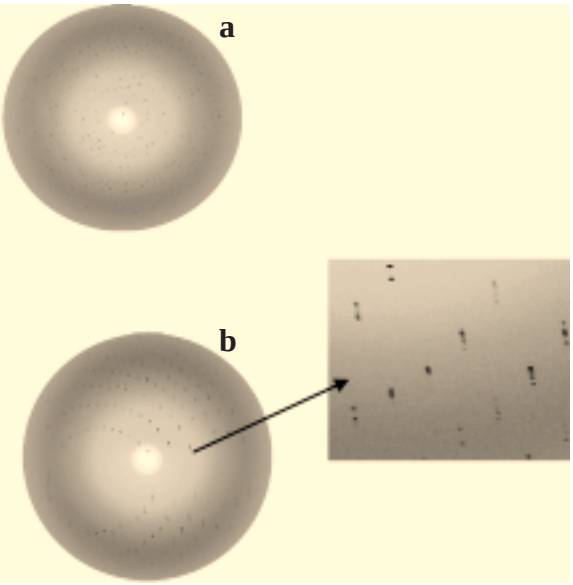

Figure 2: Diffraction pattern of a CVF crystal presented in two crystal orientations:
A) showing the a* and b* section of the reciprocal lattice
B) showing the long cell axis c; a section of the diffraction pattern has been zoomed as well.

obtained using the sitting drop vapour diffusion method. In the first step crystals of slightly irregular shape could be obtained at 20°C at two conditions. X-ray suitable crystals appeared after 6–8 days. The dimensions of the crystals, grown as relatively thin plates, are approximately 0.2 x 0.15 x 0.03 mm^3 as shown in Fig. 1. The space group of CVF crystals was characterised to be P4 when either precipitant solution was applied. The unit cell parameters are: a = b = 62.7Å and c = 368.1Å. The Matthew's coefficient is 2.4 $Å^3$/Da assuming 4 molecules in the unit cell. Applying synchrotron radiation at ELETTRA diffraction extended to approximately 2.7Å. Considering that the crystals were very small and one unit cell dimension is extremely large, the overall quality of the diffraction pattern is good with sharp reflections. A total of 13644 unique reflections were obtained which corresponds to a completeness of 89% with an R_{sym}. of 7.8% and an overall I/σ of 7.6. Hence, the high brilliance beam of ELETTRA allowed the collection of high quality diffraction data. These data will allow a high resolution definition of the CVF structure, whose determination is currently underway.

References:

[1] Vogel, C. –W., Bredehorst, R., Fritzinger, D. C., Grunwald, T., Ziegelmüller, P., and Kock, M. A. (1992) in Singh, B. R. and Tu, A. T. (Eds.) Natural Toxins: Structure and function of cobra venom factor, the complement–activating protein in cobra venom pp. 97–113, Plenum Press, New York.
[2] Eggertsen, G. A., Lind, P., and Sjöquist, J. (1981) Molecular characterization of the complement activating protein in the venom of Indian cobra (*Naja naja naja)*, *Mol. Immunol* **18,** 125–133.
[3] Vogel, C. W., and Müller-Eberhard, H. J.(1984) Cobra venom factor. Improved method for purification and biochemical characterization, *J. Immunol. Methods*,**73,** 203–220.
[4] Gowda, D. C, Schultz, M., Bredehorst, R., and Vogel, C. W. (1992) Structure of the major oligisaccharide of cobra venom factor, *Mol Immunol.* **29,** 335–342.
[5] Henseley, P., O'Keefe, M. C, Spangler, C. J., Osborne, J. C. Jr. and Vogel, C. W. (1986) The effects of metal ions and temperature on the interaction of cobra venom factor and human complement factor B, *J. Biol. Chem.* **261,** 11038–11044.
[6] Cochrane, C. G., Müller-Eberhard, H. J., and Aikin, B. S. (1970) Depletion of plasma complement in vivo by a protein of cobra venom: its effects on various immunologic reactions, *J. Immunol.* **105,** 55–69.

Low Resolution Crystallography on Human Plasma Low Density Lipoprotein (LDL)

R. Schwarzenbacher, H. Amenitsch, P. Laggner, R. Prassl,
Institute of Biophysics and X-ray Structure Research, Austrian Academy of Science, Steyrergasse 17, 8010 Graz, Austria

F. Nigon, M.J. Chapman,
INSERM Unité 321, F-75651 Paris, France

S. Bernstorff,
Sincrotrone Trieste, Italy

Human plasma low density lipoproteins (LDL, Mw = 2.6×10^6 Da) are the main carrier of cholesterol in the blood stream and hence of central biomedical interest for cardiovascular research and premature development of atherosclerotic disease [1-3]. The long term goal of the present project is the analysis of the 3-dimensional structure of apo-B100 (4536 amino acid residues and a molecular mass of about 550 kDa) in intact LDL, i.e. associated with various lipids, mainly phospholipids and cholesteryl esters. The knowledge of the detailed structure of apo-B100 would lead to an understanding of receptor-mediated pathways and structure-function relationship of the LDL-particle.

Crystals with dimensions of approx. 400 x 200 x 100 microns are obtained from highly homogenous LDL subspecies [4]. X-ray diffraction data show a strongly anisotropic behavior and are limited to a resolution of a = 15Å, b =c = 28Å. Patterns like the one shown in Fig. 1 indicate a colloidal type of crystal form, with one dimensional long range ordering along the a-axis, showing reflections up to the 12th order (15Å), with a prominent 5th order at 35Å,

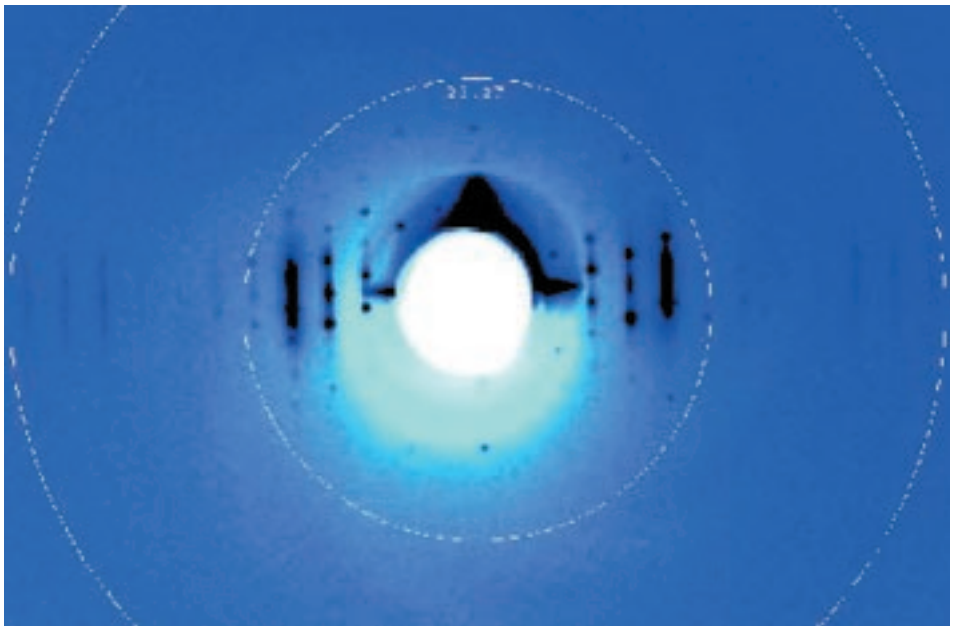

Figure 1: Diffraction pattern of a LDL crystal showing the dimensional long range ordering along the a-axis, and reflections up to the 12th order (15Å), with a prominent 5th order at 35 Å, corresponding to the length of a cholesterylester molecules.

corresponding to the length of a cholesterylester molecule.

The aim of the present experiment is to obtain the global arrangement of protein, lipid and cholesterol within the particle, which requires accurate measurements of all the low resolution reflections in the range of 400-20Å. To achieve this we used a 0.2 x 0.2mm beam profile and a sample to detector distance of 750mm, equipped with an evacuated beam path and a beam stop mounted in vacuum close to the CCD-camera. The CCD-camera is equipped with a fast read out electronic (typical readout times of 150 ms) and has 1024x1024 pixels with an optical active area of ~ 80 x 80mm. The crystal was measured under cryogenic conditions (100K) using a delta-phi of 10 degrees and exposure-times of 10 sec/frame (corresponding to rotation speed of 1deg/s). 40 frames of each angular slice were summed for the final images (Fig. 2).

A structural model based on a combination of X-ray diffraction data, solution scattering data and cryo-electronmicroscopic images [5], which indicate an elliptical particle shape and a well-defined internal layer-structure with a periodicity of about 1/35 $Å^{-1}$ is currently under construction. The application of these newly established methods for LDL should allow for the identification of certain domains within this supramolecular assembly of lipid and protein which are prone to oxidative attack and subsequently to pathological modifications.

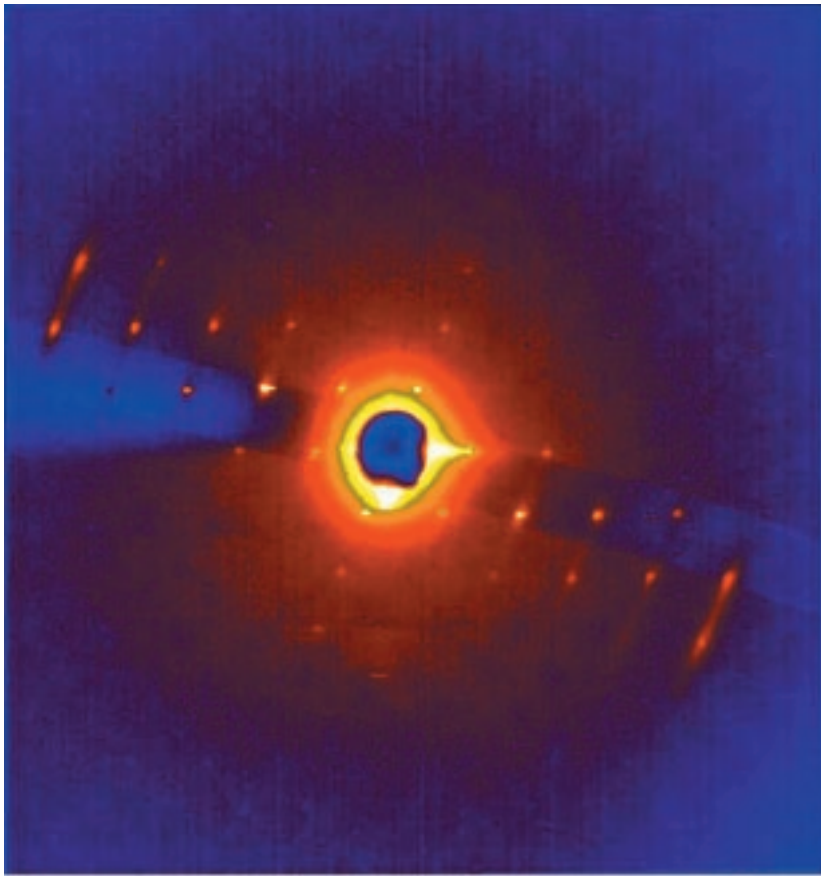

Figure 2: Example for a LDL single crystal diffraction image of a 180 deg phi-rotation with an angular slicing of 10 deg/frame. Each frame has been sampled 40 times. Rotation speed was 1 deg/s.

References:

[1] M.S. Brown and J.L. Goldstein; *Science* **232**, 34-47 (1986)
[2] M.J. Chapman, P.M. Laplaud, G. Luc, P. Forgez, E. Bruckert, S. Goulinet, and D. Lagrange; *J.Lipid Res.* **29**, 442-458 (1988)
[3] B. Schuster, R. Prassl, F. Nigon, M.J. Chapman and P. Laggner; *Proc.Natl.Acad.Sci.USA* **92**, 2509-2513 (1995)
[4] R. Prassl, J.M. Chapman, F. Nigon, M. Sara, S. Eschenburg, C. Betzel, A. Saxena and P. Laggner; *Biol.Chem.* **271**, 28731-28733 (1996)
[5] E.V. Orlova, M.B. Sherman, W. Chiu, H. Mowri, L.C. Smith and A.M. Gotto *PROC.NAT.ACAD.SCI.USA* **96**, 8420-8425 (1999)

R. Schwarzenbacher, H. Amenitsch, F. Nigon,
M.J. Chapman, S. Bernstorff, P.Laggner, R. Prassl

Diffraction Enhanced Imaging (DEI) at the SYRMEP beamline

F. Arfelli, E. Castelli, R. Longo, A. Olivo, S. Pani, P. Poropat, L. Rigon,
Dipartimento di Fisica - Università di Trieste and INFN - Sez. di Trieste (I)

A. Bravin,
ESRF – Grenoble (F)

R. H. Menk, G. Tromba,
Sincrotrone Trieste, Italy

Conventional X-ray imaging.

In conventional radiology image contrast results from the differences in the X-ray absorption due to variation of density, composition or thickness of the sample.
It turns out that, for a given dose, the main limitation of this technique is the poor enhancement of weakly absorbing details in soft tissue.

Why to use the "phase sensitive techniques"?

Phase sensitive techniques are based on the observation of the phase-shifts produced by the object on the incoming wave. In general, the phase contribution becomes relevant if the source has a high spatial coherence as occurs in the case of Synchrotron Light sources. In the energy range of 15÷25 keV, the phase shift is up to 1000 times more sensitive to variation of the structure and composition of soft biological tissue when compared to absorption. Therefore it is possible to reveal phase effects even if the absorption is negligible. Recently several approaches for phase effect-based radiology have been reported.

How does the DEI work?

One of these techniques is the Diffraction Enhanced Imaging (DEI) which takes into account the refraction angles of X-rays produced by the sample. A perfect crystal is placed between the sample and the detector (Fig. 1) and acts as an angular selector for X-rays. This crystal diffracts only the fraction of X-rays refracted by the sample in the angular range within the reflectivity curve of the crystal itself (whose width is of the order of 10 microradians). Since the refractive angle is roughly proportional to the gradient of refractive index, the analyzer allows to get information about the refractive index gradient of the sample itself.

Refraction images with DEI.

If the analyzer crystal is perfectly aligned with the monochromator, the X-rays scattered or refracted at angles higher than some tens of microradians are removed from the beam and do not reach the detector. In this case the produced image looks similar to a conventional absorption image with an enhanced contrast and improved detail visibility due to the scatter rejection.
By slightly detuning the analyzer with respect to the monochromator, it is possible to enhance the reflectivity of X-rays refracted in a certain direction. The resulting images reveal an increased contrast for the details whose refractive index gradient results in refraction angles matching with the detuning angle. Therefore, unlike conventional radiography, the image is produced because of the differences in the refraction angles of X-rays. These effects are visible in the image of the mouse (Fig. 2) taken at the SYRMEP beamline with the DEI technique. Working at appropriate angular positions of the analyzer, soft tissues such as liver, lungs and fur become visible even if their absorption to X-rays is negligible.

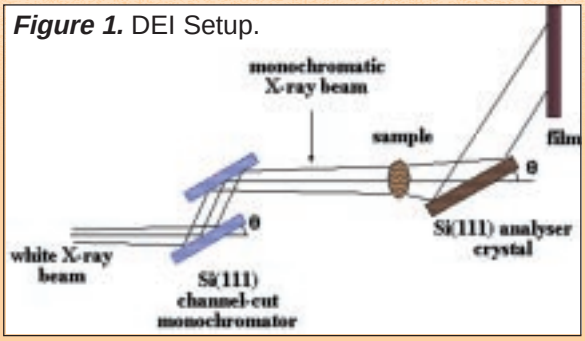

Figure 1. DEI Setup.

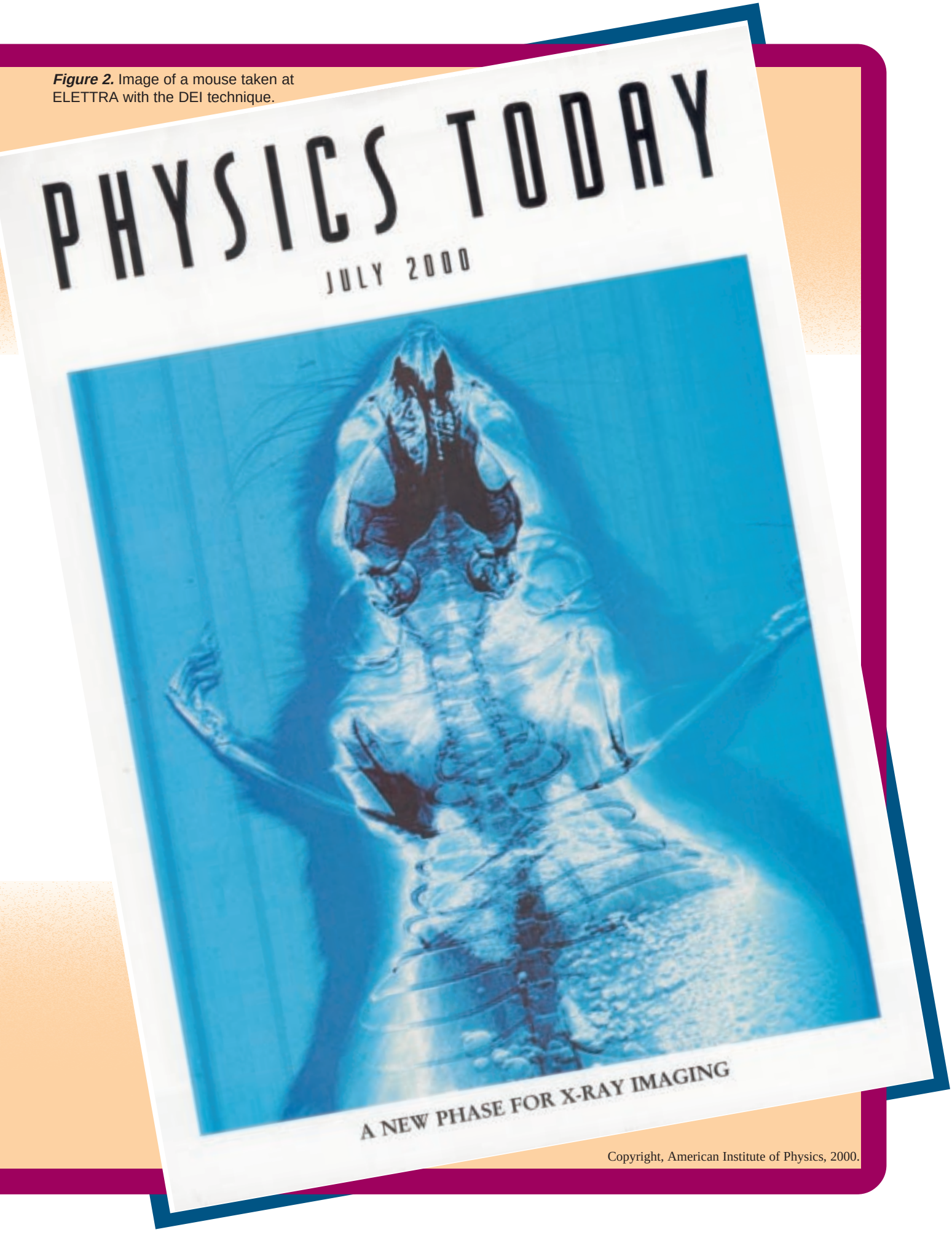

Figure 2. Image of a mouse taken at ELETTRA with the DEI technique.

F. Arfelli, E. Castelli, R. Longo, A. Olivo, S. Pani, P. Poropat, L. Rigon, A. Bravin, R. H. Menk, G. Tromba

More Structural Information from Smectic Phases Full Q-Range Fitting with High Quality X-Ray Data

G. Pabst, M. Rappolt, H. Amenitsch, P. Laggner,
Institute of Biophysics and X-ray Structure Research, Austrian Academy of Sciences, Steyrergasse 17, A-8010 Graz, Austria

S. Bernstorff,
Sincrotrone Trieste, Italy

A novel X-ray analysis method (MCG) has been developed [1] and tested on various phospholipid dispersions. MCG, which is an indirect Fourier method, combines a modified Caillé theory (the "M" and the "C" of MCG) structure factor [2] with a **G**aussian (the "G" of MCG) model representation of the bilayer electron density profile and is thus capable of fitting the full q-range, i.e., both Bragg peaks plus diffuse scattering. Hence, meaningful structural information can be derived from the powder diffraction patterns of fully hydrated phospholipid bilayer stacks, exhibiting usually only 2–3 diffraction peaks in the L_a-phase. The details of the method are described in [1].

As an example we present the structure of POPC (1-palmitoyl-2-oleoyl-*sn*-glycero-3-phosphocholine) 20% w/w in a temperature range of 10°C to 70°C. Figure 1 shows the diffraction pattern of POPC at 50°C, exhibiting only two orders of diffraction. A simple integration of the Bragg peaks results in the rude electron density profile depicted in the insert of Fig. 1 (dashed line). The MCG model (solid line) gives a good fit to the diffraction data in the full q-range and a clearly refined structure of the electron density profile.

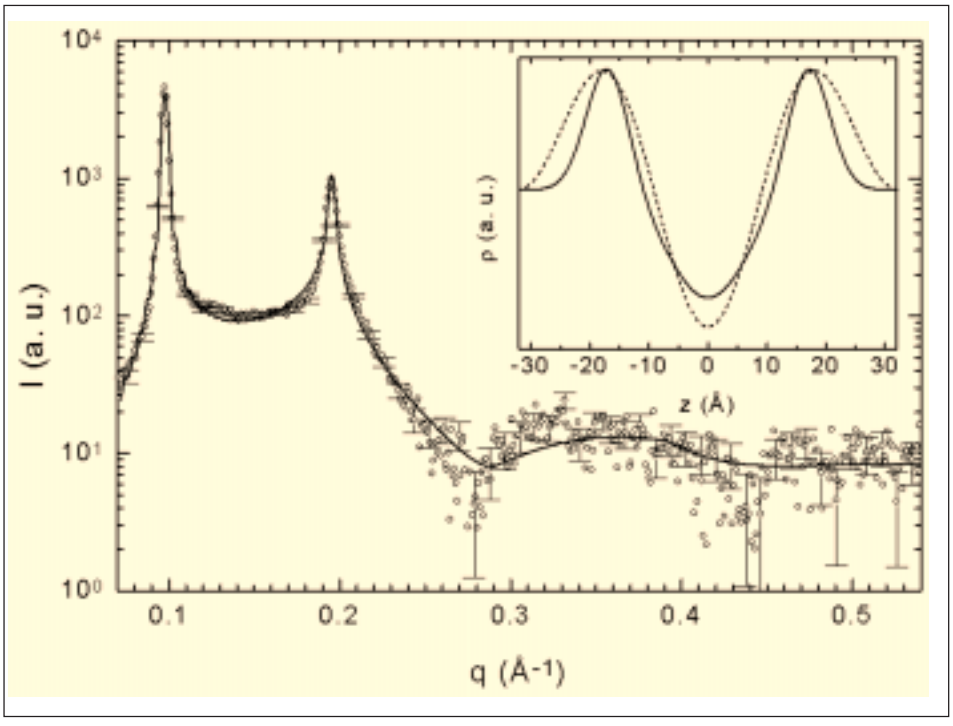

Figure 1. The best fit of the MCG model (solid line) to the diffraction pattern of POPC at 50°C. The insert gives the electron density profile obtained by a Fourier synthesis (dashed line), using Lorentzians to fit the Bragg peaks, and the profile refined with MCG (solid line).

Figure 2 depicts the MCG results for d-spacing, the membrane thickness, d_B, the water layer thickness, d_W, and the area per lipid, A, for POPC in the temperature range of 10°C to 70°C. The lamellar repeat decreases as the temperature is raised up to 30°C down to a value of d = 63.6 ± 0.1 Å. Above 30°C, the bilayer-water system swells again and finally exhibits a larger lattice parameter at 70°C than at 10°C. The decomposition of the d-spacings into bilayer and interbilayer water thickness reveals that this is caused by an uptake of water, as the membrane thickness continuously decreases with increasing temperature, but the bilayer separates more and more, such that the sum of both gives the observed re-increase in d-spacing. The area per lipid is found to increase, as the temperature is augmented. This is the result of increased molecular motions and hydrocarbon chain melting such that the individual lipid molecules require laterally more space.

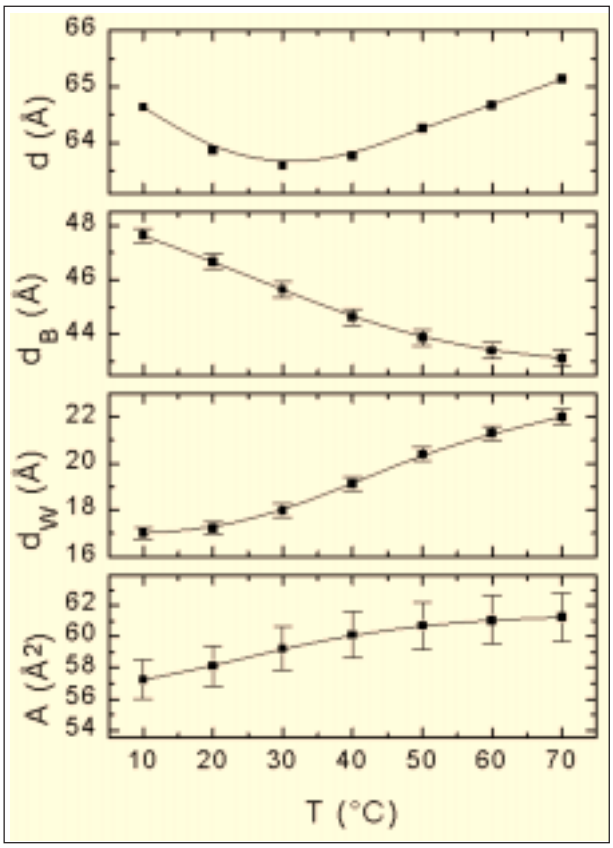

Figure 2. The equilibrium structure of POPC bilayers in the L_a-phase at different temperatures. The changes on d-spacing, membrane thickness and interbilayer water thickness are depicted. The observed re-increase in lamellar repeat distance is due to an uptake of water which increases the bilayer separation, whereas the membrane itself gets thinner with temperature and exhibits an asymptotic behavior above 50°C. Data published in [3].

References:

[1] G. Pabst, M. Rappolt, H. Amenitsch and P.Laggner; *Phys. Rev. E* **62**, in press (2000)
[2] R. Zhang, R.M. Suter and J.F. Nagle; *Phys. Rev. E* **50**, 5047-5060 (1994)
[3] G. Pabst, M. Rappolt, H.Amenitsch, S. Bernstorff and P. Laggner; *Langmuir*, in press (2000)

Materials and Surfaces

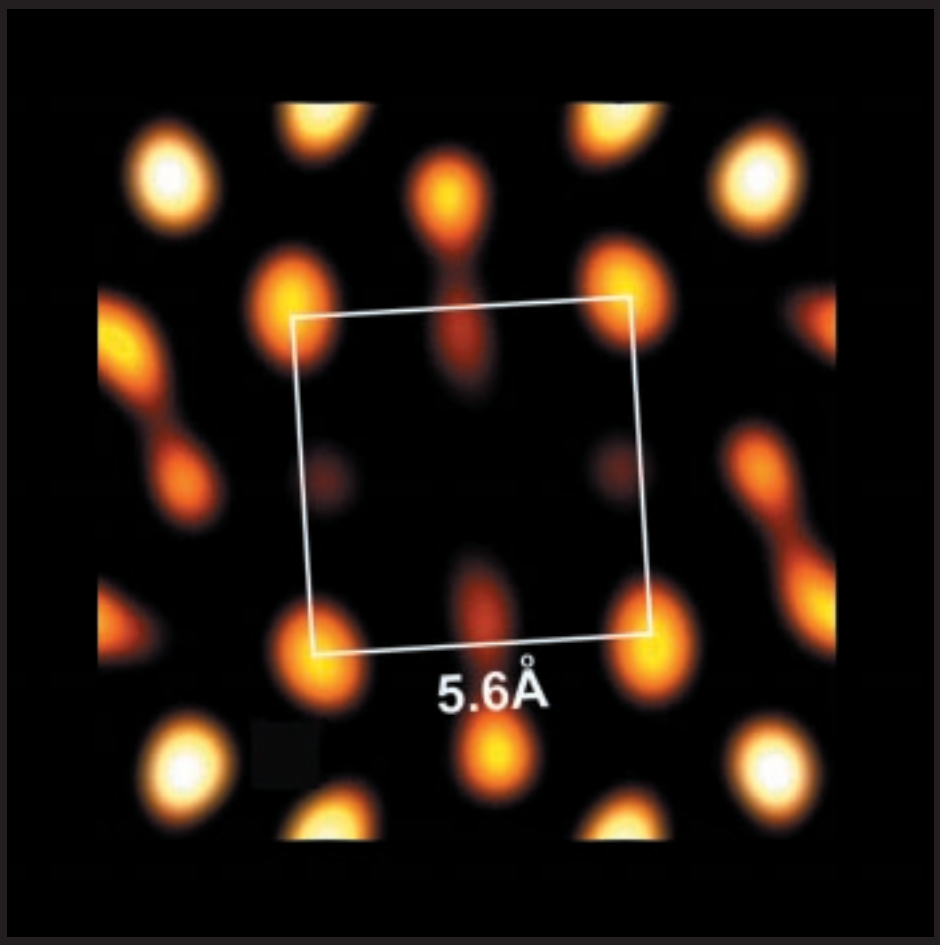

Structural Studies

A New Approach to X-ray Fluorescence Holography Experiments

M. Kopecky, E. Busetto, A. Lausi, R. H. Menk, M. Miculin, A. Savoia,
Sincrotrone Trieste, Italy

INTRODUCTION

Real-space three-dimensional imaging at atomic resolution, the original goal that led Gabor to the discovery of holography, was not achieved until recent years, when A. Szöke pointed out that the interference patterns of characteristic X-rays, photoelectrons or Auger electrons emitted by atoms inside a solid can be thought of as holograms and used for resolving the vicinity of the emitting atoms [1]. And indeed, shortly after Szöke argument was presented, Electron Emission Holography was developed both theoretically and experimentally into a useful practical tool in surface science [2]. In spite of the more ideal nature of X-ray scattering by atoms, *i.e.* (i) negligible multiple scattering, (ii) much more isotropic, (iii) negligible phase shift when compared to electrons, the development of X-ray Fluorescence Holography (XFH) as bulk probe has been much slower, and only in 1996 the first successful *internal source* XFH experiment was reported by Tegze *et al*. [3].

In the same year, T. Gog et al. proposed and realized a XFH experiment based on the alternative concept of *internal detector* [4]. In this case, the source of radiation and the detector are interchanged in accordance with the optical reciprocity theorem. This makes possible to measure holograms for several energies, thus solving the problem of twin images.

The main problem of XFH lies in the practical realization of experiments. The large number of experimental points and the precision requirements make the measurements of holographic patterns very difficult and time demanding also when using powerful synchrotron radiation sources. That is why only a few successful experiments on well-known structures of heavy atoms have been reported so far [3-6].

We carried out an XFH experiment by using a new approach to the detection of fluorescence photons [7] which made it possible to measure higher fluxes and to reduce drastically measuring times.

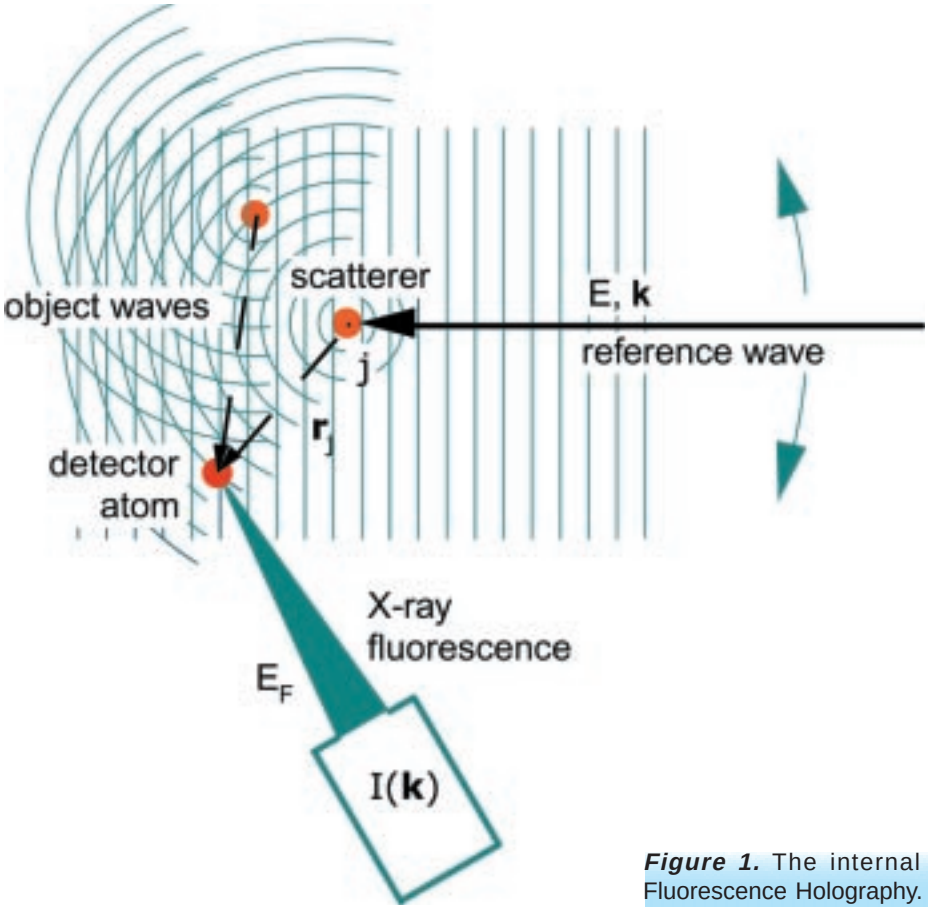

Figure 1. The internal detector scheme of X-ray Fluorescence Holography.

THEORY

The internal detector scheme of XFH [4] has been chosen to record a hologram (Fig. 1). A sample is illuminated with a monochromatic X-ray beam of energy E and wave vector **k**. The electric field in the location of the emitter $\psi(\mathbf{k})$ consists of the unscattered portion of the incident wave $\psi_0(\mathbf{k})$, which serves as holographic phase reference (R-wave), and of the portion elastically scattered at neighboring atoms $\psi_S(\mathbf{k}, °\mathbf{r}_j)$ (object or O-waves). The function $\psi_S(\mathbf{k}, °\mathbf{r}_j)$ depends on the positions $\mathbf{r}_j$ of all atoms j. The amplitude of the contribution from the j-th atom is proportional to $1/|\mathbf{r}_j|$, its phase is determined by the difference in path relative to the reference wave $\mathbf{k}\cdot\mathbf{r}_j$-k.$r_j$. The local wave field strength is proportional to the total amount of fluorescence generated by the emitter. The intensity I(**k**) for different directions of the incident beam is measured by a detector fixed with respect to the sample:

(1)

$$I(\mathbf{k}) \propto |\psi(\mathbf{k})|^2 = |\psi_0(\mathbf{k})|^2 + |\psi_S(\mathbf{k}, \mathbf{r}_j)|^2 + 2\,\mathrm{Re}[\psi_0(\mathbf{k})\,\psi_S^*(\mathbf{k}, \mathbf{r}_j)]$$

The first and second terms correspond to the intensities of the R- and O-waves, respectively. The third one is an interference term between the reference and object waves, *i.°e.* the hologram $\chi(\mathbf{k})$. The extraction of $\chi(\mathbf{k})$ from the experimental data is not easy because $\chi(\mathbf{k}) / I(\mathbf{k}) \approx 10^{-4} \div 5\cdot10^{-3}$. This ratio depends on **k** and the on the environment of the emitter, *i. °e.* on the positions and the atomic weights of surrounding atoms. The real-space reconstruction U(**r**) can be calculated from $\chi(\mathbf{k})$ by using the Helmholz-Kirchhoff theorem:

$$U(\mathbf{r}) = \iint \chi(\mathbf{k})\, e^{-i\mathbf{k}\mathbf{r}}\, d\Omega_{\mathbf{k}}, \qquad (2)$$

where the integral is over the part of a sphere in reciprocal space with radius k=|**k**| for which intensities I(**k**) have been measured. The measurements can be carried out at multiple energies which leads to an improvement of atom images and to the suppression of twins [8].

EXPERIMENT

The most important part of a holography experiment is the detection of fluorescence photons from the reference atoms. At least 10^7-10^8 photons have to be collected for each direction in order to achieve sufficient statistics. In all the previous experiments, the flux of photons with energies within a narrow window around the emitter characteristic Kα line was detected. The elastically scattered primary beam, inelastic scattering as well as characteristic Kβ line emitted by a reference atom

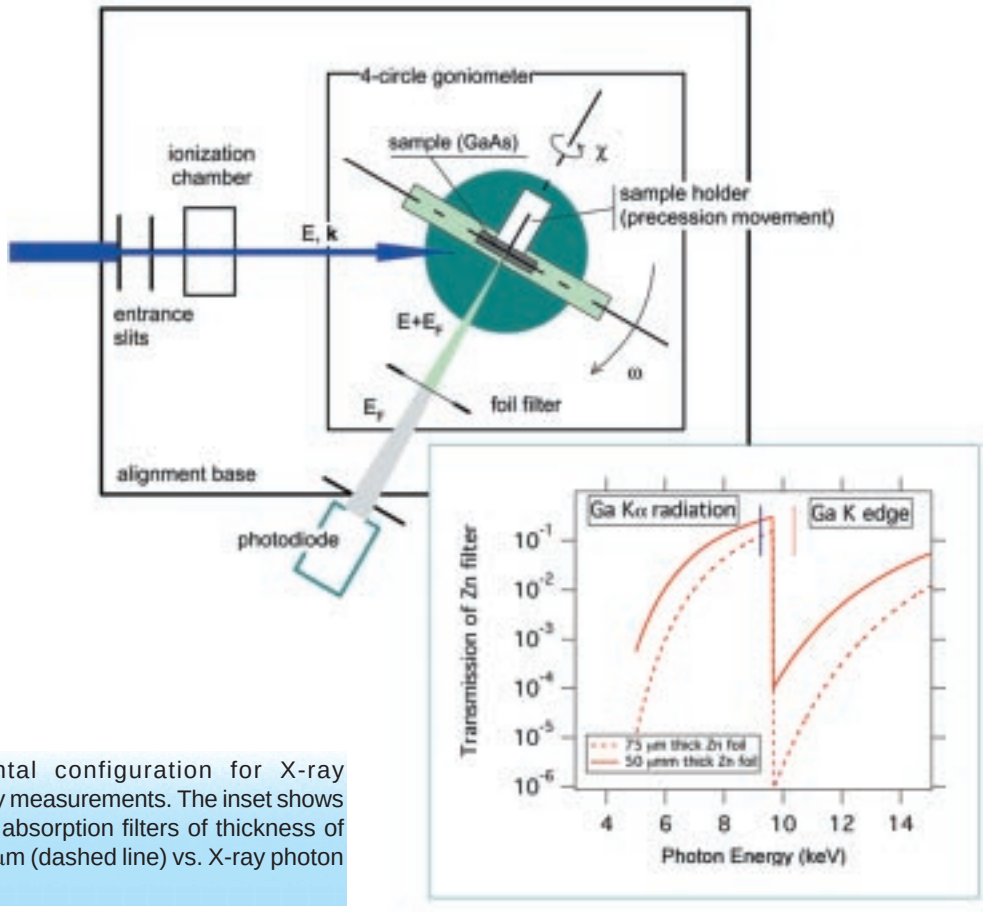

Figure 2. Experimental configuration for X-ray Fluorescence Holography measurements. The inset shows the transmission of zinc absorption filters of thickness of 75 μm (full line) and 100 μm (dashed line) vs. X-ray photon energy.

were suppressed by means of a curved graphite crystal analyzer [4, 6] and/or an energy dispersive detector [3, 5]. In these cases, the photon count rate was strongly reduced by the reflectivity of the graphite crystal, by the linearity limit of energy dispersive detectors, and by the small detection solid angle.

The point is that it is not necessary to select such a narrow energy window. As an example, let us consider a GaAs crystal. Without any limitation, Gallium atoms can be chosen as emitters. In other words, Gallium atoms are used as detectors of the local electric field. As mentioned above, the total fluorescence yield from the detector atoms is proportional to the local electric field strength $\psi(\mathbf{k})$. By using the internal detector XFH scheme, we measure the hologram for an incident beam which has to be monochromatic. But there is no reason to suppress any photon originally emitted by the Gallium atoms. The well-known technique of foil filters to reject effectively the primary beam can be applied also in XFH experiments. Zinc is a suitable material for the

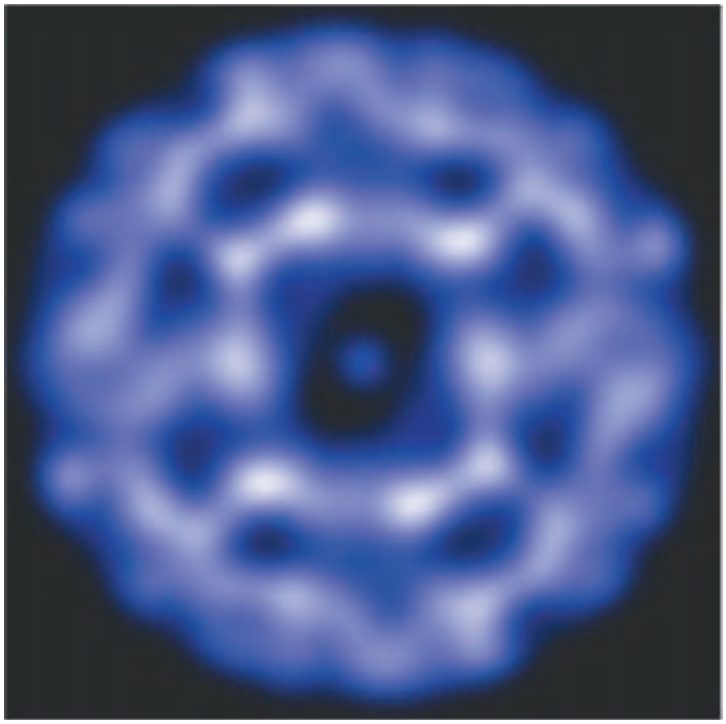

Figure 3 **(a)** Hologram $\chi(\mathbf{k})$ of GaAs measured at E=11.5 keV. This image is a top view of a hemisphere with radius $|\mathbf{k}|$ in the reciprocal space in which the intensity pattern was measured.

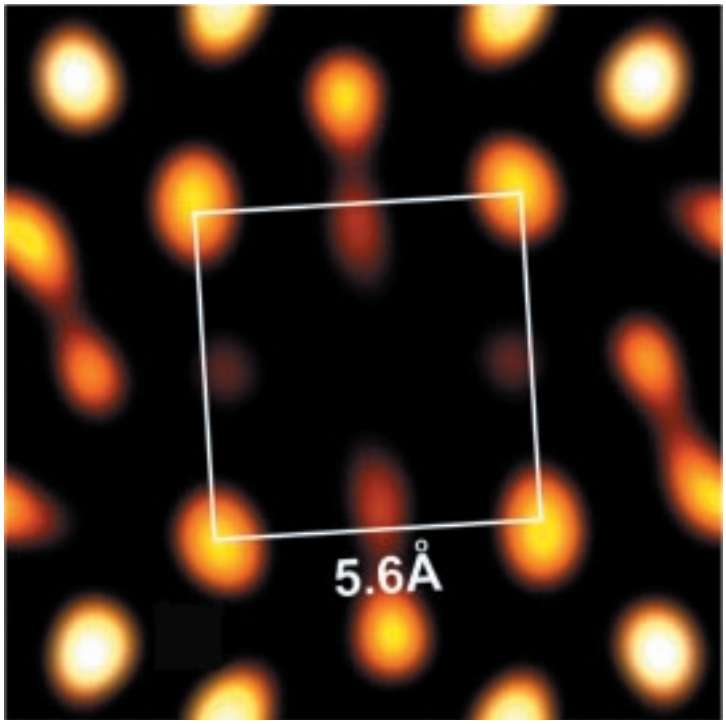

Figure 3 **(b)** Reconstructed image of the (001) plane of gallium atoms. The white square depicts a crystal unit cell.

separation of Ga $K\alpha_{1,2}$ emission lines [7].

The experiment has been carried out on the diffraction beamline of the ELETTRA synchrotron radiation source in Trieste. The energy of the incident beam was selected with a double-crystal Si(111) monochromator. The sample was a thin slab of GaAs single crystal cut parallel to (001) crystallographic planes. It has a zincblende structure with a lattice parameter of 5.654 Å. The experimental setup is shown in Fig. 2. The sample was mounted on a four-circle goniometer. The ω-circle was used to change the angle of incidence in the range $0° \le \omega \le 75°$, the χ-circle rotated the sample in the azimuthal direction $0° \le \chi \le 180°$. The step in ω was $\Delta\omega = 2.5°$, the step in χ depended on ω approximately as $\Delta\chi=\Delta\omega/\sin\omega$. Moreover the sample was mounted on a special holder, performing a continuous precession movement during the measurement; the angle of precession was set to 1.2°. This movement of the sample works as a two-dimensional low-pass filter smoothing out the contributions from distant scatterers to the hologram. A zinc foil of thickness of 75 μm was placed in front of a detector which was mounted on the ω-circle at a distance of 60 mm from the sample. The detector was an AXUV-100 silicon photodiode produced by International Radiation Detectors Inc. with a sensitive area of 100 mm^2. A photocurrent corresponding to $5 \cdot 10^6$ photons/s was measured, which is about one order of magnitude higher than what could be achieved with a graphite analyzer or an energy dispersive detector under the same conditions.

In order to demonstrate the feasibility of this experimental method for XFH measurements, the fluorescence pattern for an energy of 11.5 keV was measured. The data were collected for 1344 directions of the incident wave vector, 5s for each one. The frequency of the sample precession was set to 1 Hz. Measured data were normalized to the incident beam, monitored by means of an ionization chamber and corrected for variations in absorption at different ω angles by means of a two-dimensional Savitzky-Golay high-pass filter. After subtracting the uniform fluorescence background and filtering out the sharp pattern corresponding to X-ray standing wave lines and noise, the hologram depicted in Fig. 3a was obtained. The real-space reconstruction was performed by using the formula (2) and the images of nearest neighbors of gallium atoms were obtained. As an example, the image of the (001) plane of gallium atoms is shown in Fig. 3b. Twenty neighbors of the emitter (which, obviously, is not seen in the center) are clearly visible, the interatomic distances of the nearest atoms are in a good agreement with the lattice parameter.

CONCLUSION

The selection of radiation emitted by gallium atoms by means of a thin zinc foil resulted in a signal corresponding to a rate of several millions photons per second. Evidently, a further significant increase of the signal can be achieved by using a larger detector with higher quantum efficiency, thus making possible the collection of holographic images in times limited only by the speed of goniometer motors.

It is obvious that experimental configurations with detection of photons within a narrow energy window cannot always be replaced with the method of absorption filters. However, in many cases, suitable thin foil filters are available and then the technique of absorption filters coupled to an optimal detector reduces drastically the duration of experiments and makes it possible to measure data with better statistics. The improvement of data precision allows the recording of holographic signals from weaker scatterers and to get images of lighter atoms.

References:

[1] A. Szöke; *Short Wavelength Coherent Radiation: Generation and Applications*, editors T. Attwood and J. Boker, AIP Conference Proceedings 147 (AIP, New York, 1986)
[2] For a review on the subject, see C. S. Fadley, *Surface Science Reports* 19, 231 (1993)
[3] M. Tegze and G. Faigel; *Nature* ; 380, 49, (1996)
[4] T. Gog, P. M. Len, G. Materlik, D. Bahr, C. S. Fadley, C. Sanchez-Hanke; *Physical Review Letters*; 76, 3132, (1996)
[5] B. Adams, D. V. Novikov, T. Hiort, G. Materlik; *Physical Review B*; 57, 7526, (1998)
[6] M. Tegze, G. Faigel, S. Marchesini, M. Belakhovsky, A. I. Chumakov; *Physical Review Letters*; 82, 4847, (1999)
[7] E. Busetto, M. Kopecky, A. Lausi, R. H. Menk, M. Miculin, A. Savoia; *Physical Review B*; 62, 5273, (2000)
[8] J. J. Barton; *Physical Review Letters*; 61, 1356, (1988)

Near Node Photoelectron Holography: Images of real space with atomic resolution

J. Wider, F. Baumberger, T. Greber, J. Osterwalder
Physik Institut der Universität Zürich, Winterthurerstr. 190, CH—8057 Zürich, Switzerland

M. Sambi,
Università di Padova, Dipartimento di Chimica Inorganica, Metallorganica ed Analitica, Via Loredan 4, I—35131 Padova, Italy

R. Gotter , A. Verdini,
Laboratorio TASC, Istituto Nazionale per la Fisica della Materia, Basovizza SS14 Km 163.5, I-34012 Trieste, Italy

F. Bruno, A. Morgante,
Laboratorio TASC, Istituto Nazionale per la Fisica della Materia, Basovizza SS14 Km 163.5, I-34012 Trieste, Italy
Department of Physics, University of Trieste, Via Valerio 2, I-34100 Trieste, Italy

D. Cvetko ,
Sincrotrone Trieste, Italy
Jozef Stefan Institute, Department of Physics, Ljubljana University, Ljubljana, Slovenia

INTRODUCTION

Holography records and reconstructs the complete geometric information of three dimensional objects from diffraction patterns. The phase and amplitude of the wave field is reconstructed from the measured intensity of the object wave that interfered in the detector with a known reference wave [1]. Photoelectron diffraction has all the prerequisites of a holographic experiment [2, 3]. For electron kinetic energies above 150 eV ($\lambda_e \leq 1$Å) forward scattering dominates the diffraction process between the photoelectron and the surrounding atoms. Since this is zero a order diffraction feature it contains no holographic information and is thus a major obstacle for the holographic interpretation of such data. Forward scattering can be suppressed if the anisotropic nature of the photoelectron source waves is exploited [4]. Figure 1 compares single scattering calculations for an Al dimer for two different experimental setups. In the near node geometry the angle γ between the polarization of the light and the direction of detection is 80°. In the far node geometry these two directions are parallel. The diffraction patterns of the far node geometry are dominated by forward scattering at $\vartheta = 0°$. In the near node geometry the interference features at $\vartheta \neq 0°$ are more pronounced relative to the forward scattering peak. In order to fulfill the near node condition for the whole diffraction pattern, the angle γ must be constant during the whole experiment.

RESULTS AND DISCUSSION

The experiments have been performed in August 1999 at the ALOISA beamline [5]. Atomically clean Al(111) surfaces have been prepared using standard techniques. The fcc structure with a nearest neighbor distance of 2.86 Å is well known and no surface reconstruction occurs. The experiments were performed at room temperature. The Al 2s diffraction data sets contain about 1600 data points evenly spaced in $2\pi/3$ from normal emission down to a polar angle of 70°.

With the photon energy of 1070 eV and the binding energy of the Al 2s core level (118 eV), the electron wavelength becomes 0.4 Å. Two orientations of the linear light polarization were used. The horizontal polarization vector, the surface normal and the direction of detection lie in a single plane. In the near node geometry the angle γ between the detector and the polarization was set to 80° and in the far node geometry to 0°. The far node geometry data serve for comparison, the absolute determination

of the crystal orientation and the compensation of the residual vertical polarization component that was determined to be about 5 %. The subtraction of the photoemission intensity of the vertical polarization is allowed since the horizontal and vertical polarization components contribute incoherently. In order to remove the polar angle dependence of the instrumental response function, the azimuthal data sets, (Figure 2 a and c) are normalized for every polar emission angle.

Figure 2 demonstrates near node photoelectron diffraction with experimental data. The angular Al 2s photoemission intensities for the far node and the near node geometry are stereographically projected in Figure 2 a) and c). White corresponds to highest and black to lowest intensity. From comparison with Figure 2 b) which shows the corresponding real space projection of a fcc crystal on the (111) plane it is seen that the far node diffraction pattern can be regarded as a projection of nuclear charge along the nearest neighbor directions. The forward scattering focuses intensity along nearest neighbors and thus causes high intensity along low index atomic chains and planes [6]. This correspondence is not seen in the near node diffraction pattern (Figure 2 c) and thus indicates suppression of forward scattering. In order to get real space images of the emitter's environment the diffraction patterns are holographically interpreted by the Stuck algorithm [7]. The image function $|rU(r)|^2$ is shown after a convolution with a Gaussian with 1 Å full width at half maximum. In the near node geometry the holographic reconstruction of real space around the emitter in the (111) plane clearly reveals the positions of the surrounding atoms. In Figure 2 f) nearest, next nearest and even second next nearest neighbor positions are resolved as local maxima in the image. This is not the case for the far node geometry data where no distinct atomic positions can be assigned. As usual in inside source holography, the emitter sits at the origin of the image and is not reproduced.

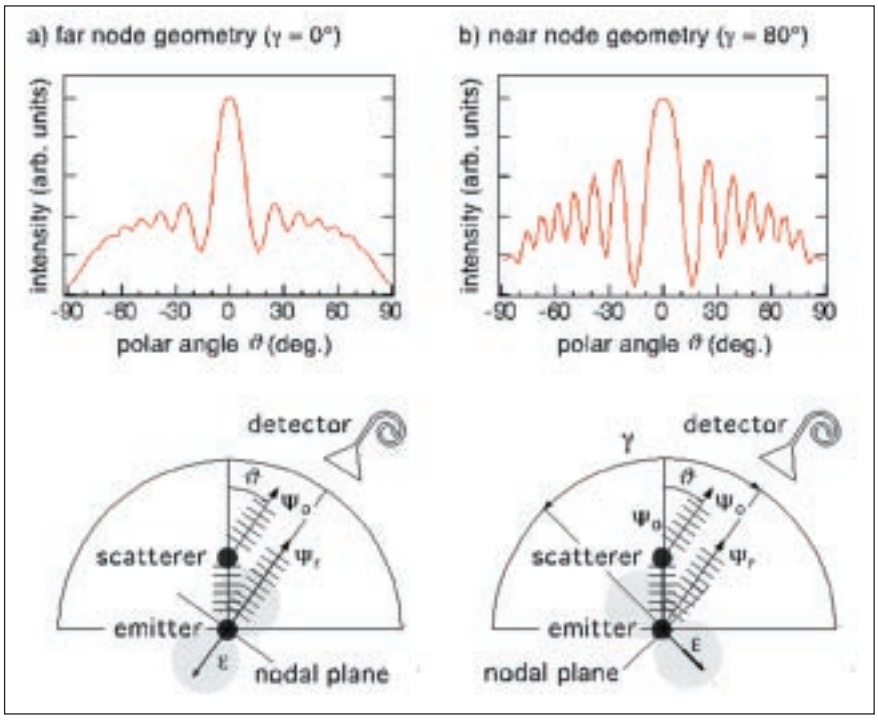

Figure 1. Principle of photoelectron holography and near node photoelectron holography illustrated for an atomic aluminum dimer. The scattered object wave Ψ_o and the unscattered reference wave Ψ_r interfere in the detector and form, if measured at many different angles, a hologram. The holograms are simulated with single scattering calculations: The Al 2s emitter is 2.86 Å away from the Al scatterer (object) and produces a p-wave with a wavelength of 0.4 Å. The situations for two different orientations γ of the light polarization ε relative to the electron detector are shown. These angles γ remain fixed during the recording of the hologram. In the far node geometry (γ = 0°), a), the diffraction is dominated by the forward scattering at ϑ = 0°. In the near node geometry, b), where the angle γ is 80°, the higher order interference fringes at ϑ≠ 0° are strongly enhanced, relative to the forward scattering.

J. Wider, F. Baumberger, M. Sambi, R. Gotter , A. Verdini,
F. Bruno, D. Cvetko, A. Morgante, T. Greber, J. Osterwalder

The nearest neighbor distances in the holographic reconstruction (Figure 2 f) are overestimated by about 15 %. This is due to the atomic scattering phase shifts that imply larger and anisotropic scattering paths.

The successful proof of the principle of Near Node Photoelectron Holography paves the way for direct structure determination at surfaces. It is expected that unknown structures of unit cells with a size of more than 10 Å may be solved.

ACKNOWLEDGMENTS

It is a pleasure to acknowledge the Istituto Nazionale per la Fisica della Materia (INFM) for beamtime and hospitality and the Swiss National Science Foundation who supports this project.

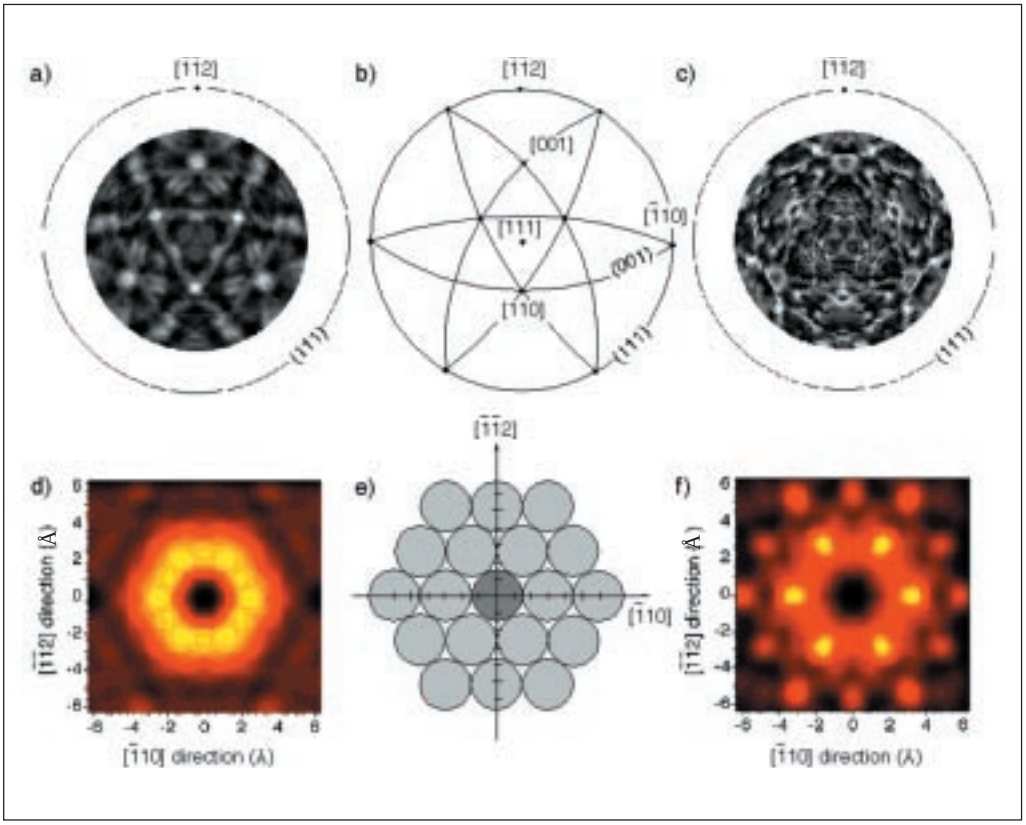

Figure 2. Comparison of far node and near node photoelectron diffraction data and their holographic reconstructions. a) and c) Stereographically projected experimental Al 2s (E_{kin} = 942 eV) photoelectron diffraction patterns from an Al(111) single crystal for the far node and the near node geometry. In the far node geometry (a) forward scattering dominates the pattern as can be seen from the stereographic projection of the high density crystal chains and planes in (b).In the near node diffraction pattern (hologram) no distinct forward scattering features are visible. d) and f) Corresponding holographic real space reconstructions of a plane parallel to the surface that contains the emitter (inside source) at (0,0).They should show the expected image of an Al(111) plane (e).In the near node reconstruction (f) nearest, next nearest and second next nearest neighbors are clearly resolved as local maxima while in the far node picture (d) no clear atom positions can be seen.

References:

[1] D. Gabor, Nature **161** (1948) 777.
[2] A. Szöke, in: Short Wavelength Coherent Radiation: Generation and Applications, Eds. D. T. Atwood and J. Boker, AIP Conf. Proc. 147 (AIP, New York, 1986).
[3] J. J. Barton, Phys. Rev. Lett. **61** (1988) 1356.
[4] T. Greber, J. Osterwalder, Chem. Phys. Lett. **256** (1996) 653.
[5] L. Floreano, G. Naletto, D. Cvetko, R. Gotter, M. Malvezzi, L. Marassi, A. Morgante, A. Santaniello, A. Verdini, F. Tommasini and G. Tondello, Rev. Sci. Instrum., **70**, (1999) 3855.
[6] C.S. Fadley, Surf. Sci. Rep., **19**, (1993) 231.
[7] A. Stuck, D. Naumovic, H.A. Aebischer, T. Greber, J. Osterwalder, L. Schlapbach, Surf. Sci. **274** (1992) 441.

J. Wider, F. Baumberger, M. Sambi, R. Gotter , A. Verdini, F. Bruno, D. Cvetko, A. Morgante, T. Greber, J. Osterwalder

Selforganization and transport mechanisms of alkali metals on a catalytic metal surface

H. Marbach, B. Luerßen, R. Imbihl,
Institut für Physikalische Chemie und Elektrochemie, Universität Hannover, Callinstr. 3 - 3a, D-30167 Hannover, Germany

L. Gregoratti, M. Kiskinova, S. Günther,
Sincrotrone Trieste, Italy

Alkali metals play a prominent role in heterogeneous catalysis due to their function as promoters. Without exhibiting substantial catalytic activity themselves they can enhance strongly the efficiency of certain transition metal catalyst. However, in order to understand and correctly predict the role of alkali promoters in surface reactions we still lack insight into the spatial organization of the alkali coadsorption systems on different length and time scales. Crucial for the documentation of these events has been the chemical identification of the imaged surface species by means of scanning photoelectron microscopy (SPEM). Direct evidence that under reaction conditions selforganization processes associated with alkali mass transport take place leading to a heterogeneous surface with large scale structures in the micrometer range has been obtained. The spatial distribution of potassium on a Rh(110) surface during the catalytic $O_2 + H_2$ reaction is investigated. It has been found that depending on the reaction conditions potassium, which is initially homogeneously distributed, condenses reversibly into macroscopic islands, where it is coadsorbed with oxygen. The mass transport of potassium proceeds via propagating reduction fronts leading to the stationary concentration pattern as final state, illustrated by the K 2p map shown in Fig. 1. Differences in the mobility and in the bonding strength of potassium on the 'reduced' and on the 'oxidized' surface areas are found to be the key factors for the condensation process. In heterogeneous catalysis numerous alkali promoted reaction systems exist where electron-acceptor coadsorbates (e. g. O, N, OH etc.) are present forming stable coadsorption complexes and affecting the mobility of the alkali metal in a similar way as in the example presented above. The processes observed here should therefore be important for a broad class of catalytic systems.

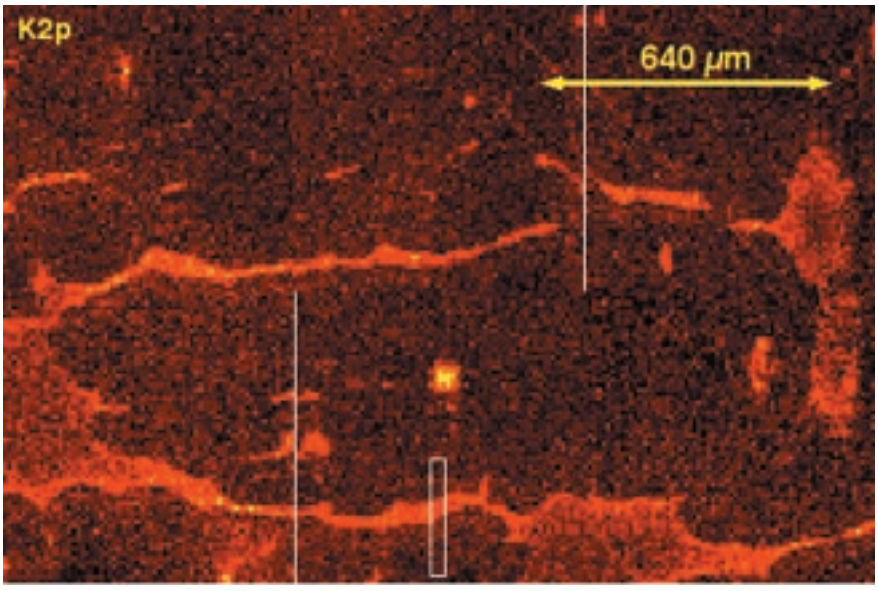

Figure 1. Large scale K 2p image showing the stationary inhomogeneous K distribution reached in the final stage of condensation process.

Morphology, chemistry and electronic properties of an Au/n-GaN interface

A. Barinov, L. Casalis, L. Gregoratti, M. Kiskinova,
Sincrotrone Trieste, Italy

Formation of stable metal contacts is a challenge faced by GaN-based technology producing devices for high-temperature applications. Still it is not much known about the morphology and chemistry developed at GaN-metal interfaces at elevated temperatures and their effect on the local electric properties. Employing synchrotron radiation photoelectron specromicroscopy, which provides chemical and electronic information from sub-μm surface areas, has enabled us to identify composition heterogeneity developed at the Au/n-GaN interface at high temperatures and investigate its effect on the local Schottky barrier heights.

Figure 1 shows an Au 4f image of an area where composition inhomogeneity has been developed. The three grains with different Au coverage relate to the defective GaN microstructure. The dark spot between the grains is a topographic defect, caused by the released nitrogen during the Au-GaN reaction, which leads to degradation of the GaN epilayers. The Ga 3d spectra taken from spots inside the grains reveal that the reaction has advanced to different extent: fraction of the released Ga has formed Au gallide, resulting in a distinctive component in the Ga 3d spectra, Ga(Au), whereas the excess of Ga segregates on top of the Au gallide layer.

The different composition of the metal layer reflects the local reactivity of the grains and the mass transport of Au to the more reactive areas. The most peculiar finding is that the reaction-induced heterogeneity at the interface does not lead to the expected variations in the Schottky barrier heights. This indicates that the interfacial layer should be homogeneous. Indeed, the SPEM measurements confirmed that the composition of the gallide phase changes with advancement of the reaction until the Ga-richest $AuGa_2$ stoichiometry is established and the excess Ga appears as metallic. It is the $AuGa_2$ interfacial layer that controls the Schottky barrier heights of the heterogeneous area shown in Fig. 1 and the observed heterogeneity is related to different thickness of the $AuGa_2$ layer and segregated Ga on top.

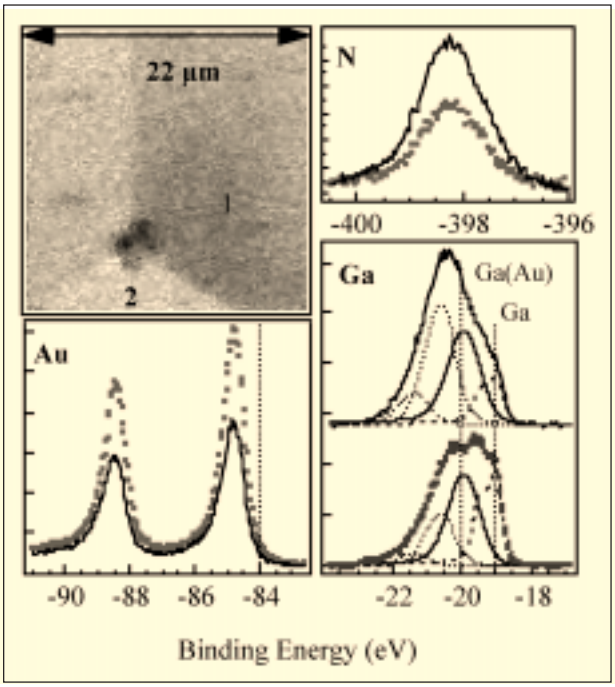

Figure 1. Au $4f_{7/2}$ image of an Au/GaN interface after annealing to 820 C and the Au 4f, N1s and Ga 3d spectra measured in position '1' (full lines) and '2' (dotted lines).

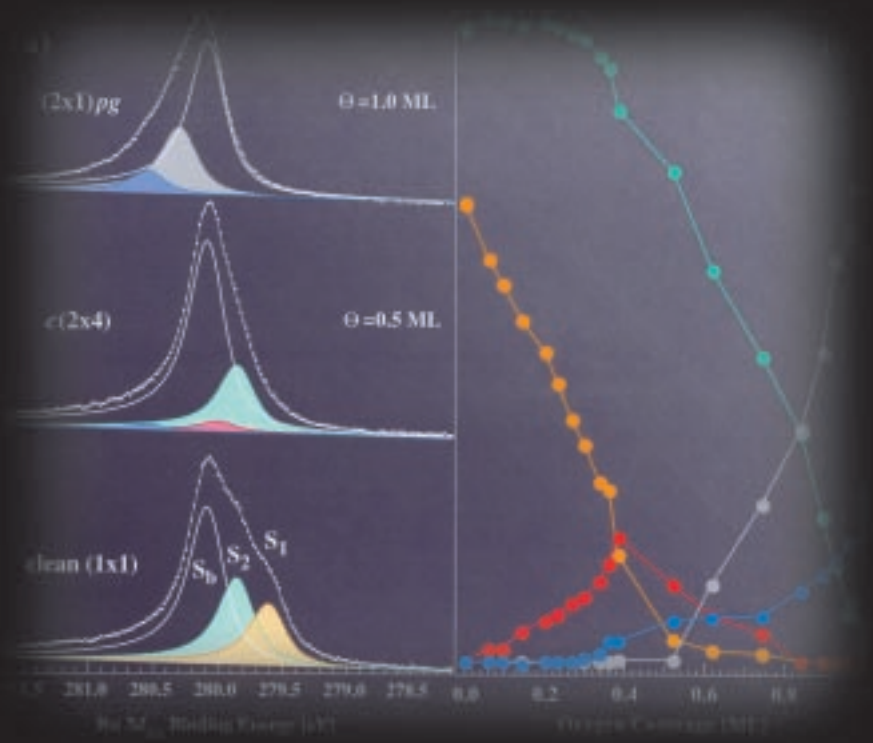

Electronic Structure of Surfaces

Synchrotron radiation plays a crucial role in the understanding of the electronic structure of matter. Photoelectron spectroscopy in particular benefitted greatly of synchrotron radiation because of its unique properties, in particular its tunability which allows to choose the appropriate photon energy for each measurement. However it should not be forgotten that excellent work can be done with laboratory sources to complement synchrotron radiation sudies.
At ELETTRA, most experimental stations for photoemission are equipped also with conventional sources to extend their capabilities in terms of photon energy range and to perform experiments during machine maintenance periods. This paper presents interesting data obtained using a Helium discharge lamp in one of the experimental stations of the APE beamline, which is currently under construction. The data show an interesting new propertiy of C60 monolayers and highlight the excellent performances of the instrumentation.

Temperature-dependent Fermi Gap Opening in the *c*(6x4)-C_{60}/Ag(100) Two-dimensional Superstructure

I. Vobornik, C. Cepek, G. Panaccione, M. Sancrotti[*]
Laboratorio Nazionale TASC-INFM, Area Science Park, S.S. 14, km 163.5 Basovizza, I-34012 Trieste, Italy
(*) also at Dipartimento di Matematica e Fisica, Università Cattolica del Sacro Cuore, Via dei Musei 41, I-25121 Brescia, Italy

J. Kröger,
Physik-Institut der Universität Zürich, CH-8057 Zürich, Switzerland

G. Selvaggi, G. Rossi,
Dipartimento di Fisica, Università di Modena e Reggio Emilia, Via Campi 213/A, I-41100 Modena, Italy

The discovery of fullerides, and in particular of superconductivity in some alkali or rare earth doped bulk C_{60} systems [1, 2], initiated one of the notably active research fields in solid state physics. Recently a major attention was dedicated to the characterization of low-dimensional ordered C_{60} films [3, 4]. This is due to the important finding that the superconductivity persists in the C_{60} surface (mono)layer with a T_c as high as the one in three-dimensional bulk systems.

Currently little is known about the electronic structure of the films. We performed high-resolution photoemission investigation of the electronic properties of one monolayer (ML) C_{60} grown on the top of the Ag(100) surface. We observe the opening of an energy-gap at the Fermi level when the temperature is lowered from 260 K to 25 K. The gap opens and closes reversibly while no changes in the geometric arrangement of the fullerene superstructure are observed.

High-resolution photoemission from the valence band was performed at the low-energy experimental station of the APE beamline, currently under construction at Elettra. This system is equipped with a Scienta SES-2002 electron energy analyzer and a high-stability He discharge lamp ($h\nu$ = 21.2 eV). The overall instrumental energy resolution is better than 10 meV.

The clean and well ordered 1ML C_{60}/Ag(100) system was obtained by a standard procedure [5]. The surface quality was checked via photoemission, Auger electron spectroscopy (AES), and low energy electron diffraction (LEED). Because of the small Brillouin zone (~6°) and the scattering effects due to a large number of C atoms per molecule, the reported photoemission spectra represent electrons scattered over all k-vectors within the first Brillouin zone.

A series of photoemission spectra from the 1ML C_{60}/Ag(100) is given in Fig. 1 as a function of temperature. All spectra are referenced to the Fermi level (E_F), which was determined independently from the spectra measured on a polycrystalline Ag sample

at four different temperatures over the spanned temperature range. The E_F position remained stable (within ±1 meV) during the measurement time. By each spectrum of Fig. 1 we also show the Fermi-Dirac distribution function at a given temperature. The spectra from the 1ML C_{60}/Ag(100) superstructure are characterized by a broad peak near E_F, which represents a portion of the lowest unoccupied molecular orbital (LUMO). This orbital is partially filled by the electronic charge transferred from the Ag substrate to the C_{60} cages. Therefore, the LUMO-related emission at 300 K exhibits a clear Fermi edge, indicating a metallic state of the 1ML C_{60} ordered layer [6].

We notice that the emission close to E_F cannot be due to the substrate since the C-related features are definitely favored in terms of the relative photoionization cross-sections at hν=21.2 eV ($\sigma_{Ag\ 5s}/\sigma_{C\ 2p} \approx 0.03/6$) [7]. We also point out that the escape depth associated with the photoelectrons of Fig. 1a and 1b favors the adlayer-related contribution with respect to the substrate.

From ~250 K downward a progressive depletion of the photoemission intensity close to E_F occurs. At the same time the spectral weight accumulates at higher binding energy, giving rise to an unambiguous energy gap opening at E_F. This is emphasized in Fig.1c, where the symmetrized spectra are shown, following the practice developed for analysis of the gap evolution in high-T_c cuprates [8].

Again inheriting the procedure from high-T_c superconductors, we determine Δ as a shift of the spectral leading edge from E_F [9]. We recall that this procedure gives only a measure of the gap, while the real gap should be determined by fitting the spectra with a known density of states (DOS). Fig. 2 illustrates Δ vs. temperature. It increases/decreases monotonously, reaching a value of ~10 meV at T ≤ 70 K.

The mechanism(s) governing the gap opening from Fig. 1 is (are) unknown at present. Different scenarios can be speculatively proposed. The line shape analysis of the fine structure of the LUMO-related photoemission spectra allowed us to measure the electron-phonon (e-ph) coupling in 1ML C_{60}/Ag(100) [6]. The total e-ph coupling constant (lÅ1.14) and the role of relevant multi-phonon replicae suggest that this system belongs to the intermediate to strong e-ph coupling limit.

A lack of the transport data does not allow deciding whether this strong e-ph coupling give rise to superconductivity. From Fig. 1a it is quite evident that, along with the progressive sharpening of the spectral leading edge, the decreasing temperature induces a highly peaked emission at ~30-35 meV binding energy. This spectral evolution is similar to the one in high-T_c cuprates when going from normal

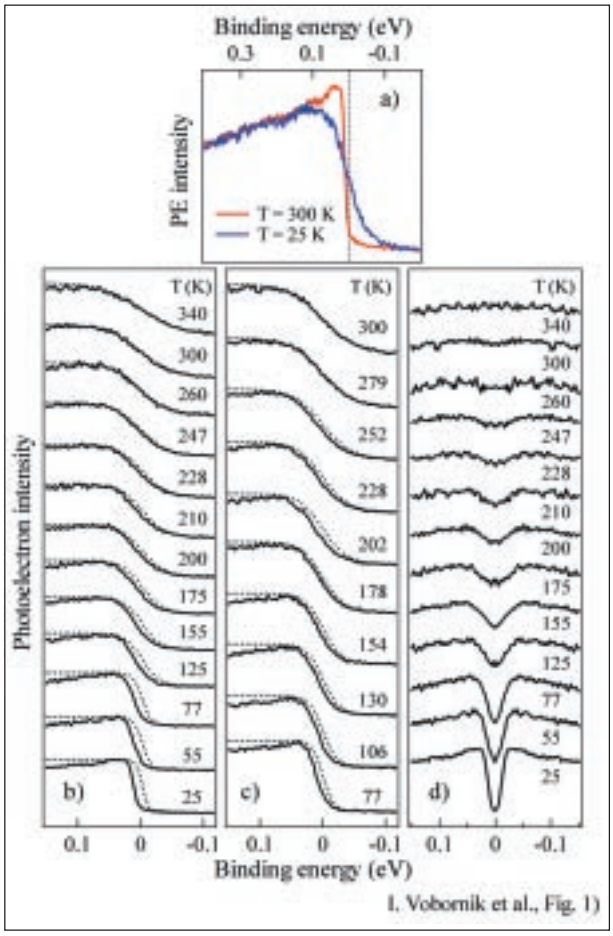

Figure 1. (a) Valence band photoemission spectra (normalized to the photon flux) of the LUMO-related spectral feature in 1ML C_{60}/Ag(100) at 300 K and 25 K; same spectra taken as a function of (b) increasing temperature, (c) decreasing temperature (normalized to the maximum intensity); (d) Symmetrized spectra from (b) illustrating the opening of a gap at E_F.

to the superconducting state [10]. Evidence from photoemission for the superconducting transition in bulk C_{60} fullerides was reported before for K_3C_{60} and Rb_3C_{60} [4, 11]. The report by Hesper et al. [4], in particular, points out the change in the line-shape consistent with the transition to the superconducting state. This line-shape evolution corresponds to the one observed in Fig. 1a.

In the BCS framework, the ratio $2\Delta_{SC}/k_BT_c$ = 3.528 would imply an energy gap as large as ~70 meV. Interestingly, the spectra do show an intensity pile-up at the binding energy corresponding to one half of such a gap (Δ_{SC}=35 meV), as expected for the condensate peak in the superconducting samples.

The critical temperature where the gap opens is at least 100 K higher than any critical

I. Vobornik, C. Cepek, G. Panaccione, M. Sancrotti, J. Kröger, G. Selvaggi, G. Rossi

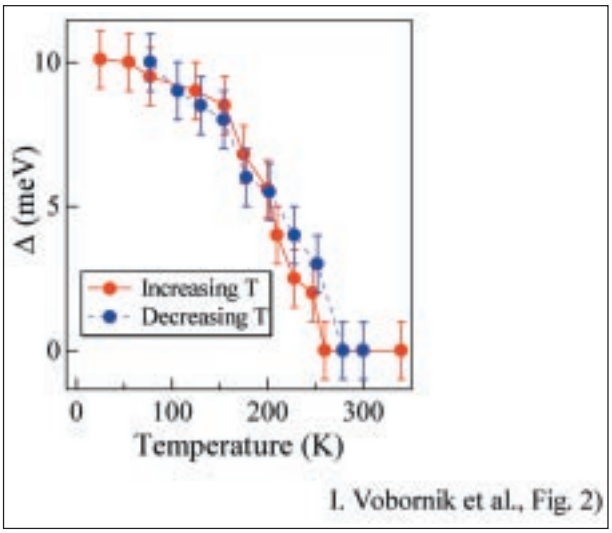

Figure 2. Gap measured as a shift of the spectral leading edge from E_F vs. temperature.

superconducting temperature measured so far (Fig. 2) [12]. However, in the presence of the strong correlation effects, the temperature where the gap opens does not necessarily need to coincide with the superconducting T_c. In fact, the most peculiar behavior in the high-T_c cuprates occurs in the low doping regime, where a normal state gap (pseudogap) is found to persist at temperatures as high as ~250 K [13].

Other features of 1ML C_{60}/Ag(100) seem also to favor the provocative superconducting scenario. The C_{60}-C_{60} distance in the overlayer is ~10.42 Å. Keeping in mind that the T_c in C_{60} superconducting materials scales with the buckyball-buckyball distance [14], this number should be compared with 10.03 Å in the non-superconducting face-centered-cubic C_{60} and in particular with 10.40 Å in the highest-T_c Cs_3C_{60} [15, 16].

In conclusion, high-resolution photoemission data reveal evidence for a temperature-dependent gap opening in the 1ML C_{60}/Ag(100) system. This result is of particular significance in the light of the recently revealed importance of the surface layer to the superconductivity in the C_{60} based superconductors. The possible explanations for the observed behavior range from the strong correlation effects, superconductivity (with extremely high T_c) or a combination of the two. At this early stage of investigation, different scenarios cannot be excluded either. In order to distinguish between the different mechanisms either transport data or a correct form of the DOS at low T is crucial. Existing experimental and theoretical work, mainly based on the three-dimensional bulk systems, will need to be extended to the low dimensional structures in order to truly understand the peculiar properties of the C_{60} systems.

References:

[1] R.M. Fleming *et al.*, Nature 352, 787 (1991)
[2] O. Gunnarsson, Rev. Mod. Phys. 69, 575 (1997)
[3] J.H. Schön, Ch. Kloc, R.C. Haddon, B. Batlogg, Science 288, 656 (2000)
[4] R. Hesper, L.H. Tjeng, A. Heeres, G.A. Sawatzky, Phys. Rev. Lett. 85, 1970 (2000)
[5] C. Cepek, PhD Thesis, Zürich 2000
[6] A. Goldoni *et al.*, Phys. Rev. B 58, 2228 (1998)
[7] J. J. Yeh and I. Lindau, Atomic Data and Nuclear Data Tables, 32 (1985)
[8] M.R. Norman *et al.*, Nature 392, 157 (1998)
[9] J.M. Harris *et al.*, Phys. Rev. Lett. 79, 143 (1997)
[10] J.M. Imer *et al.*, Phys. Rev. Let.. 62, 336 (1989)
[11] C. Gu *et al.*, Phys. Rev. B 50, 16566 (1994)
[12] A. Schilling, M. Cantoni, J.D. Guo, H.R. Ott, Nature 363, 56 (1993)
[13] H. Ding *et al.*, Nature 382, 51 (1996)
[14] T. Yildrim *et al.*, Solid State Commun. 93, 269 (1995)
[15] M.-Z. Huang, Y.-N. Xu, W.Y. Ching, Phys. Rev. B 46, 6572 (1992)
[16] T.T.M. Palstra *et al.*, Solid State Commun. 93, 327 (1995)

I. Vobornik, C. Cepek, G. Panaccione, M. Sancrotti, J. Kröger, G. Selvaggi, G. Rossi

Atomic adsorption site identification by means of High-Energy Resolution Surface Core Level Shift: oxygen on Ru(10$\bar{1}$0)

A. Baraldi, S. Lizzit, G. Paolucci,
Sincrotrone Trieste, Italy

INTRODUCTION

The knowledge of the geometrical structure of atoms and molecules adsorbed on metal and semiconductor solid surfaces is an important step to the understanding of gas-surface interactions which are the basis of heterogeneous catalysis. This has stimulated the development of a large number of experimental techniques devoted to surface structural investigations. The identification of the adsorption site normally requires a large effort in terms of experimental measurements and/or data analysis. For example diffraction techniques such as Low Energy Electron Diffraction (LEED) and Photoelectron Diffraction (PhD) need complex and time-consuming computer calculations, based on guessed trial structures. Also X-ray Photoelectron Spectroscopy (XPS) has been used to study the adsorption site of atoms and molecules. It is well known that core level binding energies are influenced by different adsorbate-substrate environments. The core levels of chemisorbed atoms and molecules are very sensitive to the adsorption site and additionally the core level binding energies of the substrate atoms are influenced by the adatoms [1]. The experiments have revealed the high sensitivity of the Surface Core Level Shift (SCLS) measurements to different geometrical configurations. SCLS investigations have been performed in order to study the reconstruction process, to probe the local overlayer structure of chemisorbed molecules or to study the role of the different coordination of the atoms at the steps. However, until now it was not possible to identify directly the adsorption site. The High-Resolution Core Level Spectroscopy measurements reported here reveal in a straightforward way that oxygen chemisorbs on Ru(10$\bar{1}$0) in a three-fold hcp site and permit an understanding of the interaction of the oxygen adatoms not only with the top layer Ru atoms but also with the second layer ones.

Previous results have shown that three components in the $3d_{5/2}$ core level of Ru(10$\bar{1}$0) clean surface are unusually present, originating from first, second-layer and bulk atoms [4]. This effect makes it possible to follow the evolution of the different Surface Core Level Shifted components - which reflects the changes in the oxygen interaction with first and second layer Ru atoms - thus giving information on the adsorption site.

The Ru $3d_{5/2}$ core level spectra were measured at the SuperESCA beamline of Elettra. The overall experimental resolution (monochromator and electron energy analyzer) was 65 meV at a photon energy of 380 eV.

As previously observed by Poulsten *et al.* [2] and Schwegmann *et al*. [3] oxygen adsorption at 300 K on Ru(10$\bar{1}$0) induces the formation of two ordered structures: a *c*(2x4) and a (2x1)*pg*. We calibrated the surface coverage by measuring while oxygen dosing the integrated intensity of the O1*s* peak, assuming the saturation coverage corresponding to the best (2x1)*pg* structure to be 1 ML. We found the coverage of the *c*(2x4) to be 0.51±0.02 ML.

Unfortunately the O1s core level energy is not useful to make any assignment of the adsorption site, because when the structure changes from c(2x4) to (2x1)*pg*, the binding energy shifts by 75±10 meV. The only conclusion is that oxygen sits in the same location in the two ordered structures. The ten structures depicted in Fig. 1 are the most plausible among those compatible with a c(2x4) LEED pattern. Oxygen can sit in the threefold hcp, threefold fcc, on-top or bridge sites forming ordered arrangements with atoms bonded with ruthenium atoms of the first layer only (Ru_1-O), second layer only (Ru_2-O) or simultaneously with both.

Our approach for understanding the adsorption site of the ordered structures implies the measurement of the Ru SCLS at different oxygen coverages. Since the clean Ru(10$\bar{1}$0) surface shows three components which belong to first- (S_1), second-layer (S_2) and bulk atoms we expect to distinguish in the core level spectra peaks originating from oxygen multiple-coordinated Ru atoms of both, first and second layers.

Figure 2(a) shows three Ru $3d_{5/2}$ spectra selected of the whole set collected during oxygen exposure at 300 K corresponding to the clean (1x1), *c*(2x4) and (2x1)*pg* surface structures. For the clean surface (Fig. 2(a) bottom) three peaks appear named S_b, S_1 and S_2: as shown in Ref. [4] they arise from the bulk and the first two surface layer atoms. The first-layer peak (S_1) is shifted by -480±20 meV from the bulk peak position and the second peak (S_2) by 240±20 meV. By increasing the oxygen coverage the peaks of the clean surface decrease in intensity and

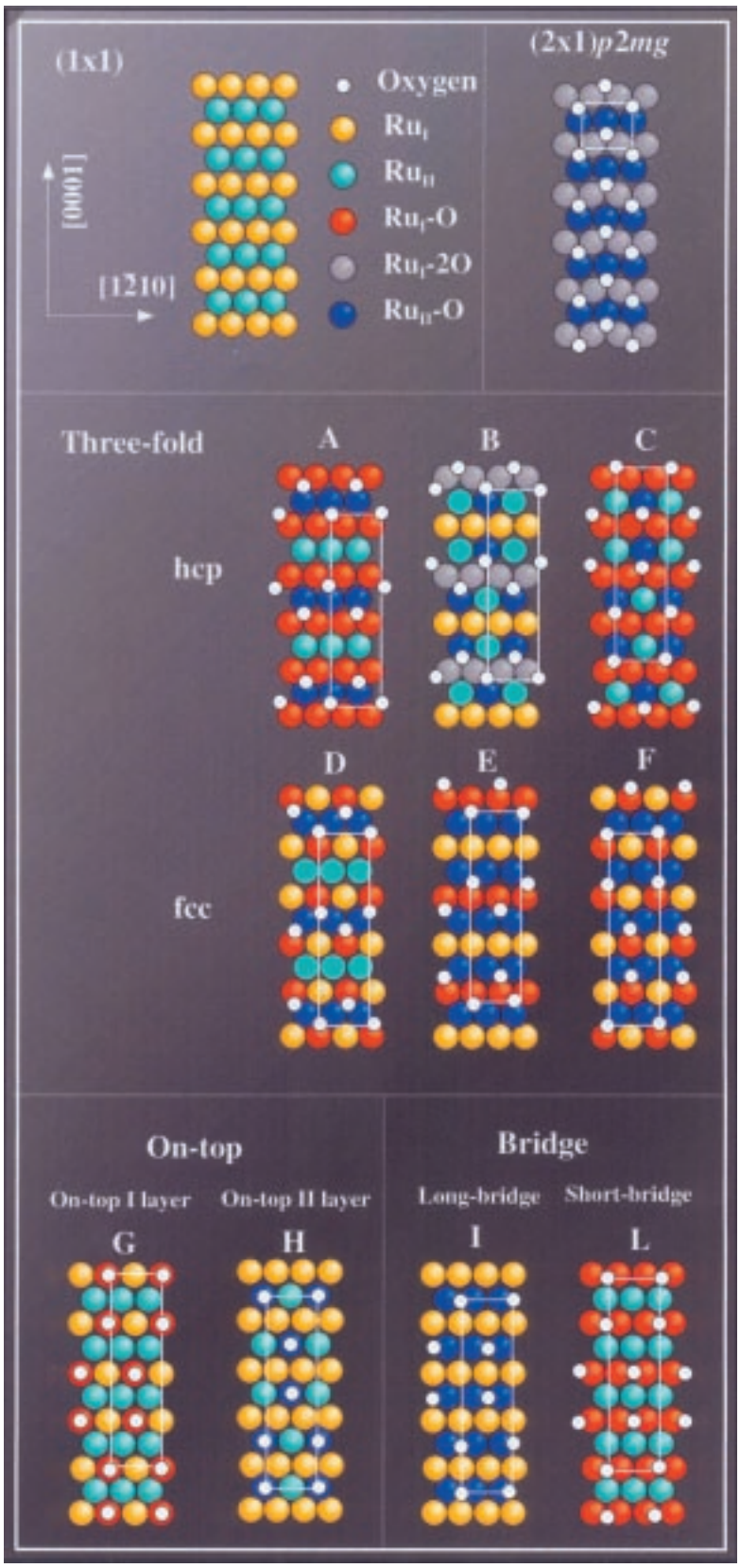

Figure 1. *Possible models for the Ru(10$\bar{1}$0)-c(2x4)-2O structure, with oxygen sitting in: three-fold hcp, three fold fcc, on-top and bridge adsorpion sites.*

new peaks appear at higher binding energies, as shown in Fig. 2(a).

Quantitative assessment of the data was obtained by fitting the spectra with a Doniach-Sunjic (DS) function The best fits parameter values were 0.27±0.02 eV, 0.095±0.020 and 140±20 meV for Γ (Lorentzian width), α (Anderson singularity index) and the Gaussian width, respectively.

The results of the analysis of the whole set of data are shown in Fig. 2(b). For coverages below 0.5 ML oxygen adsorption induces a strong decrease of the Ru_1 component, which nearly disappears on the completion of the c(2x4) phase. At this coverage Ru_2 peak is still present, even though with reduced intensity. In the same coverage range two other components (red and blue curves), at -85±20 meV and 465±20 meV, gain intensity with respect to the bulk peak, but just above 0.5 ML they behave in a different way: the red curve decreases and disappears at saturation, while the blue curve increases and reaches maximum intensity at oxygen saturation. It is important to note that a new component (gray curve) shifted by 215±20 meV with respect to the bulk peak grows at coverage larger than 0.5 ML and reaches the maximum in correspondence of the (2x1)*pg* structure.

For the interpretation of these results we assume that the only modified Ru atoms are those bonded with one or two oxygen adatoms. The first important result of the data analysis is that Ru_1 (yellow curve) goes to zero on completion of the *c*(2x4) structure at 0.5 ML. Among the possible *c*(2x4) structures reported in Fig. 1 we immediately exclude those which have unperturbed first-layer Ru atoms (orange atoms). In other words, we can exclude the three-fold fcc site (models D, E and F), the on-top site (models G and H), the long-bridge site (model I) and model B because at least half of the first layer atoms would be not bonded with oxygen. Among the rest, the structural model L is not compatible with our experimental findings because in this structure only two shifted components Ru_2 and Ru_1-O should

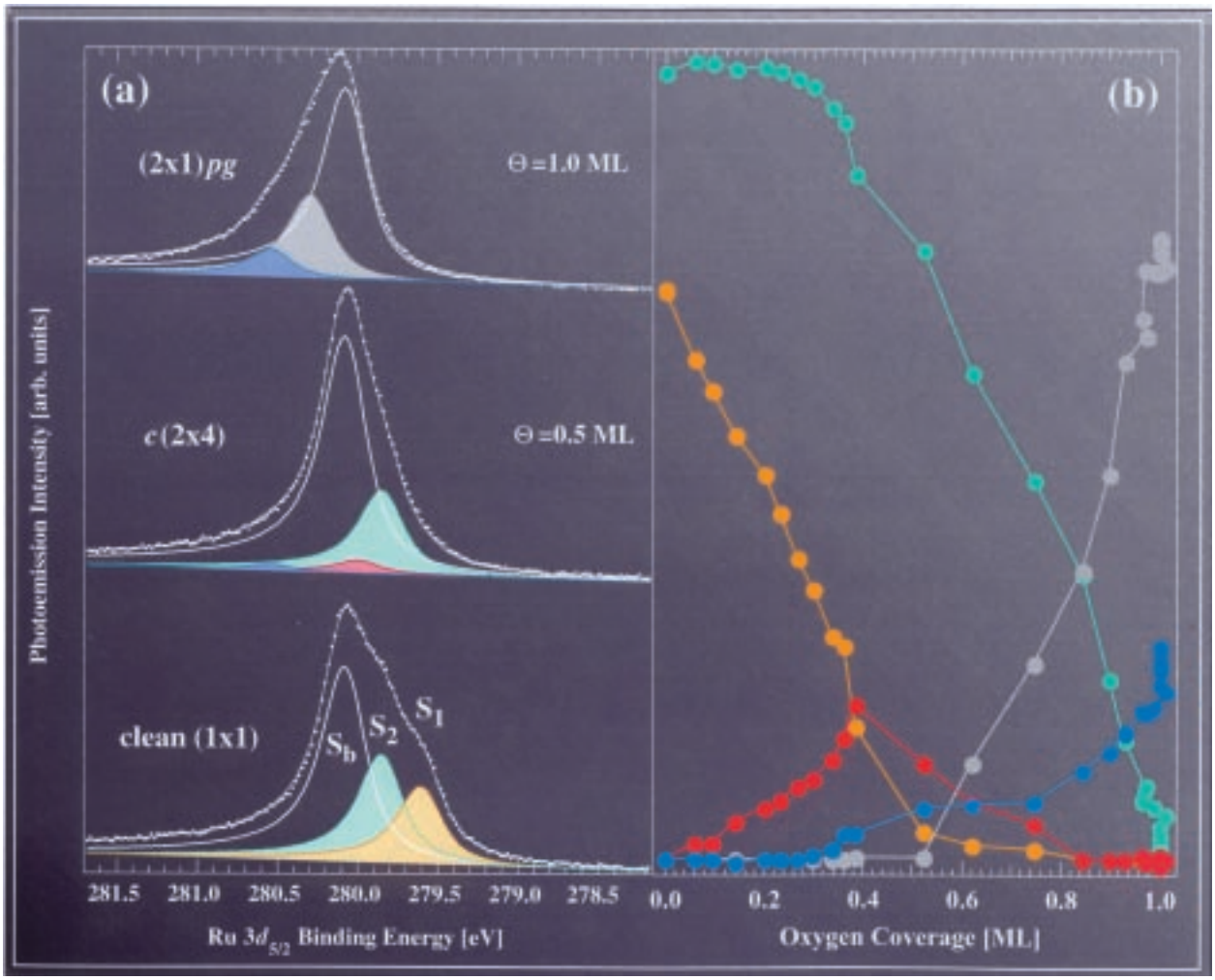

Figure 2. (a) Ru $3d_{5/2}$ core levels spectra from Ru(10$\bar{1}$0) recorded at 300K during oxygen uptake: (bottom) clean (1x1); (center) *c*(2x4); (top) (2x1)*pg*. Fit of the surface component are presented. (b) Results of fit. Colored curves are: (yellow) first layer Ru, (green) second layer Ru, (red) first layer single oxygen bonded Ru, (blue) second layer two oxygen bonded Ru and (grey) first layer two oxygen bonded Ru.

be present instead of the three observed at 0.5 ML.

We conclude that oxygen is therefore sitting in the three-fold hcp site (structure A or C) in agreement with recent LEED-IV and theoretical calculations [3]. From our results we cannot distinguish between structure A and C: they present the same number of second layer bonded and unbonded Ru atoms, but with different geometrical arrangement.

Interestingly, these two structures present the lowest Pendry R factor in the structural investigation [3].

The comparison of the behaviour of the oxygen related shifted components as a function of coverage allows to assign the Surface Core Level peaks to the corresponding Ru atoms. With reference to the models A and C of Figure 1, during oxygen uptake one expects the Ru_2-O and Ru_1-O related XPS components to appear and grow up to the completion of the *c*(2x4) structure at 0.5 ML. At higher coverage the population of Ru_1-O atoms decreases, Ru_2-O's keep on increasing and a Ru_1-2O atoms appear and reach the maximum at saturation. Finally, in the (2x1)*p*2*mg* structure only Ru_2-O and Ru_1-2O atoms are present. By comparing the expected behaviour with the experimental findings we assign the peak shifted by 465 meV (blue curve), –85 meV (red curve) and 215 meV (gray curve) to single oxygen bonded Ru second layer atoms (Ru_2-O), single oxygen bonded Ru atoms (Ru_1-O) and double bonded first-layer Ru atoms (Ru_1-2O), respectively.

In summary our results show that the knowledge of the oxygen adsorption site on Ru(100) can be directly obtained by high-resolution core level photoemission measurements of the Ru $3d_{5/2}$ SCLS induced by oxygen adsorption. The development of new surface core level shifted components at different coverage, ascribed to the first- and second-layer Ru atoms bonded with one or two oxygen atoms, permits an unambiguous assignment of the adsorption site as three-fold hcp in agreement with a previous structural determination. Moreover our results extend the usefulness and the applicability of the SLCS and provides information on the electronic structure modifications of first- and second-layer atoms upon adsorption.

References:

[1] D.M. Riffe, G.K. Wertheim, P.H. Citrin, Phys. Rev. Lett. 65, 219 (1990); J.N. Andersen, M. Qvarford, R. Nyholm, S.L. Sorensen, C. Wigren, Phys. Rev. Lett. 67, 2822 (1991).
[2] S. Poulsten, M. Tikov and R. Lambert, *Surf. Rev. Lett.* 1, 665 (1994).
[3] S. Schwegmann, A.P. Seitsonen, V. De Renzi, H. Dierisch, H. Bludau, M. Gierer, H. Over, K. Jacobi, M. Scheffler and G. Ertl, *Phys. Rev. B* 57, 15487 (1998).
[4] A. Baraldi, S. Lizzit, G. Comelli, A. Goldoni, Ph. Hoffmann and G. Paolucci, *Phys. Rev. B* 61, 4534 (2000)

Electron accumulation layer on a clean In-terminated InAs(001)(4x2)/c(8x2) surface

P. De Padova, C. Quaresima, P. Perfetti,
CNR-ISM; via Fosso del Cavaliere, 100, 00133 Roma, Italy

R. Brochier, C.Richter, V. Ilakovac, P. Bencok,
LMPS, Université de Cergy-Pontoise, Neuville/Oise, 95031 Cergy-Pontoise, France

C. Teodorescu,
LURE, Bat. 209 D, 91 898 Orsay, France

V.Y. Aristov,
Russian Academy of Sciences. Tchernogolovka, Moscow, Russia

R. L. Johnson,
Institut für Experimentalphysik, Universität Hamburg, D-22671 Hamburg, Germany

K. Hricovini,
LMPS, Université de Cergy-Pontoise, Neuville/Oise, 95031 Cergy-Pontoise, France
LURE, Bat. 209 D, 91 898 Orsay, France

One of the most recent frontiers in the field of magnetism is to build magnetic III-V semiconductors by incorporating a diluted amount of magnetic ions into the substrate [1].

These new materials offer the possibility of exploiting traditional techniques for controlling the carrier population in a semiconductor, in order to realise a novel class of tunable ferromagnetic devices for reading and writing of non-volatile data.

Magnetoelectronic devices, where the spin of the electron is controlled, are expected to find applications based on hybrid semiconductor structures. A spin-polarised field effect transistor (spin FET) derived by the injection of spin-polarised electrons from a ferromagnetic source into the GaAs semiconductor has already been proposed [2,3].

Ferromagnetism is rarely observed in semiconductors as a consequence of both low carrier density and prevalence of antiferromagnetic superexchange among local moments. As a result, most ferromagnetic semiconductors are relatively exotic systems with low Curie temperatures. Only recently the Curie temperatures over 100 K have been achieved in $(Ga_{1-x}Mn_x)As$ [3,4], and $(In_{1-x}Mn_x)As$ [5] at moderate Mn concentrations (x~0.05).

The most extensively studied systems up to date are (Fe,Mn)/GaAs. However, (In,Mn)As diluted magnetic III-V compound semiconductor is one of the most interesting systems and promising materials for technological interest in microelectronics due to the small direct band gap (0.36 eV at 300 K), and to its higher low-field mobility than GaAs and InP. This makes InAs an excellent candidate for high-speed field effect transistors.

In the case of InAs, the electronic structure of diluted (In,Mn)As magnetic semiconductors, has recently been calculated by Akai et al. [6] by using the Korringa-Kohn-Rostoker coherent-potential and local density approximation. The calculations show that the ground state of $(In_{0.94}Mn_{0.06})As$ is ferromagnetically stabilised by double exchange with a local Mn magnetic moment of about 4μB. The ferromagnetic state of (MnIn)As is half metallic, namely, the Fermi surface exists only in the majority spin band. The conductivity in such materials is expected to be governed by 100% of spin-polarised charge carriers.

Magnetic properties of (In,Mn)As are strongly sensitive to the corresponding crystallography, the strain, the interaction with InAs substrate and to the temperature. Therefore, by controlling the InAs surface reconstruction and the evolution of the metal/semiconductor interface it is possible to tailor their magnetic behaviour.

The high density of electrons present on semiconductor surface, which can form an electron accumulation layer, is of crucial technological importance for the InAs(001) surface because it permits the realisation of non-alloyed Ohmic contacts [7], and Josephson devices [8].

The (001) face of InAs gives different surface structures and stoichiometries depending on the procedure of preparation. Although the atomic structures of all the reconstructions of (001) surface are not yet completely understood, the c(8x2), c(2x8), and c(4x4) reconstructions present on the (001) crystal face are commonly believed to be superstructures of a 4x2 unit cell (see Fig.1) [9,10,11].

The interpretation of the clean InAs(001) In-terminated is still an open question. At least three problems are to be resolved: (i) the determination of a univocal crystallographic model for the clean reconstructed surface, (ii) the identification and attribution of the As3d and In4d surface core level

shifts (SCLSs), and (iii) the clarification of the origin of the presence of an intrinsic charge accumulation layer.

We have studied the InAs(001)-(4x2)/c(8x2) In-rich surface by high resolution core levels and valence band (VB) photoemission spectroscopies, LEED, RHEED and STM analysis. The experiments were performed using the synchrotron radiation on the VUV beamline. Undoped InAs(001) (3.5 Ω·cm) single crystal were used for all the measurements. The In-terminated InAs(001) clean surfaces were obtained after several cycles of argon sputtering and annealing at 800 K. In4d, As3d and VB photoemission spectra were measured after cooling the sample to ~150 K, using both angle integrated (acceptance 8°) and angle-resolved hemispherical (acceptance 2°) electron energy analysers. The angle between the photon beam and the normal to sample surface was 45°. The photon energy was 84.2 eV, and the total energy resolution better than 50 meV. STM measurements were performed at the Institut für Experimentalphysik, Universität Hamburg.

Figure 1(a) reports the LEED pattern of clean In-rich InAs(001)c(8x2) surface. In agreement with Ref.[10], this surface presents the fourth-order spots in the [0-11] direction, and the streaking of the twofold spots along the [011] direction. These characteristics are the fingerprint of the (4x2) and c(8x2) reconstructions.

Figure 1(b) shows the empty-state (U=+0.7 V and I=0.5 nA) STM image over a 200Åx200Å area. The (4x2) units cell and the c(8x2) superstructure are clearly visible and marked on the figure together with the symmetry axis. Figure 1(c) shows the filled-state (U=-1.2 V, I=0.6 nA) STM image collected at higher resolution over an area of 100Å x100Å. Very uniform and bright rows are detected along the [011] direction. The roughness along the rows and between the rows is not larger than 0.5 Å. Consequently, we can rule out the one-dimer model proposed in [10,11]. Furthermore, the distance between two protuberances measured along [011] direction on the rows is 3.29 Å. This value is exactly equal to the In-In bond (3.3 Å) in the metallic In structure [12].

On the basis of these results we suggest that the rows present on the clean InAs surface be formed by In atoms having metallic character.

In photoemission we observe dramatic changes in the shape of the In4d and As3d core levels passing from ϑ=42.5° to ϑ=45° (see Fig.2) that are probably due to photoelectron diffraction effect. In order to get a better insight about surface contributions for both, In4d and As3d core levels, we subtract the spectra collected at ϑ=42.5° and ϑ=45°. This procedure allows us to determine precisely the position of components in the spectra. The subtraction gives binding energies of surface components, referred to the bulk component (B), of +0.31 eV (S1), -0.25 eV (C) for the In4d, and one peak at –0.24 eV for the As3d which were used in the fit of the respective core levels (see Fig. 2). In4d spectral decomposition was obtained by least-square fitting the spectra with Voigt and Doniach-Sunjic functions, whereas As3d core level only with Voigt functions. Accordingly to Refs. [13,14], Lorentzian width (FWHM) W_L =130 (100) meV, spin orbit splitting S.O.=0.87 (0.69) meV, and branching ratio R=1.57 (1.58) fitting parameters were used for In4d and As3d, respectively. The Gaussian widths W for both bulk and surface was fixed to 300 meV. In4d best fit was obtained introducing for the C component an asymmetry parameter α=0.045.

It is worth noting that the C component is located at the energy of the metallic In4d. Therefore, it is reasonable to attribute this component as due to the contribution of well-localised metallic In rows evidenced in the STM images.

Figure 3 shows a significative emission at the FL on the InAs(001) surface that is probably derived from the self-assembled In metallic rows on the clean surface. The VBM maximum is located at 0.57 eV. Considering the band gap of the InAs (0.36 eV) our VB indicate a downward band bending of 0.21 eV in agreement with that obtained by HREELS

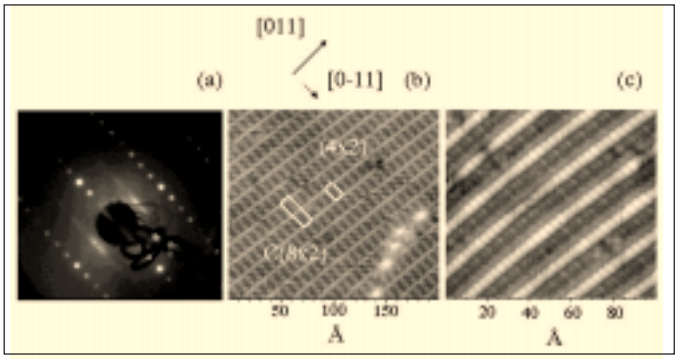

Figure1. LEED pattern of (4x2)–c(8x2) clean InAs(001) surface, (Ep= 50.4 eV) (a); 200Åx200Å empty–state STM image (U=+0.7 eV, 0.5nA) (b); 100Å x100Å filled-state STM image (U=-1.2 V, I=0.6 nA) (c). The (4x2) units cell, the superstructure c(8x2) and the symmetry axis are marked.

P. De Padova, C. Quaresima, P. Perfetti, R. Brochier, C.Richter, V. Ilakovac, P. Bencok, C. Teodorescu, V.Y. Aristov, R. L. Johnson, K. Hricovini

measurements [15]. The electron density corresponding to a band bending of 0.21 eV is about 10^{12} cm $^{-2}$. By calculating the area of the In rows on the InAs STM topographic surface we obtain an occupation of 25 %. Supposing, in an extreme case, that each In atom on the linear chain gives one electron, we obtain an electron density ($\approx 10^{13}$ cm $^{-2}$) close to the value calculated by the band bending.

In conclusion clean In-terminated InAs(001)c(8x2) surface was examined by LEED, STM and high-resolution core-level and valence band (VB) spectroscopies. Metallic In-rows are found by STM measurements on the well ordered (4x2)-c(8x2) InAs(001) surface. SCLSs of In4d and As3d core levels are resolved. The decomposition of In4d core level shows a new component (C) associated with the metallic In located on the rows. Photoelectron VB showed an electron emission at the Fermi level demonstrating that the InAs(001) In-terminated surface is metallic.

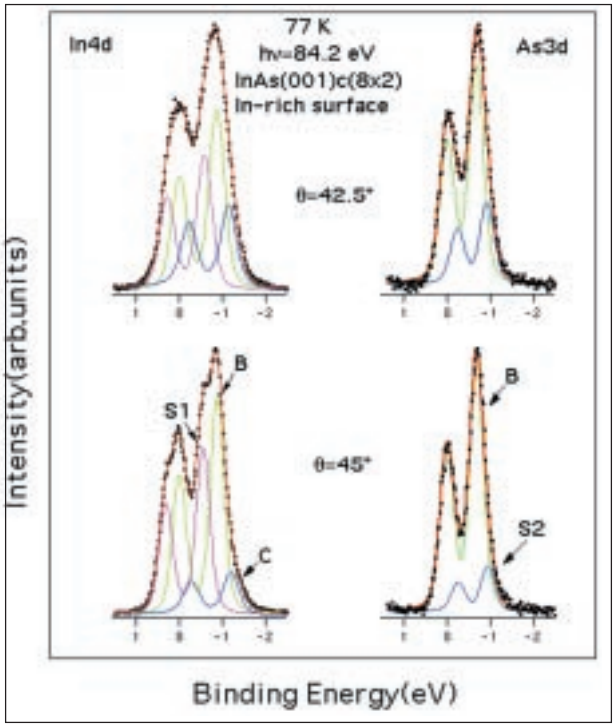

Figure 2. Best fits and spectral components (full lines) of the In4d(left side) and As3d(right side) spectra (dots) collected at ϑ=45° and ϑ=42.5°.

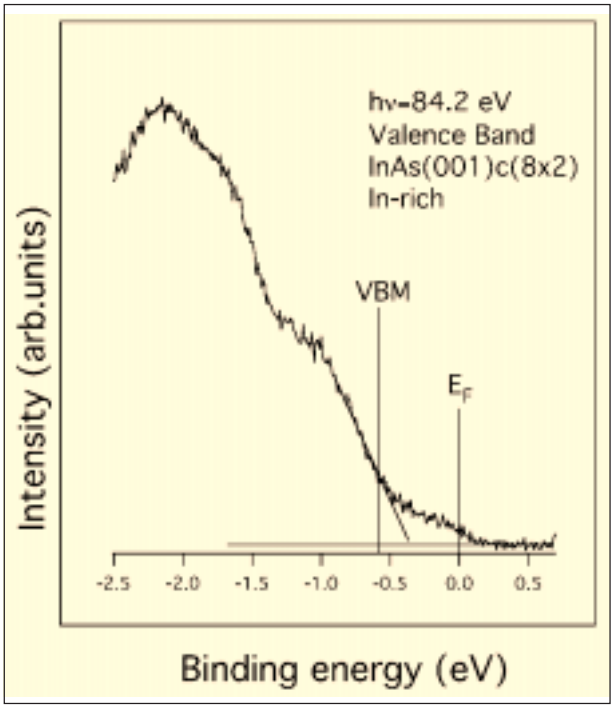

Figure 3. Photoelectron spectrum collected on the InAs(001) clean surface at the energy region between the upper part of VB and the bottom of the conduction band. The VBM and the Fermi level energy are indicated.

References:

[1] H. Ohno, Science, 281 (1998) 951
[2] S. Datta, B. Das, Appl.Phys.Lett. 56 (1990) 665.
[3] Y.Ohno, D. K. Young, B. Beschoten, F. Matsukura, H. Ohno & D. D. Awschalom, Nature 402 (1999) 790
[4] B. Beschoten et al. PRL. 83 (1999) 3073
[5] R. Brochier et al. To be published
[6] H. Akai, Phy.Rev.Lett. 81 (1998) 3002
[7] J. M. Woodall, j. L; Freeouf, G. D. Pettit, T. Jackson, and P. Kircher, J. Vac Sci. Technol, 19 (1981) 626
[8] H. Takayanagi and T. Kawakami, Phys. Rev. Lett. 54 (1985) 2449
[9] P. John, T. Miller, a,d T.-C. Chiang, Phys. Rev. B 39 (1989) 1730
[10] C. Kendrick, G. LeLay, A. Kahn, Phys. Rev. B 54 (1996) 17877
[11] S. Ohkouchi and N. Ikoma, Jpn. J. Appl. Phys. 33 (1994) 3710
[12] N. Ridley, J. Less, Common Metals, 8 (1965) 354
[13] J. N. Andersen and U. O. Karlsson, Phys. Rev B, 41 (1990) 3844
[14] P. R. Varekamp, M. C. Håkansson, J. Kanski, D. k. Shuh, M. Björkqvist, M . Gothelid, W. C. Simpson, U.O. Karlsson, J. A. Yarmoff, Phys. Rev. B, 54 (1996) 2101
[14] M. Noguchi, K. Hirakawa, and T. Ikoma, Phys. Rev. Lett. 66 (1991) 2243

Effects of the interatomic potential anharmonicity on the bulk and surface photoemission core-levels

Alessandro Baraldi, Silvano Lizzit, Giorgio Paolucci,
Sincrotrone Trieste, Italy

Giovanni Comelli, Renzo Rosei,
Dipartimento di Fisica, Università di Trieste, 34127 Trieste and Laboratorio T.A.S.C.-I.N.F.M., S.S. 14 Km.163.5, 34012 Basovizza, Trieste, Italy

By means of high energy resolution photoemission we show that the Rh(100) $3d_{5/2}$ Surface Core Level Shift (SCLS) decreases when the surface temperature increases. The effect is interpreted as due to the expansion of the first interlayer distance, because of the different anharmonicity of the bulk and surface inter-atomic potentials, in agreement with theoretical predictions

The core level binding energy difference between an atom at the surface and in the bulk, usually named Surface Core Level Shift (SCLS), has been widely investigated in recent years. It is strictly related to the differences in the electronic and geometrical structure of the atoms in the first and in deeper layers of a solid. The availability of synchrotron radiation has prompted a large number of experimental studies on 4d transition metals[1-7], while a complementary effort has been devoted by theoreticians in the attempt of reproducing the experimental results and interpreting the nature of this phenomenon[8-12]

It is commonly accepted nowadays that *ab initio* theoretical calculations can reproduce the SCLS with high accuracy, provided the contribution of the bulk and surface core hole screening in the final-state of the photoemission process is taken into account. Furthermore it is clear that even small variations of the structural parameters considered in the calculations can affect the results. As an example, the theoretical work of Andersen et al.[11] predicts that the transition metal 3d SCLS decreases as the first inter-layer distance increases. Due to the extreme difficulties of measuring SCLS variations for these core levels, which are very small, an experimental confirmation of this effect has never been provided so far and constitutes the subject of the present work.

High-energy resolution photoemission measurements have been performed at the SuperESCA beamline of ELETTRA. The $3d_{5/2}$ Rh(100) core level spectra were measured using a photon energy of 398 eV with an overall energy resolution of 65 meV. A sequence of spectra of the $3d_{5/2}$ Rh(100) region was measured as a function of the sample temperature, according to the following procedure. The sample was brought to the selected temperature, then a photoemission spectrum was acquired in about 90 s and finally the sample was flashed to 620 K. This procedure prevents contamination of the surface from the residual chamber atmosphere, which would reduce the SCLS, as previously shown[3-5,7].

A series of $Rh3d_{5/2}$ core level photoemission spectra acquired at different temperatures is shown in Fig 1. As previously reported[4] the higher binding energy (BE) peak arises from the atoms in the bulk while the lower BE peak originates from the first atomic layer. Spectrum decomposition into bulk and surface components has been performed by fitting the data using two peaks with Doniach-Sunjic (DS) lineshape[14]. The latter is described by two parameters, the Anderson singularity index α due to the final-state screening of the core hole and the Lorentzian width Γ linked to the core-hole lifetime. The two DS peaks, which were allowed to have different α and Γ, were convoluted with Gaussians in order to account for the experimental, phonon and any possible inhomogeneous broadening. A linear background was also added to the fit. The individual peaks are also shown in Figure 1. At the lowest temperature we find a SCLS of 0.655±0.005 eV, which is in good agreement with previous experimental results[3-5,7]. In our case however, the Gaussian widths are much lower, as a combined consequence of the higher resolution and lower temperature of our experiment. The values of the α and Γ parameters obtained from the low temperature spectrum have been fixed in order to fit the data at the higher temperature. Apart from the BEs of the two peaks, only the gaussian widths have been used as free parameters in a least-square analysis, accounting for the expected increase in phonon broadening. Two effects can be distinguished. First, both the bulk and surface components shift to lower binding energies as the temperature increases. The bulk peak BE changes by ~55 meV between 20 K and 970 K, while the surface-peak shift by ~ 25 meV. As a consequence the temperature dependent SCLS, which is plotted in Figure 2 (upper panel), decreases by ~30 meV between 20 and 970 K. Secondly, both the surface and bulk components increase their width as the tem-

perature rises. The width includes two different contributions, namely the experimental resolution and the phonon broadening. The latter is shown for our data in Fig. 2 (lower panel), where the square of the gaussian width for the surface and bulk peaks is plotted against the sample temperature after subtraction of the experimental resolution. At 20 K the total gaussian width is about the same for the two components, but for higher temperatures the surface peak width grows more rapidly than the bulk one.

The observed temperature dependence of the SCLS can be understood by taking into consideration the different anharmonicity of the surface and bulk interatomic potentials. Because of the lower symmetry, the anharmonicity at the surface is expected to be larger than in the bulk, and therefore the first interlayer spacing increases with the temperature more than in the bulk. Indeed in a recent theoretical study Xie and Scheffler[15] predict for the Rh(100) surface that the surface relaxation $\Delta d_{12}/d_0$ goes from -2.5% at 0 K to -0.5% at 600 K, with a surface thermal expansion coefficient that at 300 K is 5 times larger than in the bulk. At 770 K, where on the basis of the above mentioned theoretical results the surface relaxation is expected to be approximately 0%, we measured a SCLS of 0.62 eV. This value is in extremely good agreement with the result of first-principles calculations by Andersen et al.[11], who predict a SCLS of 0.62 eV for $\Delta d_{12}/d_0$=0%. Moreover, they calculated also that larger SCLS, as we measure at lower temperatures, corresponds to contracted first interlayer distances. Our data therefore clearly support the theoretical predictions that there is an inward relaxation of the Rh(100) surface at room temperature, in contrast to the most recent LEED IV study which suggests an outward relaxation ($\Delta d_{12}/d_0$ =+ 1.0±0.6%) [16]

Further information about the bulk and surface interatomic potentials could in principle be obtained by analyzing the observed gaussian broadening of the photoemission peaks. The higher slope of the square of the surface gaussian broadening with respect to the bulk one is an evidence of the existence of enhanced vibrations at the surface[17]. The

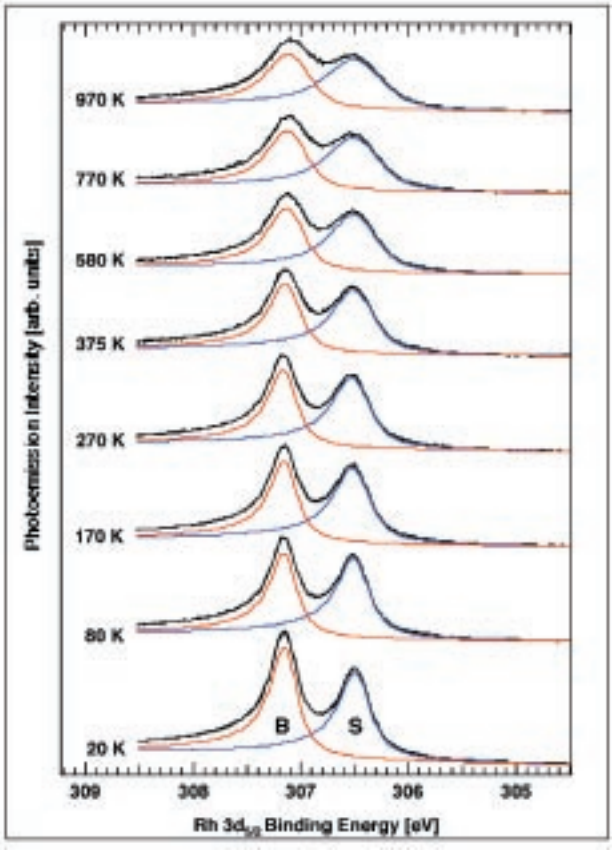

Figure 1: Photoemission spectra and corresponding fits of Rh(100) $3d_{5/2}$ core-level measured at temperatures ranging from 20 K to 970 K (photon energy of 398 eV).

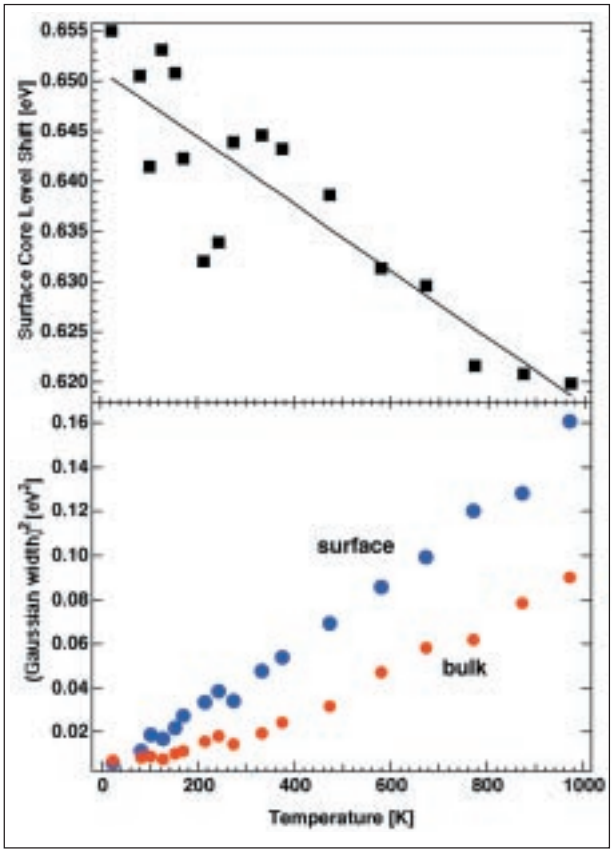

Figure 2: Upper panel: Temperature evolution of the Rh(100) $3d_{5/2}$ Surface Core Level Shift Lower panel: temperature evolution of the square of the intrinsic gaussian width of the Rh(100) $3d_{5/2}$ core level, after quadratic subtraction of the intrumental resolution.

presence of anharmonicity in the interatomic potentials though cannot be revealed directly in a simple way from the gaussian width data. Deviation from the temperature dependent linear behavior predicted by a theory based on the Debye model has previously been taken as an evidence of the presence of anharmonicity in the potential energy surface (PES)[18]. This conclusion however has to be considered with care, as the cited theory assumes also that the shape of the inter-atomic potential for the final state ionized atoms and the initial state neutral ones is the same, and only the equilibrium distances change[19]. Using a different approach Theis and Horn[20] have shown that a deviation from the linear behavior does not necessarily require the existence of anharmonicity in the initial state PES, but can also be due to the presence of a quadratic coupling term in the Hamiltonian, i.e. a change in the force constant between the initial and final state PES. Further theoretical investigations, where the actual shape of the PES for both the initial and final state is considered, are needed in order to clarify this point. The results of the present work also show that, in general, care must be taken when comparing experimental SCLS with theoretical predictions if low temperature experimental data is not available.

Finally it is worth considering the role of the magnetic ordering which was recently experimentally demonstrated on this surface[21] in the change of SCLS. Calculations show[22] that the magnetic and non magnetic states of this surface are degenerate, while the electronic structure is strongly influenced by changes in the interplanar and intraplanar atomic distances. For this reason we believe that an interpretation of the present data which neglects magnetic effects is appropriate.

In conclusion, on the basis of high resolution photoemission data we have analyzed the temperature behavior of the bulk and surface components of the Rh(100) $3d_{5/2}$ core level, evidencing a decrease of the SCLS on increasing the temperature. The effect can be interpreted in terms of a higher anharmonicity of the inter-atomic potential of the surface atoms, in agreement with theoretical predictions.

ACKNOWLEDGEMENTS

We would like to thank S. de Gironcoli, S. Baroni, N. Mårtensson and K.C. Prince for stimulating discussions. Technical support of M. Barnaba is gratefully acknowledged.

References:

[1] R. Nyholm, M. Qvarford, J.N. Andersen, S.L. Sorensen, and C. Wigren, J. Phys.: Condens. Matter 4, 277 (1992).
[2] E. Lundgren, U. Johansson, R. Nyholm, and J.N. Andersen, Phys. Rev. B 48, 5525 (1993).
[3] A. Borg, C. Berg, S. Raaen, and H.J. Venvik, J. Phys.: Condens. Matter 6, L7 (1994).
[4] M. Zacchigna, C. Astaldi, K.C. Prince, M. Sastry, C. Comicioli, R. Rosei, C. Quaresima, C. Ottaviani, C. Crotti, A. Antonini, M. Matteucci, and P. Perfetti, Surf. Sci. 347,53(1996).
[5] M. Zacchigna, C. Astaldi, K.C. Prince, M. Sastry, C. Comicioli, M. Evans, and R. Rosei, Phys. Rev. B 54, 7713 (1996).
[6] A. Beutler, E. Lundgren, R. Nyholm, J.N. Andersen, B. Setlik, and D. Heskett, Surf. Sci. 371, 382 (1997); 396, 117 (1998).
[7] F. Strisland, A. Ramstad, T. Ramsvik, and A. Borg, Surf. Sci. 415, L1020 (1998).
[8] M. Alden, L.H. Skriver, and B. Johansson, Phys. Rev. Lett. 71, 2449 (1993).
[9] M. Methfessel, D. Henning, and M. Scheffler, Surf. Sci. 287'288, 785 (1993).
[10] M. Methfessel, D. Henning, and M. Scheffler, Surf. Rev. Lett. 2, 197 (1995).
[11] J.N. Andersen, D. Henning, E. Lundgren, M. Methfessel, R. Nyholm, and M. Scheffler, Phys. Rev. B 50,17 525(1994).
[12] M.V. Ganduglia-Pirovano, V. Natoli, M.H. Cohen, J. Kudrnovsky, and I. Turek, Phys. Rev. B 54, 8892 (1996)
[13] A. Baraldi, V.R. Dhanak, G. Comelli, K.C. Prince, and R. Rosei, Phys. Rev. B 56,10 511(1997).
[14] S. Doniach and M. Sunjic, J. Phys. C 3, 185 (1970).
[15] Xie and M. Scheffler, Phys. Rev. B 57, 4768 (1998).
[16] G. Teeter, D. Hinson, J.L. Erskine, C.B. Duke, and A. Paton, Phys. Rev. B 57, 4073 (1998).
[17] D.M. Riffe, G.K. Wertheim, and P.H. Citrin, Phys. Rev. Lett. 67, 116 (1991).
[18] G.K. Wertheim, D.M. Riffe, and P.H. Citrin, Phys. Rev. B 49, 2277 (1994).
[19] L. Hedin and A. Rosengren, J. Phys. F: Met. Phys. 7, 1339 (1977).
[20] W. Theis and K. Horn, Phys. Rev. B 47,16 060(1993).
[21] Goldoni, A. Baraldi, G. Comelli, S. Lizzit, and G. Paolucci, Phys. Rev. Lett. 82, 3156 (1999).
[22] J.-H. Cho and M. Scheffler, Phys. Rev. Lett. 78, 1299 (1997).

Alessandro Baraldi, Giovanni Comelli, Silvano Lizzit, Renzo Rosei, Giorgio Paolucci

A supersonic molecular beam for gas-surface interaction studies with synchrotron radiation

A. Baraldi, M. Barnaba, L. Rumiz, S. Lizzit, G. Paolucci,
Sincrotrone Trieste, Italy

M. Moretuzzo, G. Comelli, R. Rosei,
Dipartimento di Fisica, Università di Trieste, via Valerio 2, I-34127 Trieste and Laboratorio T.A.S.C.-I.N.F.M., Strada Statale 14, km 163.5, I-34012 Basovizza (Trieste), Italy

F. Buatier de Mongeot, U. Valbusa,
INFM Unità di Genova and Dipartimento di Fisica, Via Dodecaneso 33, I-16146 Genova, Italy

Gas-surface interaction is crucial in a wide variety of phenomena spanning from reactive etching of semiconductors to chemisorption and catalysis.

A typical approach to study these phenomena is to use the experimental technique called "Molecular Beam Reactive Scattering" (MBRS), which makes use of the highly collimated, highly intense and energy controlled molecular beams produced during the supersonic expansion from a nozzle source. However until now the MBRS has been applied to study the gas-surface interaction by detecting the scattered molecules in gas phase with a mass spectrometer or by detecting by spectroscopic techniques the adsorbates stabilized on the surface after the exposure to the beam.

In spite of the undoubted success of this technique we believe that an important improvement will be the coupling of our new supersonic molecular beam (see Figure), which permits to control all the kinetic parameters (angles of incidence, flux, translational and vibrational energy, etc.), to a quantitative surface technique with good time resolution like the "*Fast X-Ray Photoelectron Spectroscopy*" realized at the SuperESCA. The high photon flux and high-energy resolution at the SuperESCA beamline of ELETTRA will allow following in real-time phenomena like chemisorption, dissociation, desorption and reactions of molecular species with a time resolution in the ms range.

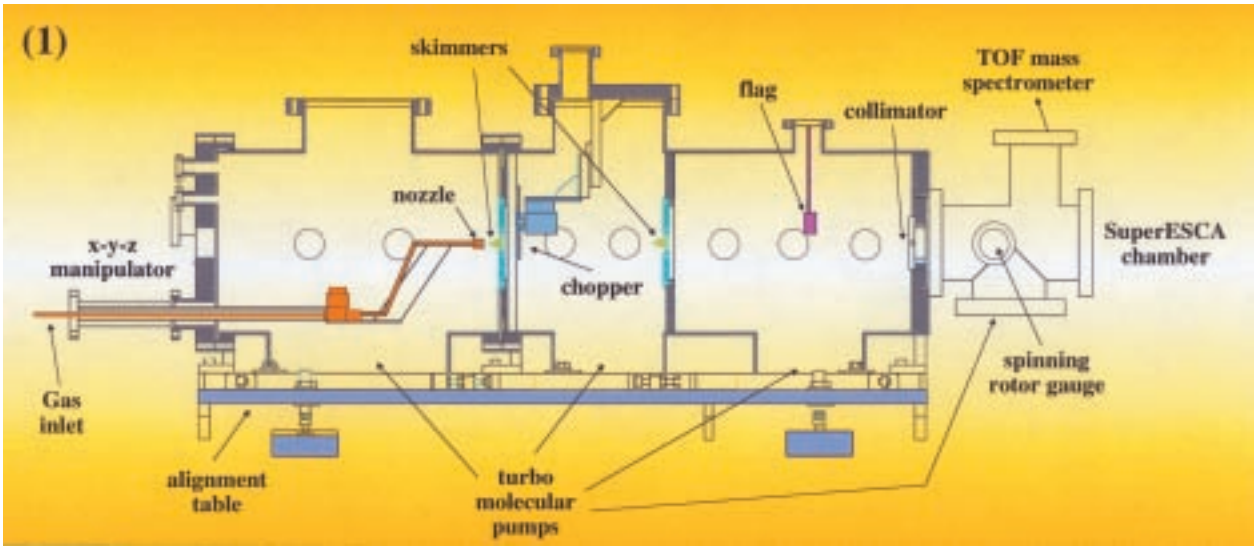

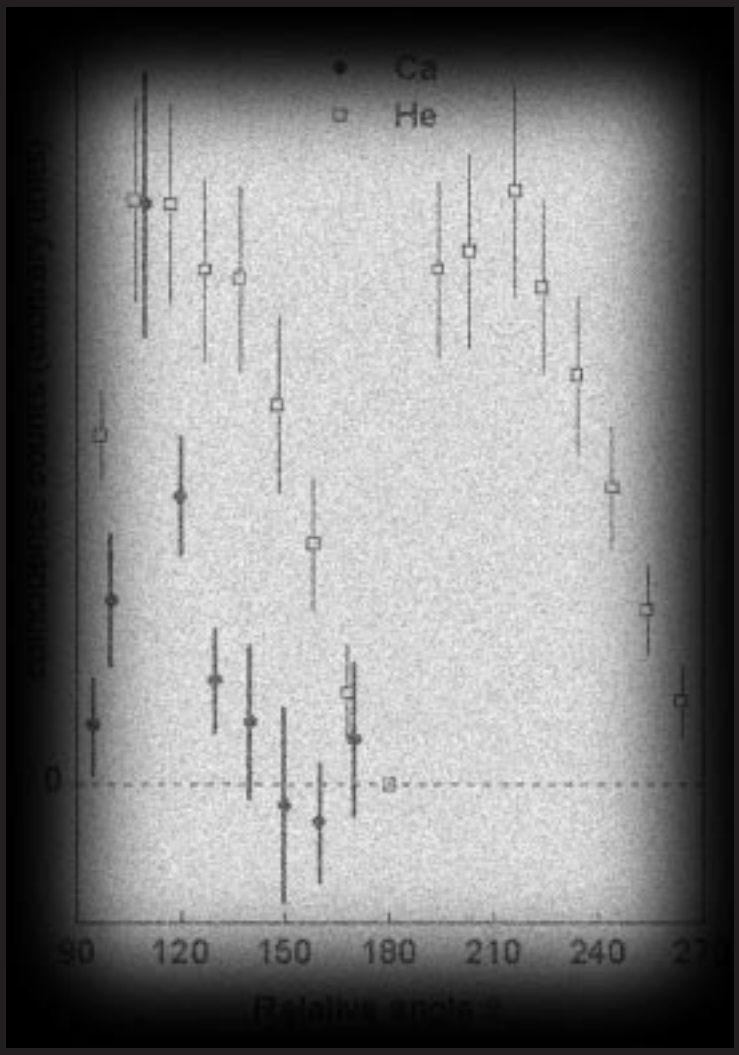

Atomic Physics

Measurements of resonance free double photoionization (γ,2e) in atomic calcium

K. J. Ross, A. De Fanis,
Department of Physics and Astronomy, Southampton University, Southampton SO17 1BJ, UK

H.-J. Beyer,
Atomic Physics Unit, University of Stirling, Stirling FK9 4LA, UK

J. B. West,
CLRC Daresbury Laboratory, Warrington WA4 4AD, UK

INTRODUCTION

Studies of double photoionization have focused mainly on the He atom, where there is good general agreement between relative values of the theoretical and experimental triple differential cross section (TDCS) [1]. We have extended such studies to the alkaline earth atoms, which have a similar outer electron shell to He and at first might be expected to behave similarly. We have discovered however that this is far from the case, probably because of the differing interaction between the two outgoing electrons, as well as between those electrons and the ionic core.

In our investigations so far [2,3] we have studied double photoionization in Ca atoms for photon energies in the region of the Ca 3p→3d *giant* resonance at 31.41 eV using the Daresbury Synchrotron Radiation Source (SRS). The presence of this giant resonance greatly enhances the cross section of the double photoionization process, and for this reason it proved possible to make double photoionization measurements using the second generation Daresbury SRS.

Our earlier experiments on Ca used two different geometries, in both cases the electrons being observed in the plane perpendicular to the photon beam. In that of reference [2] one electron was observed in a fixed direction at 90^0 to the **E** vector, and the other over a range of ~180^0 opposite to it, for relative angles θ_{12} between the two electrons in the range 90^0 to 270^0. In the later experiment [3] one electron was observed parallel to the **E** vector, the relative angles of emission could be varied between 90^0 and 270^0 between the two electrons as before. In both experiments four maxima were observed in the angular correlation data over the 180^0 range of the relative angles between the electrons, and the structure of the maxima was assumed to be symmetrical about $\theta_{12}=180^0$; the TDCS at $\theta_{12}=180^0$ is zero. This was in striking contrast to the case for He for which only two maxima are found experimentally.

The first theoretical analysis of the resonant Ca data was carried out by Maulbetsch *et al* [4] for the case where the two photoejected electrons have equal energy. They reproduced the shape of the Ca angular correlation data in a parameterisation based on selection rules, interference effects and electron correlations. The selection rules corresponding to $^1P^0$ symmetry, which is assumed to be the case for the Ca resonance at 31.41 eV, require that the TDCS is zero when the electrons are ejected in opposite directions or both are ejected perpendicular to the E-vector, as was found in [2]. The second minimum seen at a relative angle of 144^0 in the experiment was attributed to destructive interference in the outgoing partial waves of the ejected electrons, primarily between the *pd* and *df* channels [4]. Using these concepts it was possible to obtain a good fit to the experimental data, including that of the later experiment [3]; also in this case a zero in the TDCS was expected, and in fact observed, when the electron analysers were set to a relative angle of 180^0. As mentioned above, four maxima were observed but now the inner pair of maxima (those closer to the symmetry axis at $\theta_{12}= 180^0$) were much smaller than the outer pair; in the earlier experiment the maxima were of approximately equal magnitude. It was possible to reproduce the features and relative intensities seen in both sets of experimental data, and the data from the two experiments were consistent with each other [4].

Given the complications of modelling the on-resonance measurements, we attempted to observe resonance-free double photoionization at the second generation Daresbury SRS, but the coincidence count rates were so low that they could not be distinguished from background noise. In this highlight we describe the results which we obtained for Ca in a resonance-free region by using our spectrometer on the third generation SRS ELETTRA [5].

EXPERIMENT

The experiment was conducted at the Gas Phase Beamline at ELETTRA [6]. The spectrometer

contains two 150^0 hemispherical sector electron energy analyzers of 90 mm mean radius, detecting electrons ejected in the plane perpendicular to the photon beam. One analyzer is in a fixed position, the other can be rotated through ~180^0 around the photon beam; the relative angles between them can be varied over the range 90^0 to 270^0. An effusive beam of metal vapor is produced and focused in the interaction region by a cylindrical oven that surrounds the radiation beam [7]. The full width half maximum of the electron analysers was set at ~200 meV and the monochromator band pass was set at 250 meV, similar to that used for our earlier measurements at the Daresbury SRS. Further details of the apparatus are given in reference [3].

The photon energy which we used was 43.03 eV, this being near the peak of the output of the beam line monochromator. It is also in a region of the Ca spectrum which is free of absorption profiles, and also where Auger lines do not occur with the same energies as any electrons resulting from double photoionization. Furthermore, the background count rates of our electron analysers are low at the corresponding electron kinetic energies, so that the chance coincidence rate is also kept low.

RESULTS AND DISCUSSION

The figure shows the measured TDCS over the range of relative angles θ_{12} from 93^0 to 170^0 for equal energy sharing of the two emitted electrons; the excess energy was 25.05 eV. Each data point was accumulated for an average of 12 hours. The error bars on the data contain only the statistical uncertainties of the true and false coincidences (1σ limits). Also plotted in the figure are the He TDCS data of Schwarzkopf and Schmidt [8], recorded under similar geometrical conditions at an excess energy of 20 eV.

There are two features evident from the figure. First, there is clearly no indication of two maxima in the ~90^0 range of our data from this experiment, in contrast to our previous Ca measurements made at the 3p→3d resonance at 31.41 eV. We note that our previous measurements were made at an excess energy of 13.43 eV, whereas those presented here were recorded at an excess energy of 25.05 eV. However, it seems unlikely that the difference in excess energy is responsible for the major difference in the number of maxima observed in our two sets of data. Second, the Ca TDCS structure in the figure is different to that of He, in that the maximum is much narrower than that for He. Even though the two atoms, Ca and He, have similar closed outer shells, it would appear that the two $4s^2$ electrons in Ca are more strongly correlated in the initial state than is the case for He, with a consequential effect on the TDCS. In this respect it is interesting to make a comparison of our data with the calculated reduced TDCS of Kazansky and Ostrovsky [9], for excess energies of the two electrons up to 15.5 eV, and also that of Malegat *et al* [10] for excess energies up to 10 eV. These authors predicted that two maxima should be present for $90^0<\theta_{12}<180^0$, although their TDCS was dominated by a single peak. However, no second maximum is visible, within the accuracy of our experiment, in the off-resonance measurements. The present data were taken for a total excess energy of 25.03 eV, and this may explain the detailed differences between theory and our experimental data. Kazansky and Ostrovsky attributed the presence of the small, second maximum to the detailed shape of the radial wave function for the initial state, and we note that the presence of two maxima becomes less evident as the excess energy increases. The two peaks approach each other and the intensity of the smaller peak at lower values of θ_{12} becomes almost negligible.

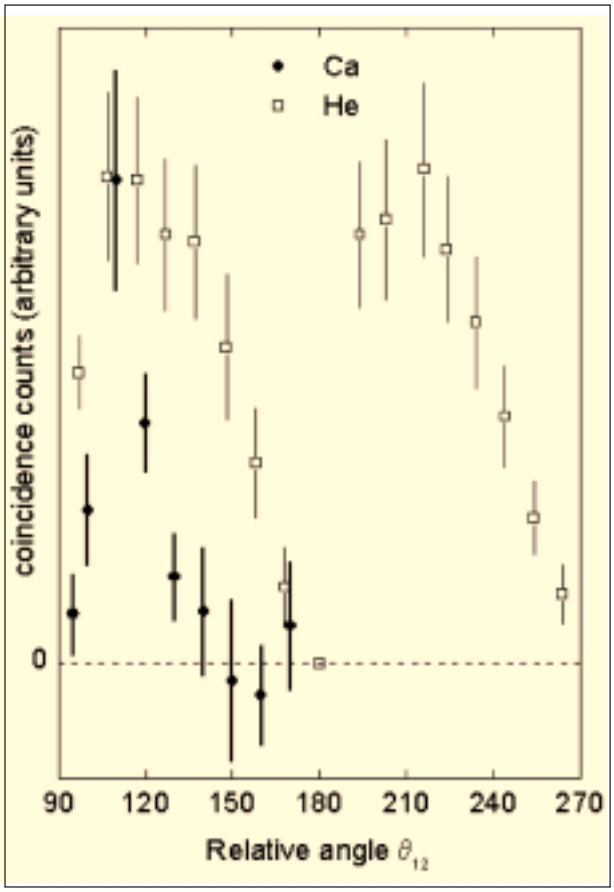

From the reduced TDCS calculated by Malegat *et al*. no conclusions can be drawn concerning the dependence of the TDCS on the

excess energy, since they present data at only three energies: 0.1, 1 and 10 eV. Although a second, smaller maximum becomes better resolved as the excess energy increases, its intensity appears to be lowest at the intermediate energy of their calculations. Furthermore, they point out that the weak secondary structure may be an artifact due to the potential they used in their calculations. The main peak in the reduced TDCS for Ca calculated by Malegat *et al.* is narrower than the reduced TDCS for He at the same excess energies; our experimental data are in agreement with this theoretical result.

An attempt was also made to estimate the ratio of the cross sections for double photoionization of Ca at the resonant and non-resonant energies. This was done by measuring the coincidence count rate at the peak of the 3p→3d resonance at 31.41 eV, and comparing this with the corresponding rate in the continuum at 43.03 eV. The result is of course susceptible to the resolution used for the resonance measurement, in our case ~250meV and therefore considerably larger than the natural width of the 3p→3d resonance. As a result the ratio we measure will be smaller than the true ratio which would be obtained if our resolution were sufficient to reproduce the actual peak profile. Also, the measurements were made for a relative angle between the directions of the two electrons of 100^0 and no correction was made for any angular effects. For these reasons the values obtained here give a measure of the cross section ratio for a realistic experimental situation, rather than an absolute value. The relative photon flux at the two energies was determined from the current measured by a photodiode at the rear of the experimental chamber. The average of two sets of data from these measurements gave a ratio of (3800±2100):1 for the two cross sections at 31.41 and 43.03, after correction for the energy dependence of higher order contributions from the beamline. This is to be compared with similar measurements for the single photoionization cross section, made by observing the intensities of the 4s electrons, which gave a value of (6200±400):1, the error being substantially smaller because of the much larger count rates involved. Our measurements indicate therefore that the double photoionization probability is significantly enhanced by the resonance, although, given the uncertainty in the ratio of the on:off-resonance double photoionization cross sections, this conclusion has to be tentative.

More significantly, an indication of the magnitude of the cross sections involved in making TDCS measurements for metal atoms has been obtained. It is clear that even with a third generation synchrotron radiation source such measurements are still difficult. The main limitation, in view of the extended measuring time required for a complete set of angles, was the long term stability of our experiment. This could be overcome by using a multiple angle detector system.

ACKNOWLEDGMENTS

This work was supported by a grant from the EPSRC. We are grateful to L. Avaldi, M. Alagia, R. Richter and S. Stranges for their expert assistance in making this experiment successful.

References:

[1] J. S. Briggs and V. Schmidt; *Journal of Physics B: Atomic, Molecular and Optical Physics*; **33** R1 (2000)
[2] K. J. Ross, J. B. West and H-J Beyer; *Journal of Physics B: Atomic, Molecular and Optical Physics*; **30** L735 (1997)
[3] K. J. Ross, J. B. West, H-J Beyer and A. De Fanis; *Journal of Physics B: Atomic, Molecular and Optical Physics*; **32** 292 (1999)
[4] F. Maulbetsch, I. L. Cooper and A. S. Dickinson; *Journal of Physics B: Atomic, Molecular and Optical Physics*; **33** L119 (2000)
[5] H-J Beyer, J. B. West, K. J. Ross and A. De Fanis; *Journal of Physics B: Atomic, Molecular and Optical Physics* (accepted)
[6] R. R. Blyth *et al*; *Journal of Electron Spectroscopy and Related Phenomena*; **101-103** 959, (1999)
[7] K. J. Ross and J. B. West; *Measurements of Science and Technology*, **9** 1236 (1998)
[8] O. Schwarxkopf and V. Schmidt; *Journal of Physics B: Atomic, Molecular and Optical Physics*; **28** 2847 (1995)
[9] A. K. Kazansky and V. N. Ostrovsky; *Journal of Physics B: Atomic, Molecular and Optical Physics*; **30** L835 (1997)
[10] L. Malegat, F. Citrini, P. Selles and P. Archirel; *Journal of Physics B: Atomic, Molecular and Optical Physics*; **33** 24 (2000)

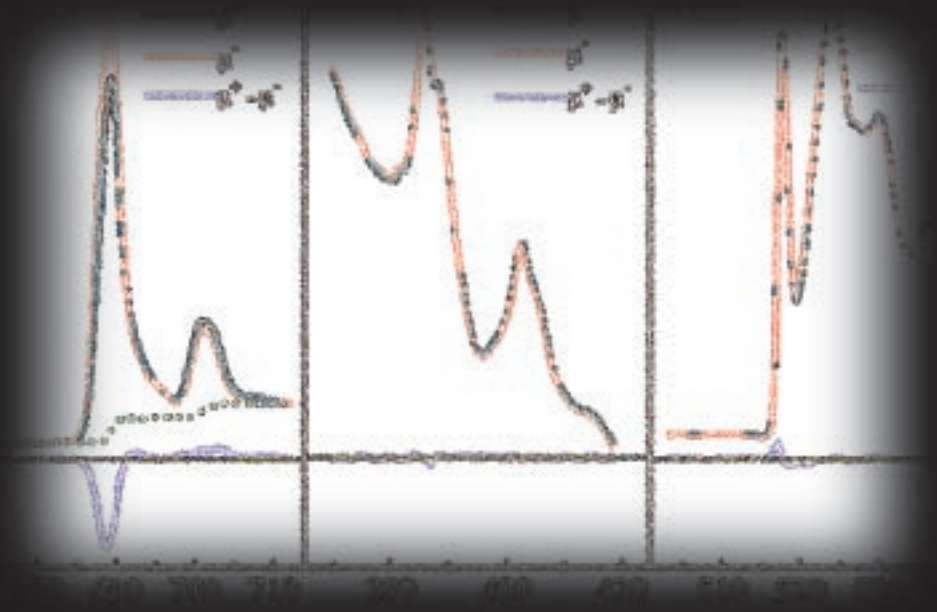

Magnetic Systems

X-ray Magnetic Circular Dichroism Study of Sr_2FeMoO_6

Sugata Ray, Ashwani Kumar,
T. Saha-Dasgupta, D. D. Sarma,
Solid State and Structural Chemistry Unit, Indian Institute of Science, Bangalore 560 012, India

R. Cimino,
Istituto Nazionale di Fisica Nucleare - Laboratori Nazionali di Frascati

S. Turchini,
Istituto di Chimica dei Materiali, CNR- Area della Ricerca di Montelibretti – Roma

S. Zennaro,
Istituto di Struttura della Materia, CNR, sez. Trieste - Trieste

N. Zema,
Istituto di Struttura della Materia, CNR-Area della Ricerca di Tor Vergata - Roma

Colossal negative magnetoresistance (CMR), a large decrease in the resistance (*R*) of a material with the application of a magnetic field, has attracted a great deal of interest due to their potential technological applications. One of the most interesting recent discovery [1] in this area of activity is an ordered double perovskite Sr_2FeMoO_6, with alternating Fe^{3+} ($3d^5$, $S = 5/2$) and Mo^{5+} ($4d^1$, $S = 1/2$) ferrimagnetically coupled ions, exhibiting substantial CMR even at room temperature. This system is supposed to be a half-metallic ferromagnet with very unusual electronic and magnetic properties [2]. Specifically, it is interesting that the magnetic coupling between the strongly correlated magnetic Fe^{3+} ions is mediated over a very long distance *via* oxygen and Mo ions, which are normally expected to be nonmagnetic; yet this system has a very high magnetic transition temperature ($T_C \sim 450$ K). In the proposed [1] magnetic structure, the system is expected to have a moment of 4 μ_B per formula unit (f.u.) due to the ferrimagnetic coupling between Fe^{3+} $3d^5$ and Mo^{5+} $4d^1$ configurations. However, the observed saturation moment in this system from bulk magnetization experiments is most often found to be about 3 μ_B/f.u. Thus, two important questions arise concerning the magnetic structure of this system: (1) is Fe indeed in the 3+ state in this compound with the remaining single electron spin density at the Mo site; and (2) what is the origin of the reduction of the magnetic moment from the expected value of 4 μ_B/f.u., based on the electron count to the experimentally observed value of about 3 μ_B/f.u.? We address these questions combining linear and circularly polarized x-ray absorption spectroscopy in conjunction with *ab initio* large scale band structure calculations. These techniques are obviously ideally suited for the issues addressed here, due to their ability to provide site specific electronic and magnetic information [3].

The experiments were carried out at 77 K using the circularly polarized beamline, 4.2 R. X-ray absorption spectra recorded with linearly polarized light with high resolution, at the Fe $2p_{3/2}$ and $2p_{1/2}$ edges (not shown here) agree with expected spectral features from Fe^{3+} ions in the octahedral cubic crystal field [4]. Thus, the system indeed appears to be in Fe^{3+} - Mo^{5+} state, rather than in Fe^{2+} - Mo^{6+} state, in agreement with Mössbauer results [5, 6]. Figure 1(a) shows the photon-flux normalized polarization-dependent Fe 2*p* XAS spectra, μ^+ (black) and μ^- (red) for highly ordered Sr_2FeMoO_6, corresponding to the helicity parallel and anti-parallel to the Fe 3*d* majority-spin direction, respectively. The dashed line in Fig. 1(a) shows the background, represented by a sum of two arctangent functions with the step energies set at the peaks of Fe $2p_{3/2}$ and Fe $2p_{1/2}$ transitions and with a step-height ratio of 2:1. This background corresponds to transitions from the Fe 2*p* levels to continuum states. The XMCD spectra ($\Delta\mu = \mu^+ - \mu^-$), also shown in the same panel, clearly shows a substantial magnetic signal, indicative of a large Fe moment. The corresponding experimental Mo 3*p* and O 1*s* spectra are shown in Fig. 1(b) and 1(c), respectively, with the respective XMCD signals also shown. It is clearly evident from the XMCD spectrum of Mo that any magnetic moment at these sites is below the detection limit, while the oxygen XMCD signal exhibits a very small but measurable signal. This result shows that the single electron of opposite spin *is not localized* on any of the neighbouring Mo or O ions, with the spin density of this electron being spread out over several sites, namely on the neighbouring six oxygens and six Mo sites as well as on the central Fe site. Band structure calculation [1] clearly shows that the states near E_F arising from this delocalized electron is an admixture of Fe, Mo and O states with significant contributions from all three. As this spin

density is distributed over so many atoms, the effective moment on each individual ion is small, rendering it below the detection limit of the experiment for the Mo site and barely visible for the O site. These results have a striking similarity with previously discussed Zhang-Rice singlet formation in the context of high T_C cuprates [7]. In that case the localized moment at the central Cu site is coupled antiferromagnetically with the doped delocalized hole spin-density spread out over the nearest neighbour oxygen sites to form a singlet state. In the present case, the localized Fe S = 5/2 state couples antiferromagnetically with the spin-density of

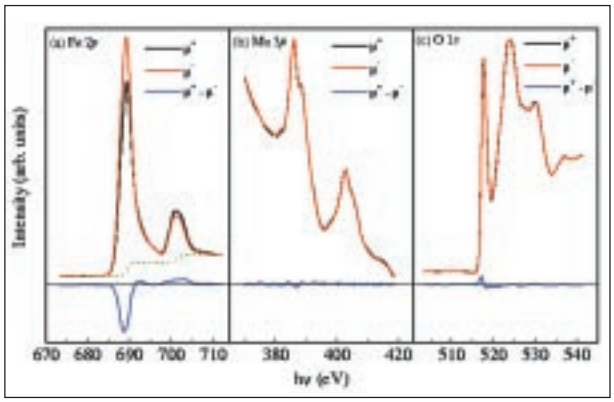

Figure 1: (a) The Fe $2p \rightarrow 3d$ absorption spectra with two different polarizations of light. The difference spectrum is also shown at the bottom.
(b) Mo $3p \rightarrow 4d$ absorption spectra for both polarizations of light and the corresponding difference spectrum.
(c) O $1s \rightarrow 2p$ absorption spectra for both polarizations of light and the corresponding difference spectrum.

delocalized S = 1/2 state to form a S = 2 state.

Now, we address the issue of observing experimentally a lower M_S value for Sr_2FeMoO_6 than is expected on the basis of the simple ionic picture. We establish that the relative ordering between M and M' ions of the compound of general formula $Sr_2MM'O_6$ is responsible for this effect. Extensive band structure calculations from our group [8] clearly show that any disorder between Fe and Mo destroys the half-metallic ferromagnetic state of Sr_2FeMoO_6, leading to a sharp decrease in the magnetic moment at the Fe sites, and consequently, reduces the total magnetic moment of the system. X-ray diffraction studies show that the as-prepared sample of Sr_2FeMoO_6 has about 90% ordering of the Fe and Mo sites [6]. In order to have an experimental control on the extent of ordering, we prepared a sample of Sr_2FeMoO_6 by melt-quenching [6] resulting in approximately 30% ordering. Further, we make use of the fact that the extent of ordering between M and M' sites increases with W doping at the Mo site ($Sr_2FeMo_xW_{1-x}O_6$). It has been recently shown [8] that at x = 0.3, the system becomes fully ordered and the bulk magnetization becomes $4\mu_B$/f.u. We compare the XMCD results at Fe $2p$ edges for the disordered Sr_2FeMoO_6 (melt-quenched Sr_2FeMoO_6), ordered (normally prepared Sr_2FeMoO_6) and fully

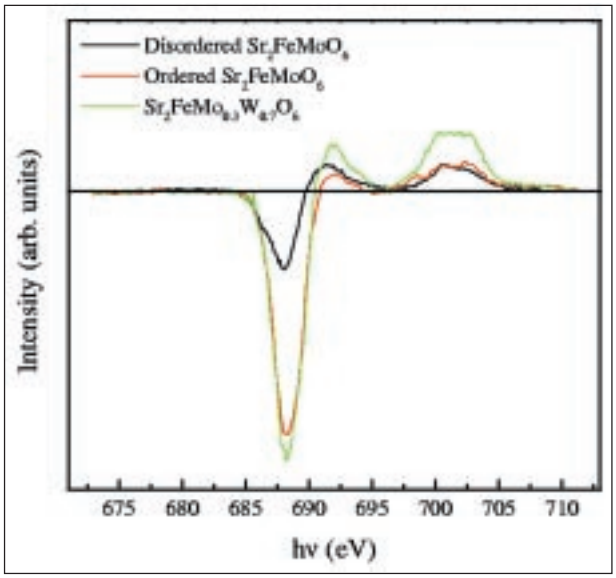

Figure 2: The difference XMCD spectra for disordered and ordered Sr_2FeMoO_6 and $Sr_2FeMo_{0.3}W_{0.7}O_6$.

ordered ($Sr_2FeMo_{0.3}W_{0.7}O_6$) samples in Fig. 2.

It is evident from the spectra that the magnetic moment on individual Fe ions decreases remarkably with decreasing ordering. In order to quantify our results, we have calculated the orbital, spin and total moments at the Fe sites from these spectra using the well established sum rules [3], with the assumption that the magnetic-dipole moment is negligibly small in every case. These results are summarized in Table 1. Evidently, there is a substantial increase in the spin moment at the Fe sites with increasing ordering. It is to be noticed that the magnetic moments obtained from the XMCD results are considerably smaller than the bulk moments obtained from magnetization measurements on the same samples [8]. Such discrepancies are well known in the literature [9], possibly arising from various factors, such as uncertainties in data analysis and near surface region being less magnetic. However, the relative change in the total moments given in Table 1 is in agreement with the observations from bulk magnetization experiments. For example, magnetization data indicates that the W-doped sample exhibits a total moment of about 4 μ_B/f.u., in accordance with its

Sugata Ray, Ashwani Kumar, T. Saha-Dasgupta, D. D. Sarma, R. Cimino, S. Turchini, S. Zennaro, N. Zema

fully ordered state, while the "ordered" Sr_2FeMoO_6 has a moment of 3.1 μ_B/f.u., establishing a 22.5% decrease in the moment due to finite disorder. The present XMCD result shows a 17.6% decrease in the Fe moment in good agreement. The decrease in the Fe moment in the "disordered" Sr_2FeMoO_6 compared to the "ordered" one is 50.2%, in agreement with the sharp decrease in the calculated moment in our band structure results for an extensively disordered configuration. This establishes that the loss of moment in the so-called ordered Sr_2FeMoO_6 is indeed due to the presence of finite mis-site defects, leading to disorder, in the as-prepared samples.

Compound	Spin Moment (μ_B/Fe)	Orbital Moment (μ_B/Fe)	Total Moment (μ_B/Fe)
Disordered Sr_2FeMoO_6	1.17	-0.033	1.14
Ordered Sr_2FeMoO_6	1.89	0.408	2.29
$Sr_2FeMo_{0.3}W_{0.7}O_6$	2.56	0.223	2.78

Table 1.

References:

[1] K. –I. Kobayashi, T. Kimura, H. Sawada, K. Terakura and Y. Tokura; *Nature*, 395, 677, (1998)
[2] D. D. Sarma, Priya Mahadevan, T. Saha-Dasgupta, Sugata Ray and Ashwani Kumar; *Physical Review Letters*, 85, 2549, (2000)
[3] B. T, Thole, Paolo Carra, F. Sette and G. van der Laan; *Physical Review Letters*, 68, 1943, (1992); Paolo Carra, B. T. Thole, Massimo Altarelli and Xindong Wang; *Physical Review Letters*, 70, 694, (1993)
[4] Priya Mahadevan and D. D. Sarma; *Physical Review* B, 61, 7402, (2000)
[5] T. Nakagawa, K. Yoshikawa and S. Nomura; *Journal of Physical Society of Japan*,27, 880, (1969)
[6] D. D. Sarma, E. V. Sampathkumaran, Sugata Ray, R. Nagarajan, Subham Majumdar, Ashwani Kumar, G. Nalini and T. N. Guru Row; *Solid State Communications*, 114, 465, (2000)
[7] F. C. Zhang and T. M. Rice; *Physical Review* B, 37, 3759, (1988)
[8] Unpublished results from the group.
[9] J. Okamoto, H. Miyaguchi, T. Sekine, T. Shidara, T. Koide, K. Amemiya, A. Fujimori, T. Saitoh, A. Tanaka, Y. Takeda and M. Takano; *Physical Review* B, 62, 4455, (2000)

Sugata Ray, Ashwani Kumar, T. Saha-Dasgupta, D. D. Sarma, R. Cimino, S. Turchini, S. Zennaro, N. Zema

Imaging of Magnetic Microstructures

C.M. Schneider, O. de Haas, U. Muschiol,
Institute of Solid State and Materials Research Dresden, Germany

N. Cramer,
Dept. of Physics, University of Colorado at Colorado Springs, USA

A. Oelsner, M. Klais, O. Schmidt, G.H. Fecher, G. Schönhense,
Institute of Physics, Joh.-Gutenberg University Mainz, Germany

N. Zema, S. Zennaro,
ISM-CNR, Rome, Italy

W. Jark,
Sincrotrone Trieste, Italy

Magnetic thin films are the building blocks of devices in magnetic storage technology and magnetoelectronics. They often exhibit unique magnetic and transport properties which are of interest both from a fundamental and an application-oriented point of view as they add specific functions to magnetic thin film systems. Macroscopic magnetic properties are determined by micromagnetic issues and therefore the knowledge of static magnetic microstructures and microscopic magnetization reversal processes is mandatory.

In many magnetic sensor applications the direction rather than the presence or magnitude of a magnetic field needs to be determined. For this purpose a well-defined reference magnetization is required which remains stable in an applied external field. This goal is achieved by means of "spin valve" structures, which consist of two ferromagnetic layers, one of which rotates freely in an external magnetic field. The other magnetic layer is "pinned" via exchange anisotropy to an antiferromagnet to keep its magnetization direction fixed in space. The magnetic behavior of a spin valve system is largely determined by this "exchange biasing" mechanism.

In order to investigate the influence of exchange biasing on the magnetic microstructure, micropatterned $Ni_{81}Fe_{19}$/NiO samples were studied as model systems. Various different micropatterns were prepared. They ranged in size from 100 down to 6 μm.

The multi-element nature of the individual film requires an element-selective investigation of the magnetic microstructure. Soft x-ray magnetic dichroism (XMD) with circularly or linearly polarized light combined with parallel imaging techniques offers a powerful experimental probe of magnetic phenomena on a microscopic scale. Images are formed by electrons emitted from a sample surface (photoemission electron microscopy, PEEM). The PEEM approach combines element selectivity with surface sensitivity, because of its finite information depth of the order of 20 – 40 Å. The technique is also able to determine magnetic quantities with submonolayer sensitivity.

The experiments were carried out at the electromagnetic wiggler/undulator beamline 4.2R, providing light with a variable polarization in the range 5 – 1000 eV. The experiments described in the following used only light with elliptical polarization and a dedicated photoemission microscope. The magnetic contrast in ferromagnetic samples can be enhanced by aligning the local magnetization vector $\underline{M}$ with the direction of light incidence $\underline{q}$.

The figure gives an example for the results obtained from a frame-shaped structure with 100μm leg length (image recorded at the L_3 edge of Ni). In a soft magnetic material, such as $Ni_{81}Fe_{19}$ (Permalloy), the domain pattern should be essentially governed by flux closure arguments. Instead of a simple flux closure pattern, however, the structure in the figure

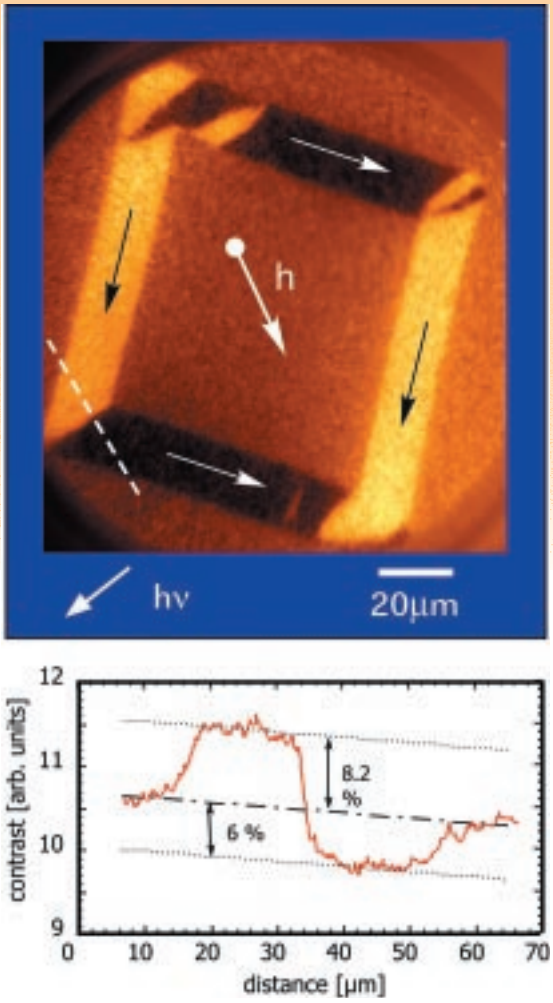

exhibits a more complicated behavior. First of all, the magnetic contrast exhibits only two distinct gray levels (the sample has been rotated to optimize the magnetic contrast) within the experimental uncertainty. When rotating the sample by about 90° the magnetic contrast disappears. From this information one can reconstruct the dominant features of the local magnetization orientation (arrows). The extended dark and bright areas are related to two *orthogonal* magnetization directions, both of which have a net component along the frame's vertical diagonal (direction denoted by h). This domain pattern strongly suggests the presence of exchange anisotropy (pinning) along h. Quantitative information about the orientation of the magnetization is gained from line scans, such as the one marked by the broken line. It reveals the absolute values of the dark and bright contrast to differ slightly and being asymmetric with respect to the intermediate contrast level (bottom graph). The latter corresponds to vanishing magnetic contrast. The imbalance in the contrast levels is caused by the incoming light (q) making an angle of ~10-15° with the frame's horizontal diagonal.

The second finding concerns the magnetic domain boundaries. Almost all of them run roughly perpendicular to h. The reconstructed magnetization pattern suggests a formation of 90° walls at the left and right hand corner of the frame, which is consistent with the experimental findings. This situation clearly causes unfavourable magnetic configurations (higher stray field) in the top and bottom corner, where smaller domains and presumably magnetically charged walls are detected. These configurations reflect the competition between the uniaxial or unidirectional anisotropy and the demagnetizing field.

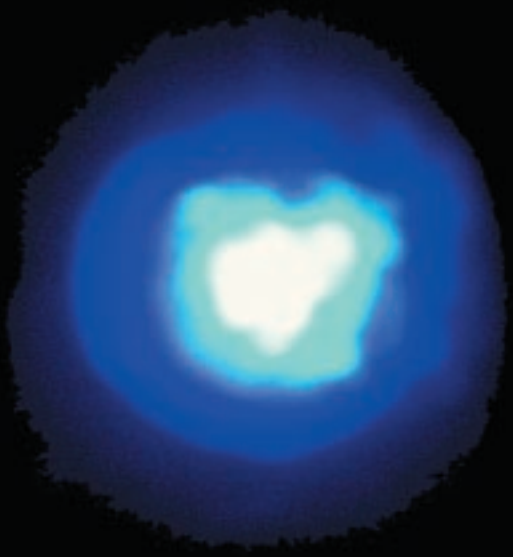

Machine Status

Machine Status

Operations and Ongoing Developments

C. J. Bocchetta,
Sincrotrone Trieste, Italy

At the end of 1999 ELETTRA completed six years of operation for the User community. Over this period 25800 hours were dedicated to the Users from a total of 34800. Figure 1 shows the distribution of the total and User time including that programmed for the year 2000.

During 1999 the facility operated for 6192 hours of which 5088 were scheduled to the users mainly operating a 2.0 GeV. The operating hours were distributed in eight runs of four to eight weeks duration separated by nine shutdown periods for systems maintenance and equipment installation, notably: new front ends, insertion devices and their vacuum chambers. The user uptime for 1999 was 89.8% (including storms and electricity micro-interruptions). Excluding these external factors the net user uptime was 92%, see figure 2. The major downtime contributions came from: storms and power interruptions 22%, power supplies 14% and water system 12% (see figure 3). As in previous years normal operation for Users involved one injection per day with a starting beam current of 320 mA (7 hours lifetime) that decayed to ~100 mA (35 hours lifetime) after 24 hours. While the nominal beam energy remained at 2.0 GeV a significant fraction of the scheduled User time was also spent at 2.4 GeV (22%). At the higher energy the maximum beam current is limited to 120 mA (36 hours lifetime) to contain the thermal load on the vacuum chamber at acceptable values. The usual mode of operation is multibunch where roughly 90% of the ring circumference is filled with electrons.

The schedule for 2000 consists of seven runs for a total of 6504 hours of which 5016 are dedicated to User operation. The installation of new insertion devices, their chambers and front ends have as in previous years determined the length and number of

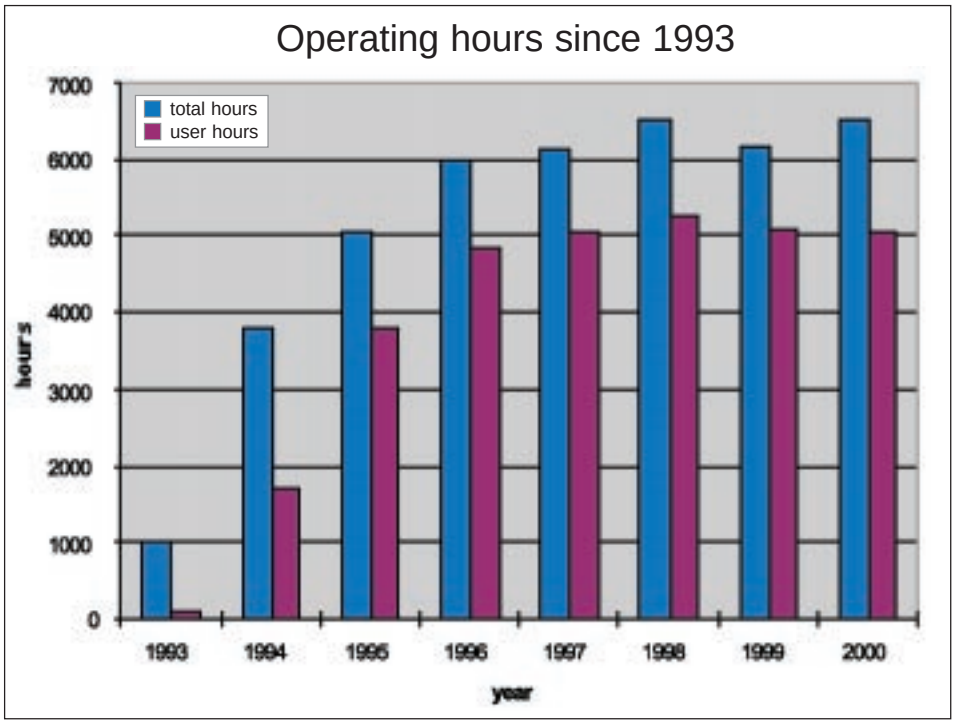

Figure 1: Operating hours since 1993

operation periods. Roughly 25% of the User time was scheduled with a beam energy of 2.4 GeV.

Many machine studies have been performed to better understand the behaviour of the light source. These measurements have included studies on ion-trapping and gas Bremsstrahlung (especially associated with the conditioning of new aluminium vacuum chambers), bunch lengthening and machine impedance, beam instabilities and studies for storage ring free-electron-laser (FEL) operation. In this context the streak camera has proven to be a powerful diagnostic tool allowing pico-second resolution both in single shot bunch length measurements and in long-term (tens of milliseconds) observation (see figures 4a-4b). A significant fraction of machine physics time was utilised for conditioning of new vacuum chambers. The gradual addition of smaller gap vacuum chambers has also increased the transverse impedance of the machine by a factor six since 1994. This in turn means that the maximum single bunch current is limited to around 20 mA when operating with near zero chromaticity.

Significant work was performed during the past year to improve the basic operational characteristics of the light source, namely the photon sources, brightness, lifetime and reliability. The activities have focused on improved operations and on the development of new insertion devices that provide elliptically polarised radiation, a transverse multibunch feedback system, new position monitors - both electron and photon, a superconducting third harmonic cavity, a UV/VUV storage ring based free electron laser and a full energy injector. The majority of these activities are still underway and only a brief description will be given. The free-electron laser and the new photon beam position monitors are described in more detail below.

The understanding of beam losses not associated with a hardware fault has greatly improved. These losses typically amounted to about 40 events per year of which a third could be tied to evident storms or mains interruptions. All of these losses were associated with the fast interlock system that intervenes to protect the vacuum chamber against mis-steered insertion device (ID) radiation beams, based on electron Beam Position Monitor (BPM) readings. Two systems were set up to monitor the stability of various magnet power supplies mains circuits and to monitor the interlock system by registering the last one second of BPM data. The

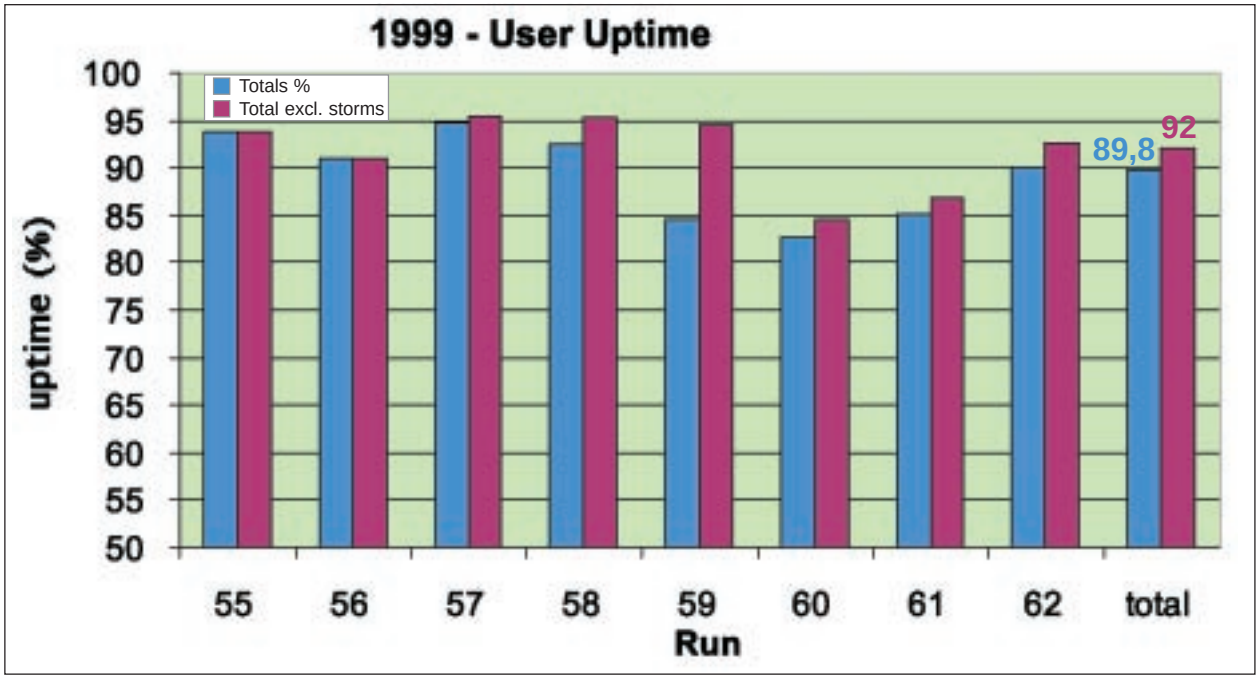

Figure 2: 1999 User uptime

result of this analysis is that 70 % of these losses (up to 14 % of all beam losses) can be associated with disturbances of the mains (including both mains dips and micro-interruptions). The remaining 30 % (about 12 per year) can be divided equally between those in which the interlock kills the beam because a real beam movement has occurred, and those in which the beam is lost prior to the interlock action.

Further progress has been made with the correction of the orbit distortion introduced by the Electromagnetic Elliptical Wiggler (EEW). A slow feed-forward correction loop, acting on special correction coils on either side of the device, has allowed users to have direct control of EEW currents during d.c. operation since December 1998. The a.c. mode however introduces a regular disturbance that was not initially acceptable to users on other SR beamlines. To improve the correction it was found necessary to take into account the magnetic hysteresis by creating two calibration curves, for increasing and decreasing currents. The change in global orbit was corrected at each current step to a level of 1 µm rms, i.e. at the limit of sensitivity of the BPM system. After averaging a number of such calibration curves acceptable performance was obtained. At the same time a new system architecture has also been set up which uses the same DSP for both principal waveform generation and orbit correction. The EEW can now be operated during user shifts in a.c. mode for fixed wiggler mode settings (+160 A vertical field, ± 260 A horizontal field) with a slow trapezoidal waveform (1 s ramp, 5 s flat-top).

In the last two years six elliptical undulator modules (each 2.0-2.2 m long), four new aluminium ID vessels, four new bending magnet (BM) vessels as well as six ID and BM beamline front-ends have been installed. Three ID straight sections each contain two APPLE-type undulator modules with periods ranging from 4.8 cm to 12.5 cm, one of which is a novel quasi-periodic design. The six devices installed so far have all reached very good performance: rms phase errors of < 3.5 deg. (apart from the first device, 4.5 deg.) and field integrals < 2.5 Gm and 3 Gm2, at any gap and phase. Commissioning of the devices in the ring with electron beam has been performed during the past year, including extension of the usual feed-forward closed orbit correction system to include both gap and phase. A storage ring free-electron laser utilising two of these new devices has been developed by a

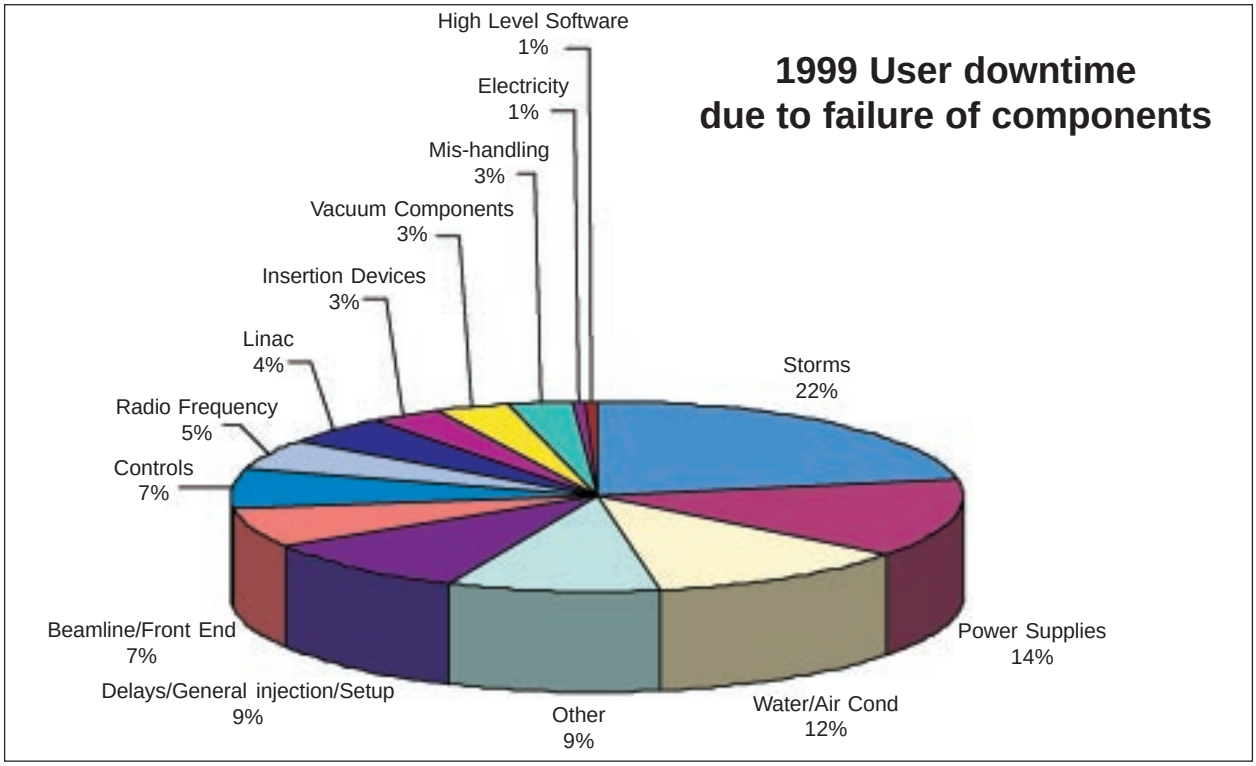

Figure 3: Sources of User downtime

European collaboration as a future facility for users in the UV/VUV range (350-190 nm) of which further details can be found below.

In order to permit the installation of elliptical undulators, with a larger vertical radiation opening angle compared to planar devices, particularly those with large K values designed for low photon energies, it has been necessary to improve the cooling in the region of the radiation slot in the downstream bending magnets. New chambers have therefore been constructed made of aluminium alloy with integral cooling channels. Four such chambers have been installed, two with an enlarged slot height of 20 mm (instead of the usual 10 mm) in the region of the light exit to ease operation of the free-electron laser (see below). In addition, four new ID vacuum chambers have been built and installed based on extruded aluminium, each 4.7 m in length, with internal/external vertical dimension of 14/17 mm. Based on previous positive experience with ID vessels with no lateral pumping, these new chambers were also based on that concept. Conditioning of these chambers has been slower than for previous stainless steel vessels, particularly for the ID vessels, which have required approximately 100 Ah of beam dose to recover the beam lifetime (see figure 5)

In an effort to improve beam orbit stability, both locally at the ID source points, as well as globally, a new low-gap BPM system has been undergoing development, to provide stable sub-µm resolution position signals based on the following key elements:

• Higher sensitivity BPM geometry based on the narrow gap (14 mm) ID vacuum chamber cross-section.

• A novel digital detector developed jointly with the SLS Project (PSI, Switzerland) consisting of a 4-channel RF front-end, 4 channel digital receiver and DSP module, providing optimised resolution/bandwidth for different detector modes: closed orbit, feedback, turn-by-turn and single pass.

• A stable support system for the BPM block, which is isolated from the rest of the vacuum system by means of bellows on either side.

• Monitoring of the residual motion of the BPM to sub-micron accuracy by means of capacitive sensors with respect to a separate highly stable (1.9 µm/°C expansion) reference column based on carbon epoxy laminate.

Measurements with a prototype RF front-end

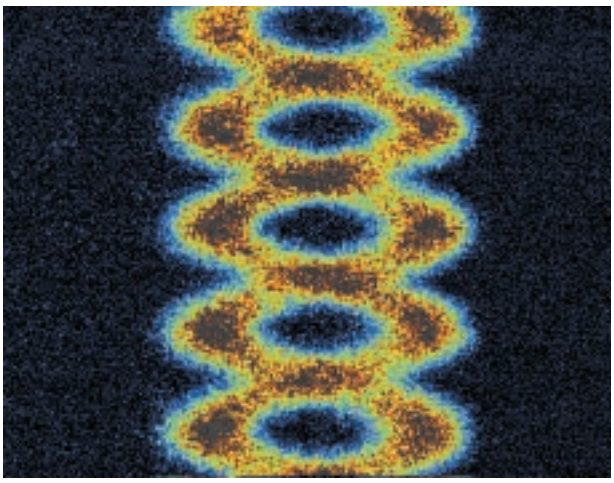

Figure 4a: Longitudinal multibunch oscillations of four bunches at 1.0 GeV and 19 mA before stabilisation by mode-cancellation performed by cavity temperature tuning.

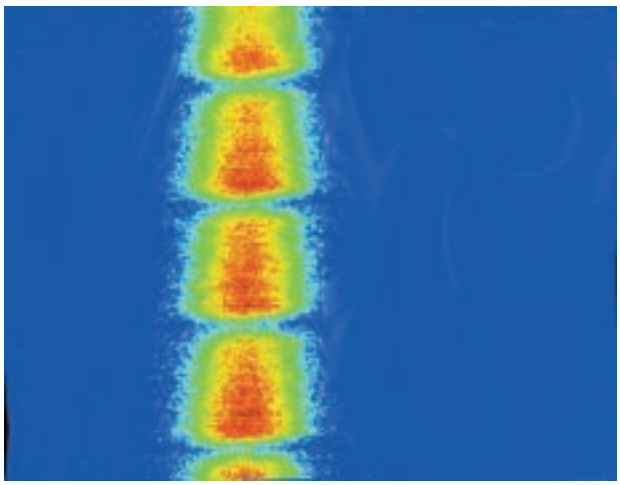

Figure 4b: Stable longitudinal operation of a multibunch filling (90%) at 2.0 GeV and 100 mA. Vertical dimensions correspond to 3.45 micro-seconds, horizontally to 441 pico-seconds.

and digital receiver confirmed the position resolution of 1.6 µm rms in closed-orbit mode (1 kHz bandwidth). Two prototype low-gap BPMs as well as the position monitoring system were installed in January 2000. Subsequent tests have confirmed the sub-µm resolution of the position monitoring system, as well as a factor of 2.6 improvement in sensitivity of the new BPM geometry. A new type of photon BPM has also been developed for undulator beamlines as a second, independent, position monitor and one that could also be used in a feedback loop for particularly sensitive beamlines of which more details are given below.

Normal operation of ELETTRA is with a controlled amount of longitudinal excitation introduced by adjustment of r.f. cavity temperatures, in order to stabilise the beam against transverse instabilities, as well as to increase the lifetime. To permit stable longitudinal conditions to be obtained therefore requires overcoming transverse multibunch instabilities and to this end a digital transverse feedback system is being developed, in collaboration with the SLS Project. Horizontal and vertical kickers, constructed at PSI, and the new BPM r.f. front-ends were installed in April 2000 and first tests carried out. In order to offset the reduction in beam lifetime that will result when the ELETTRA beam is fully stabilised, an idle superconducting 3rd harmonic cavity is being developed, in collaboration with CEA-DAPNIA (Saclay, France) and SLS. The first phase of the project, involving the cavity design, construction and characterisation of a copper model and preliminary cryomodule design have been performed this past year. Plans are underway for the second phase that foresees installation of the final system in March 2002.

A major handicap to the efficiency, stability and future potential of ELETTRA is the lack of a full-energy injector. During the last year a significant effort has been dedicated to the completion of a design study for a full-energy injector based on a 100 MeV linac and 2.5 GeV booster synchrotron. The booster would be located in the presently open area on the inside of the ring and could be constructed and tested without interference to storage ring operation. A relatively short shut-down of three to fours months would be required for connection to the storage ring and for commissioning. Following a major project review in May 2000, a final optimisation of the design is presently underway.

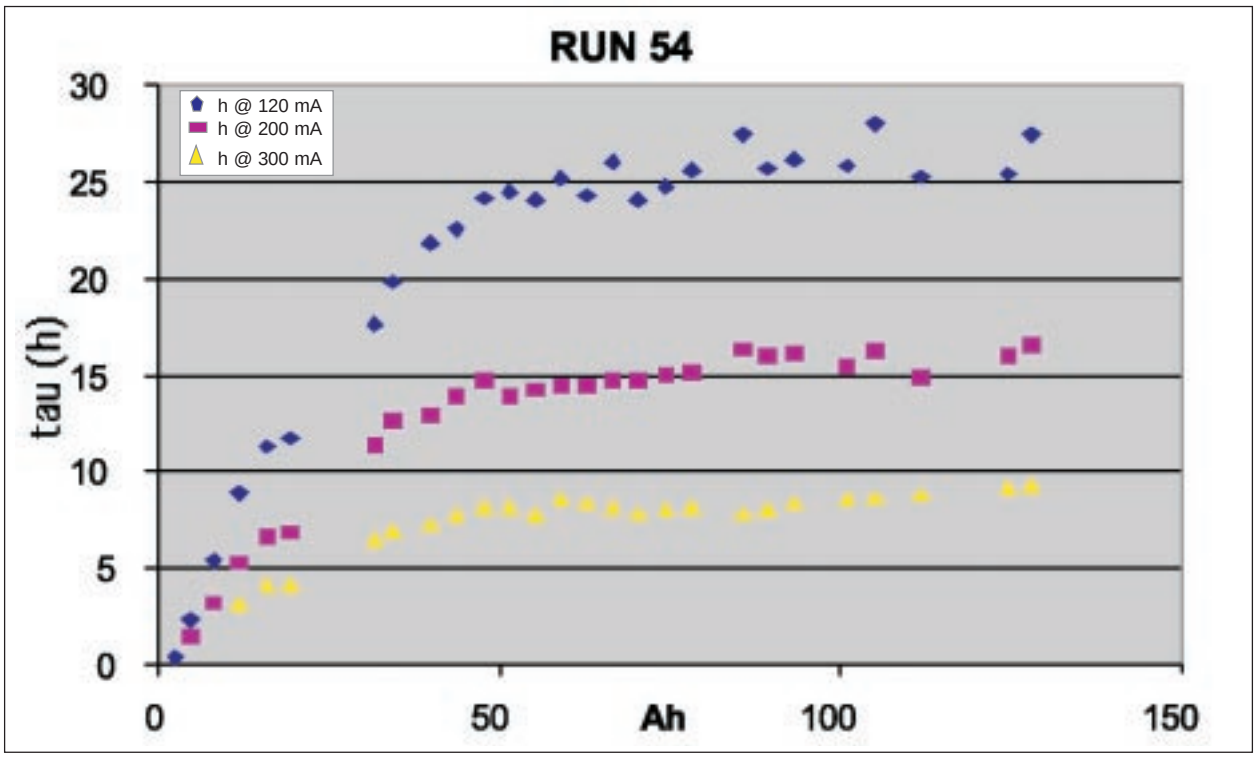

Figure 5: Lifetime as a function of Ampere – hours of circulating current after the installation of new aluminium vacuum chambers. Roughly 100 Ah are required to condition these chambers.

First Light from the European Storage Ring Free-Electron Laser Project on ELETTRA

R. Walker,
Sincrotrone Trieste, Italy

A free-electron laser (FEL) is a source of intense, coherent, monochromatic radiation similar to that of a conventional laser but using an electron beam as its 'lasing medium'. Since its operation is not linked to particular atomic or molecular transitions the advantage of such a scheme is the possibility of achieving a wide wavelength tunability, reaching otherwise inaccessible regions of the spectrum. Another advantage is the possibility of producing very high peak and average powers, since there is no material medium to cause breakdown problems.

In the most common oscillator type of FEL, synchrotron radiation emitted in an undulator is reflected back and forth between two mirrors which form an "optical cavity". The length of the cavity is adjusted precisely so that the radiation pulses pass

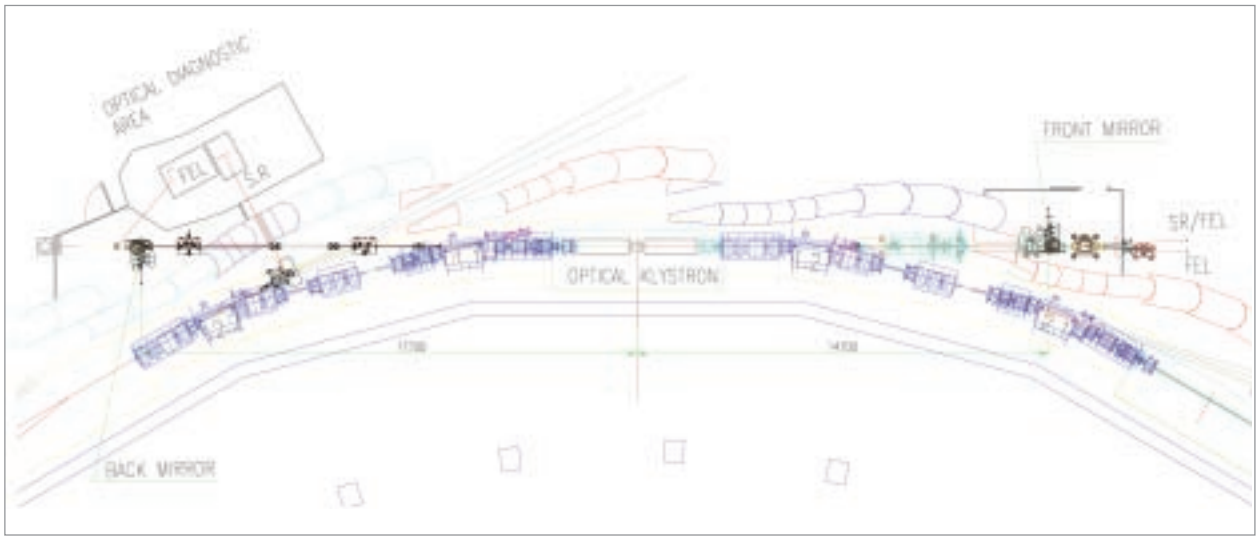

Figure 1. Layout of the Free-Electron Laser in ELETTRA.

through the undulator in synchronism with the electron bunches circulating in the ring. The interaction between them causes a bunching of the electrons on the optical length scale, which results in the emission of coherent laser radiation.

The FEL project on the ELETTRA storage ring aims to capitalise on the availability of a high quality electron beam to develop a source of intense UV/VUV radiation in the 350-190 nm range as a potential future user facility. Such a source, used by itself or in conjunction with SR from other beamlines, will open up the possibility of a range of interesting studies in several research fields, thanks also to the proximity of advanced instrumentation and to the interdisciplinary environment of a third generation synchrotron radiation source. The project got underway in May 1998, when partial funding became available from the European Commission under an RTD grant. The partners who have contributed to the project are CEA-LURE (France), CLRC-Daresbury Laboratory (England), University of Dortmund (Germany), ENEA-Frascati and MAX-lab (Sweden).

The implementation of the FEL in ELETTRA is shown in fig. 1. A standard switching mirror following the front mirror chamber will allow use of the undulator radiation during normal storage ring operation by the Nanospectroscopy beamline, which is presently nearing completion. One of the distinguishing features of the present FEL project is the use of helical undulators in order to reduce the power load and hence damage of the delicate mirrors, a technique successfully demonstrated at UVSOR in Japan. Another feature is the design of the mirror

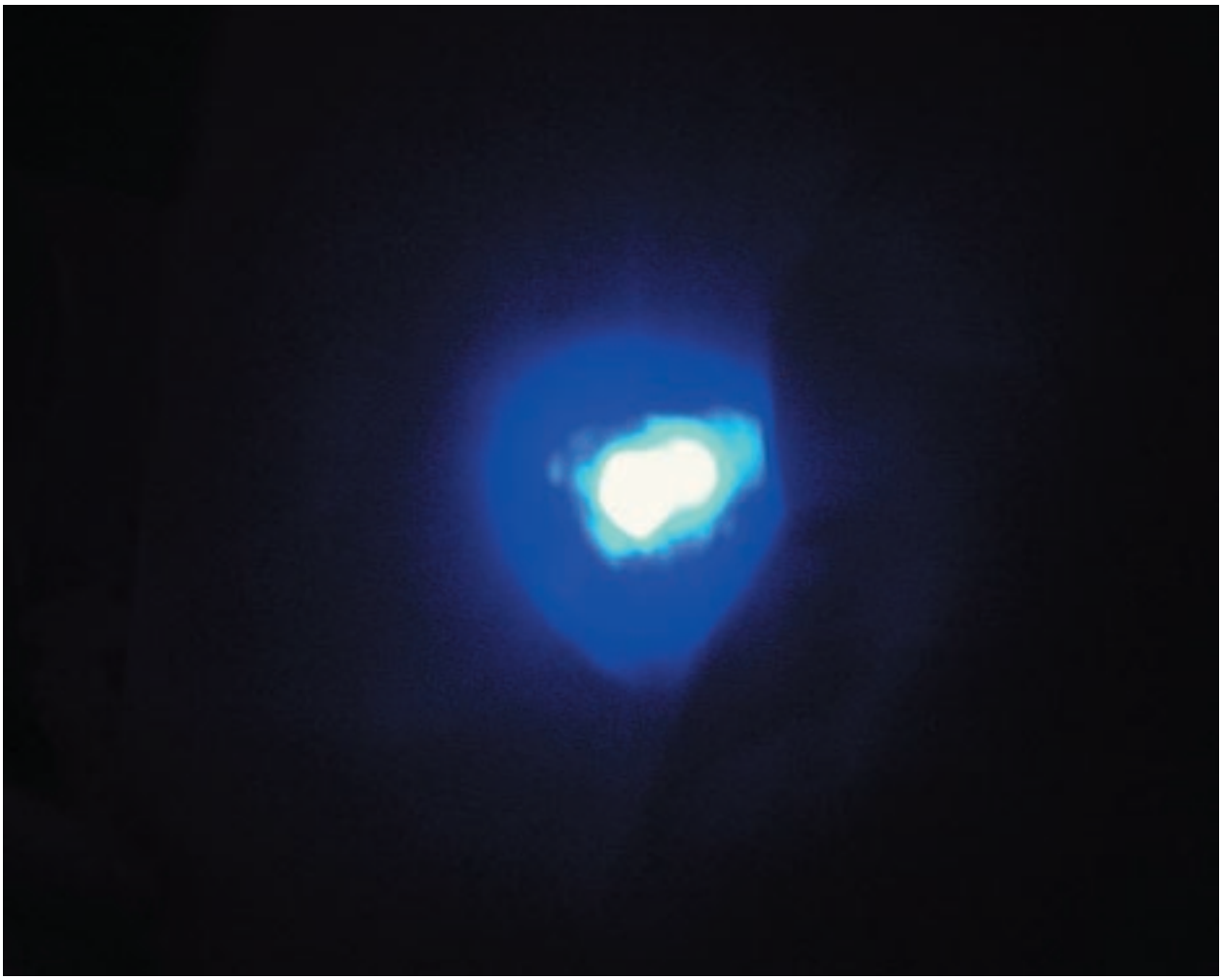

Figure 2. Photograph of the fluorescence induced by the FEL radiation striking a white screen.

chambers, developed at Daresbury Laboratory, which allows an in-vacuum switching between 3 mirrors, in order to extend the wavelength range that can be covered, as well as to maximise use of the limited commissioning time.

Installation of the first hardware components began during the August 1999 shutdown, starting with the undulators and associated new vacuum chambers and beamline front-end, and was completed in mid February 2000 following delivery in January of the two mirror chamber units from Daresbury Laboratory, and the first set of high reflectivity UV multilayer mirrors from LURE.

FEL commissioning began in mid February, and first lasing was obtained on February 29th, after only 30 hours of beam time, at a wavelength of 355 nm. Figure 2 shows a photograph of the fluorescence induced by the UV radiation on a white card. Subsequent work has been divided between studying the operation of the FEL, and in attempting to reduce the wavelength. On May 27th lasing was successfully obtained between 218 and 224 nm. (Only two other oscillator FELs in the world have so far been operated at shorter wavelengths, 212 nm was obtained at the NIJI-IV ring in Japan, while the current record of 194 nm was reached at Duke University, USA).

Measurements of the FEL radiation have shown that the main features are in good agreement with expectations, confirming therefore the suitability as a source for carrying out experiments. Figure 3 shows the spectral line at 224 nm with the smallest linewidth recorded so far of 0.05 nm (FWHM), i.e. a relative width of 2.2 10-4, which is quite suitable for experimental use without further monochromatisation. The optical pulse length is of the order of 10 ps (FWHM). The maximum average output power of 30 mW is also at the level of being useful for experiments, however at least an order of magnitude increase will be possible in the future with optimised mirror transmission

Future work will continue in studying and improving the FEL performance, addressing also important stability and reproducibility aspects. Further attempts will also be made to reach shorter wavelengths but in parallel another main aim is to carry out some pilot experiments, using FEL light as excitation source for an electron emission microscope to study the electronic properties of nanostructures with threshold photoelectrons.

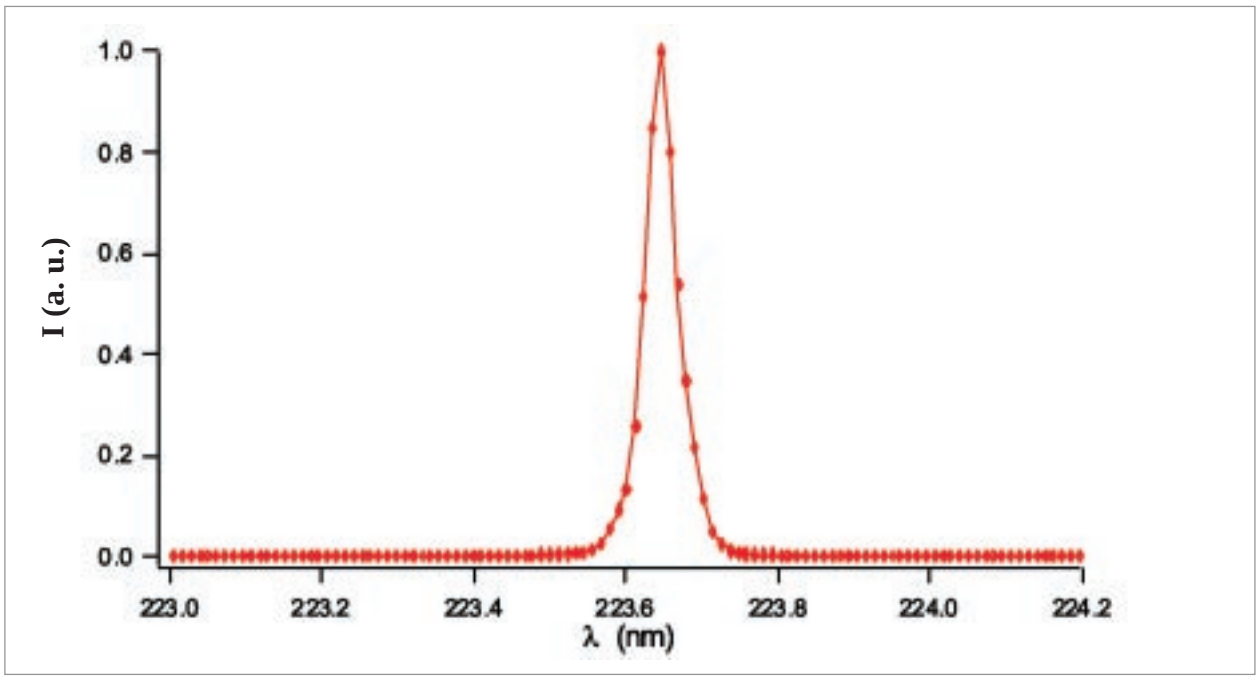

Figure 3. Measured Spectrum of FEL radiation in the region of 224 nm.

The project is supported by EC RTD Contract No. ERBFMGE-CT98-0102, involving the following partners and participating persons:

Sincrotrone Trieste: *A. Abrami, L. Battistello, R. Bracco, B. Diviacco, A. Fabris, C. Fava, M. Ferianis, P. Furlan, A. Gambitta, R. Godnig, E. Karantzoulis, F. Iazzourene, G. Loda, M. Lonza, M. Marsi, F. Mazzolini, G. Pangon, N. Pangos, M. Pasqualetto, C. Pasotti, F. Pradal, R. Roux, M. Svandrlik, G. Tromba, M. Trovò, A. Vascotto, R. Visintini, D. Zangrando*

CEA-SPAM and LURE, Orsay, France: *M.E. Couprie, D. Garzella, L. Nahon, D. Nutarelli, E. Renault*

CLRC-Daresbury Laboratory, Warrington, UK: *N. Bliss, A.A. Chesworth, J.A. Clarke, B. Fell, C. Hill, R. Marl, I.D. Mullacrane, M.W. Poole, R.J. Reid*

University of Dortmund, Germany: *D. Nölle, H. Quick, K. Wille*

ENEA-Frascati, Italy: *G. Dattoli, L. Giannessi, L. Mezi, P.L. Ottaviani, A. Torre*

MAX-lab, Lund, Sweden: *M. Eriksson, S. Werin*

New Photon Beam Position Monitor (For Undulator Beamlines)

A. Galimberti,
Sincrotrone Trieste, Italy

The most common Photon Beam Position Monitor (PBPM), used in synchrotron radiation facilities, is the so called blade-monitor that is based on the principle of photoemission. When this device is used in an undulator beamline there is an unwanted effect arising from dipole radiation that hits the PBPM. The configuration of the storage ring magnets allows a significant part of the radiation from the upstream and downstream dipoles to go down the undulator beamline. In order to have a PBPM system that is suitable in any feedback control loop (including one that allows insertion device gap changes when an orbit feedback is active), we have to drastically reduce errors induced by the dipole magnet radiation to less than 0.1%. The new PBPM developed at Elettra has achieved this goal. A first prototype, acting only in the vertical plane, has been built (figure 1). It consists in two photoemissive graphite blades coupled with two Electron Energy Analysers that collect the electrons photoemitted by the blades when they are hit by the photon beam. The analysers perform a sort of bandpass filtering on the electron

Figure 1: The New PBPM prototype layout. The flange of the manipulator supports the detector. The main active elements are visible: the blades, that intercept the photon beam, and the hemispherical analysers that collect and filter the photoemitted electrons.

energies in order to retain only those electrons within a narrow energy bandwidth centred on a desired undulator harmonic and rejects all contributions to the signal coming from electrons with different energies. Within the energy range preserved, the undulator photon flux is greater than that of the dipole by a factor ranging from 100 to 1000, depending on the undulator settings. This flux difference allows us to reduce the contamination coming from dipole magnet radiation down to a range from 0.1% to 0.01%.

A series of spatial scans of the photon beam cross-section was performed by moving the detector and using its X-Z manipulator. The whole photon beam is visible inside the front end as seen by the traditional arrangement of blades (figure 2a) and by the new PBPM (figure 2b). The dimensions are very different. In fact the traditional blade integrates both in space and in energy while the new PBPM reduces the spatial integration and takes only a few eV of the whole energy bandwidth. Figure 2b therefore shows a narrow peak essentially only due to the undulator harmonic considered. Figures 2c and 3d show the photon beam seen as pure dipole magnet radiation for the traditional blades (2c) and for the new PBPM (2d). The comparison of figures 2c and 2d is impressive. In the first a huge photon lobe seems to cover the largest amount of the space, in the latter a noise-level peak shows a very low residual dipole magnet radiation component.

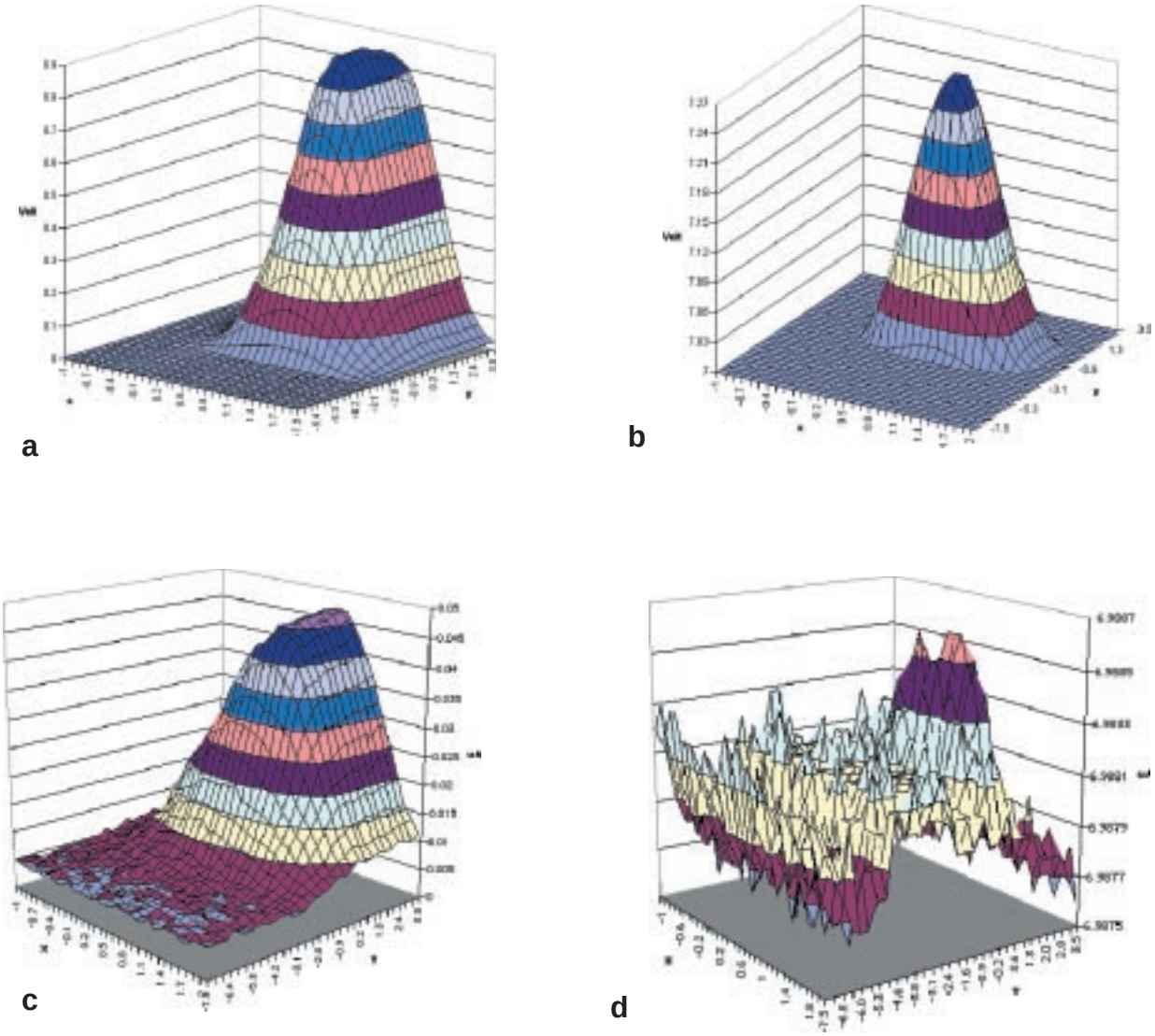

Figure 2: A spatial scan shows the photon beam as seen by photoemissive blades in an undulator beamline: a) Traditional blade PBPM (both undulator and dipole radiation) b) New PBPM (both undulator and dipole radiation) c) Traditional blade PBPM (only dipole radiation) d) New PBPM (only dipole radiation).

Both the linearity and sensitivity of the detector were examined by performing a vertical scan about the photon beam centre with a correctly centred monitor. A 3 mm scan in steps of 60 µm was made. The overall linearity is the same as for a traditional monitor but is restricted to a 1 mm range dependent on the shape of the harmonic.
A more refined scan was made to determine the limit of resolution. The detector was moved in steps of 1 µm over range of 100 µm using a stepping motor and an optical encoder configured in a servo-loop. The new monitor is sensitive to micron level beam movement, similar to a traditional monitor, but with a very effective reduction in dipole magnet contamination (figure 3).

NEW PHOTON BEAM POSITION MONITOR VERTICAL SENSITIVITY

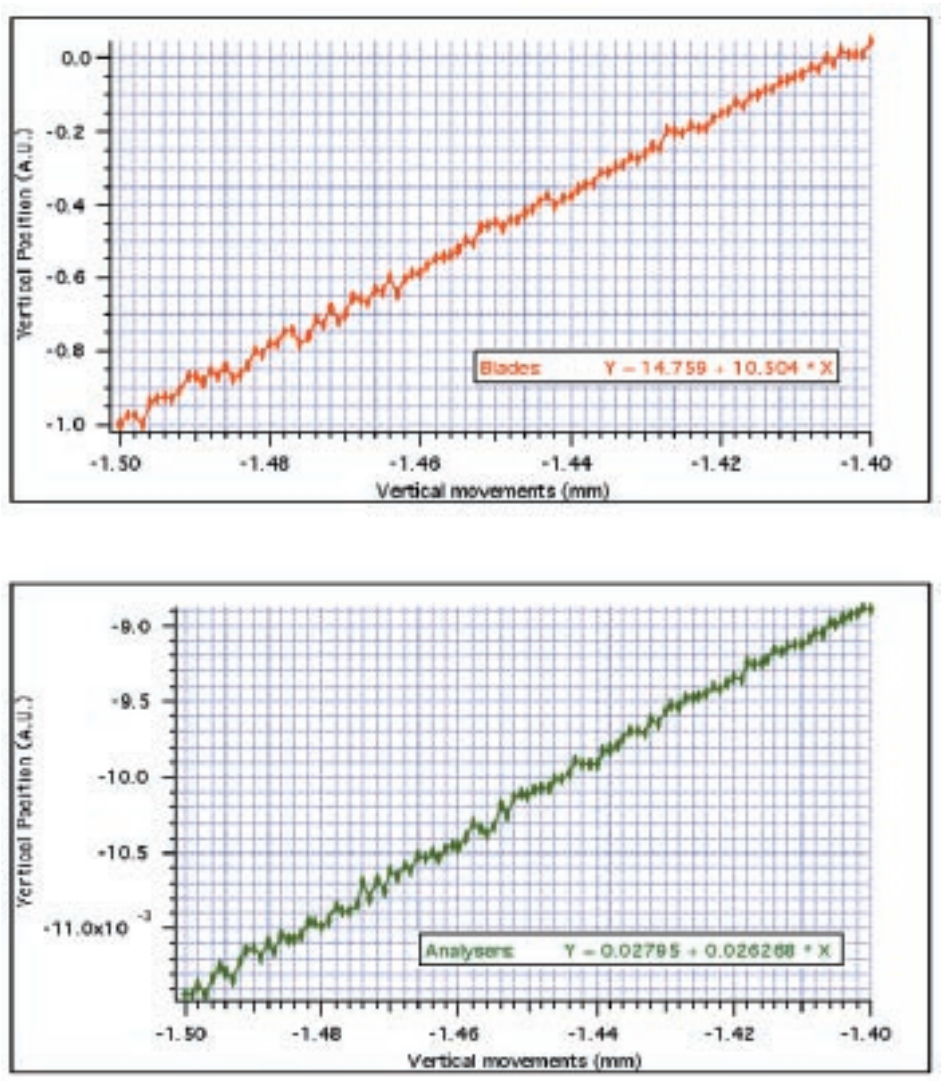

RUN 63 - JANUARY 2000 - EEW (I_v=20A, I_h=0A)

Figure 3: Micron level sensitivity is shown for the traditional blades and the new PBPM both as calculated vertical position.

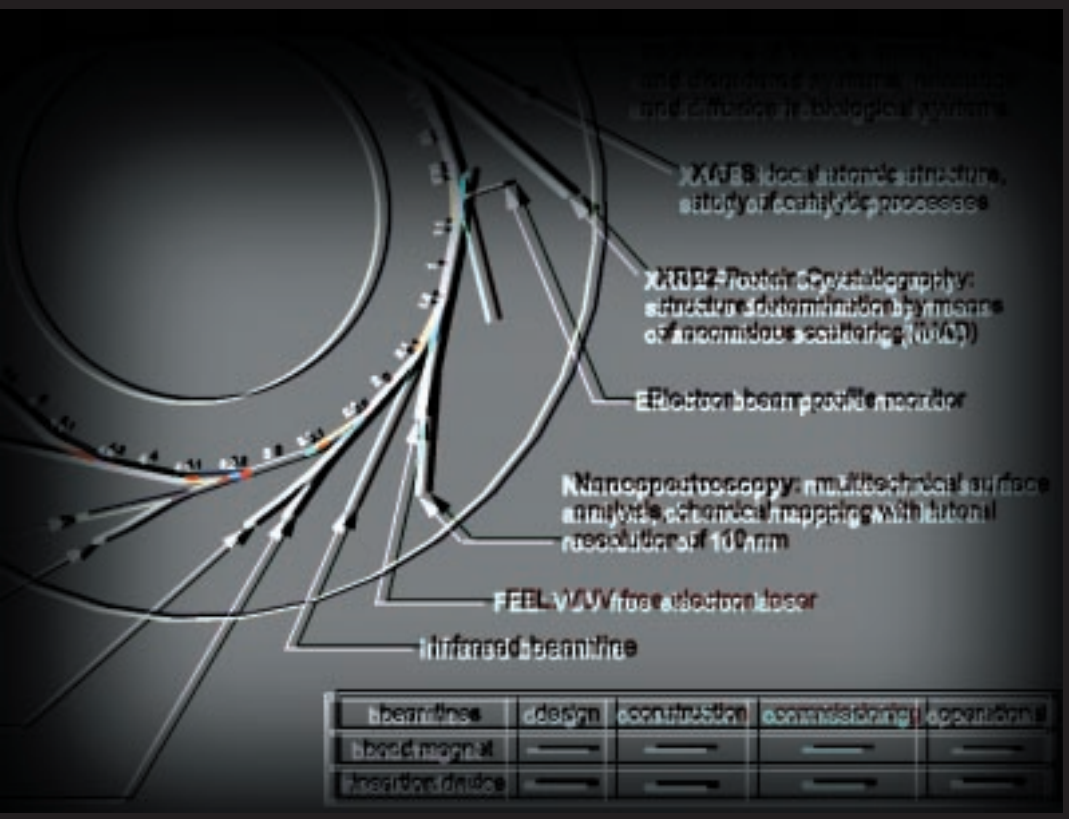

Facts & Figures

Facts & Figures

STATUS	N°	BEAMLINE	RT's INSTITUTION	PHOTON SOURCE
Operational	1	SUPERESCA	SINCROTRONE TS	UNDULATOR U 5.6
	2	ESCAMICROSCOPY	SINCROTRONE TS	BRANCH LINE OF N° 1
	3	VUV PHOTOEMISSION	CNR-ISM	UNDULATOR U 12.5
	4	X-RAY DIFFRACTION	CNR	WIGGLER W 14.0
	5	X-RAY SMALL-ANGLE SCATTERING	AUSTRIAN ACADEMY OF SCIENCES	BRANCH LINE OF N° 4
	6	SURFACE DIFFRACTION (ALOISA)	(CNR) INFM	U 8.0 UNDULATOR/WIGGLER
	7	GAS-PHASE PHOTOEMISSION	CNR-IMAI INFM UNIV. OF ROME	U 12.5 UNDULATOR
	8	MAMMOGRAPHY (SYRMEP)	UNIVERSITY OF TRIESTE-INFN	BENDING MAGNET
	9	SPECTRO-MICROSCOPY	SINCROTRONE TS EPFL-CXRL	BRANCH LINE OF N° 3
Under commissioning	10	CIRCULARLY POLARIZED LIGHT	CNR-ISM CNR-ICMAT UNIV. OF ROME I	CROSS FIELD UNDULATOR/ WIGGLER
	11	DEEP LITHOGRAPHY	SINCROTRONE TS	BENDING MAGNET
	12	PROXIMITY PHOTOLITHOGRAPHY (LILIT)	INFM	BENDING MAGNET
	13	MATERIALS SCIENCE	CZECH ACADEMY OF SCIENCES - PRAGUE	BENDING MAGNET
Under construction *Approved by the Scientific Advisory Committee and Board of Directors*	14	XAFS	UNIV. OF TRIESTE	BENDING MAGNET
	15	BEAMLINE FOR ADVANCED DICHROISM (BACH)	INFM	CROSS-FIELD UNDULATOR
	16	DICHROIC PHOTOEMISSION (APE)	INFM	CROSS-FIELD UNDULATOR
	17	SOFT X-RAY OPTICAL SPECTROSCOPY (X-MOSS)	INFM	BENDING MAGNET
	18	XRD II	SINCROTRONE TS	WIGGLER
	19	NANOSPECTROSCOPY	SINCROTRONE TS	FEL UNDULATOR
	20	INELASTIC ULTRAVIOLET LIGHT SCATTERING	SINCROTRONE TS	UNDULATOR
	21	POWDER DIFFRACTION	CNR-UNIV. OF TRENTO	BENDING MAGNET
Approved by the Scientific Advisory Committee	22	IR BEAMLINE	UNIVERSITY OF ROME I	BENDING MAGNET
	23	MINIUNDULATOR	CNR	UNDULATOR
	24	BIOSPEC	CNR	BENDING MAGNET
	25	MEPHISTO	CNR	BENDING MAGNET
	26	PHOTOABSORPTION SPECTROSCOPIES	CNR	BENDING MAGNET
	27	LOW PHOTON ENERGY HIGH-RESOLUTION PHOTOEMISSION (LEMON)	CNR	BENDING MAGNET
	28	MULTIPURPOSE X-RAY BEAMLINE (BOSS)	J. STEFAN INSTITUTE LJUBLJANA	BENDING MAGNET
	29	FLUORESCENCE MICROANALYSIS	SINCROTRONE TS	BENDING MAGNET
	30	SOFT X-RAY TEST BL	SINCROTRONE TS	BENDING MAGNET
	31	HARD X-RAY TEST BL	SINCROTRONE TS	BENDING MAGNET

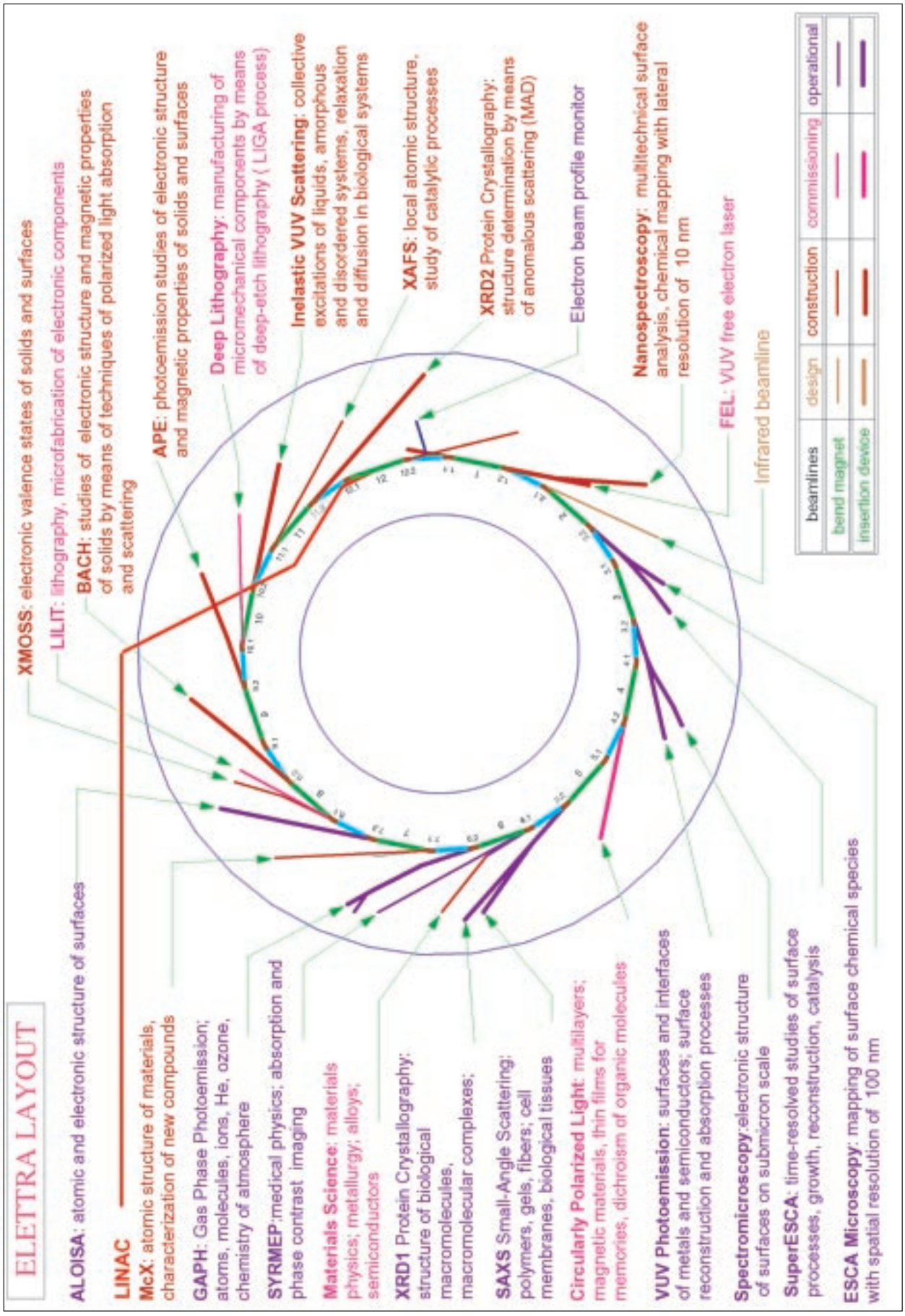
ELETTRA LAYOUT
XMOSS: electronic valence states of solids and surfaces
LILIT: lithography, microfabrication of electronic components
BACH: studies of electronic structure and magnetic properties of solids by means of techniques of polarized light absorption and scattering
APE: photoemission studies of electronic structure and magnetic properties of solids and surfaces
Deep Lithography: manufacturing of micromechanical components by means of deep-etch lithography (LIGA process)
Inelastic VUV Scattering: collective excitations of liquids, amorphous and disordered systems, relaxation and diffusion in biological systems
XAFS: local atomic structure, study of catalytic processes
XRD2 Protein Crystallography: structure determination by means of anomalous scattering (MAD)
Electron beam profile monitor
Nanospectroscopy: multitechnical surface analysis, chemical mapping with lateral resolution of 10 nm
FEL: VUV free electron laser
Infrared beamline
ALOISA: atomic and electronic structure of surfaces
LINAC
McX: atomic structure of materials, characterization of new compounds
GAPH: Gas Phase Photoemission; atoms, molecules, ions, He, ozone, chemistry of atmosphere
SYRMEP:medical physics; absorption and phase contrast imaging
Materials Science: materials physics; metallurgy; alloys; semiconductors
XRD1 Protein Crystallography: structure of biological macromolecules, macromolecular complexes;
SAXS Small-Angle Scattering: polymers, gels, fibers; cell membranes, biological tissues
Circularly Polarized Light: multilayers; magnetic materials, thin films for memories, dichroism of organic molecules
VUV Photoemission: surfaces and interfaces of metals and semiconductors; surface reconstruction and absorption processes
Spectromicroscopy:electronic structure of surfaces on submicron scale
SuperESCA: time-resolved studies of surface processes, growth, reconstruction, catalysis
ESCA Microscopy: mapping of surface chemical species with spatial resolution of 100 nm
beamlines
design
construction
commissioning
operational
bend magnet
insertion device

STATUS OF EXPERIMENTS

(updated August 31st, 2000)

USERS	
Italy	140
European Union	207
Others	42
TOTAL	**389**

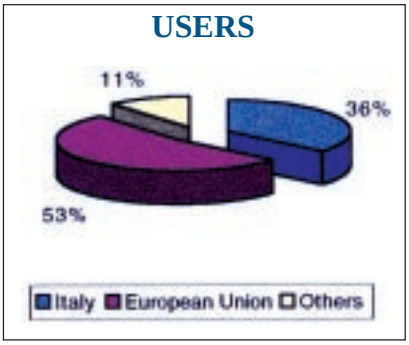

SHIFTS USED	
Experiments of General Users	1138
Experiments of Research Teams	833
TOTAL	**1971**

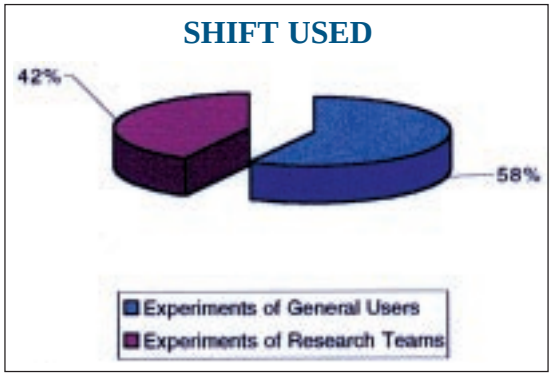

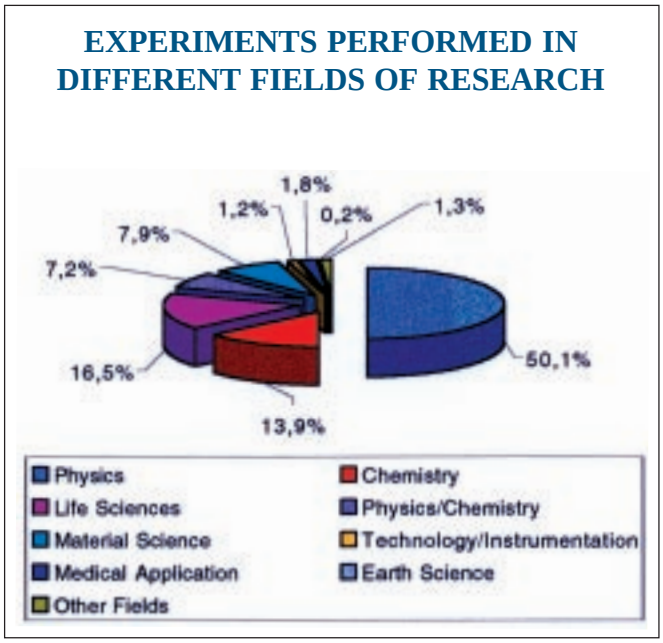

EXPERIMENTS PERFORMED IN DIFFERENT FIELDS OF RESEARCH		
Research Fields	**n. shifts**	**%**
Physics	988	50,1
Chemistry	273	13,9
Life Sciences	325	16,5
Physics/Chemistry	141	7,2
Material Science	156	7,9
Technology/Instrumentation	24	1,2
Medical Application	36	1,8
Earth Science	3	0,2
Other Fields	25	1,3
TOTAL	**1971**	**100,0**

LABORATORY STAFF

	scientists and researchers	technical personnel	administrative and clerical personnel	TOTAL
ACCELERATOR AND TECHNICAL SERVICES SECTOR	17	63	3	**83**
EXPERIMENTS SECTOR	32	28	6	**66**
GENERAL SERVICES	0	27	12	**39**
ADMINISTRATION	0	4	26	**30**
SINCROTRONE TRIESTE	**49**	**122**	**47**	**218**

STAFF DISTRIBUTION PER SECTOR

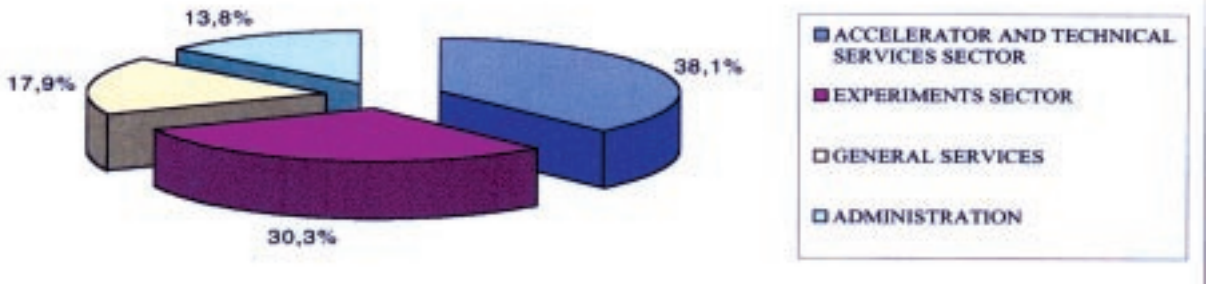

STAFF DISTRIBUTION PER PROFESSIONAL STATUS

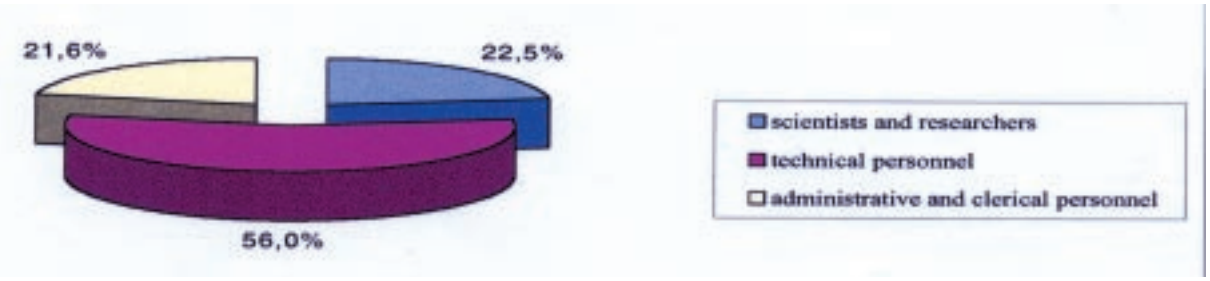

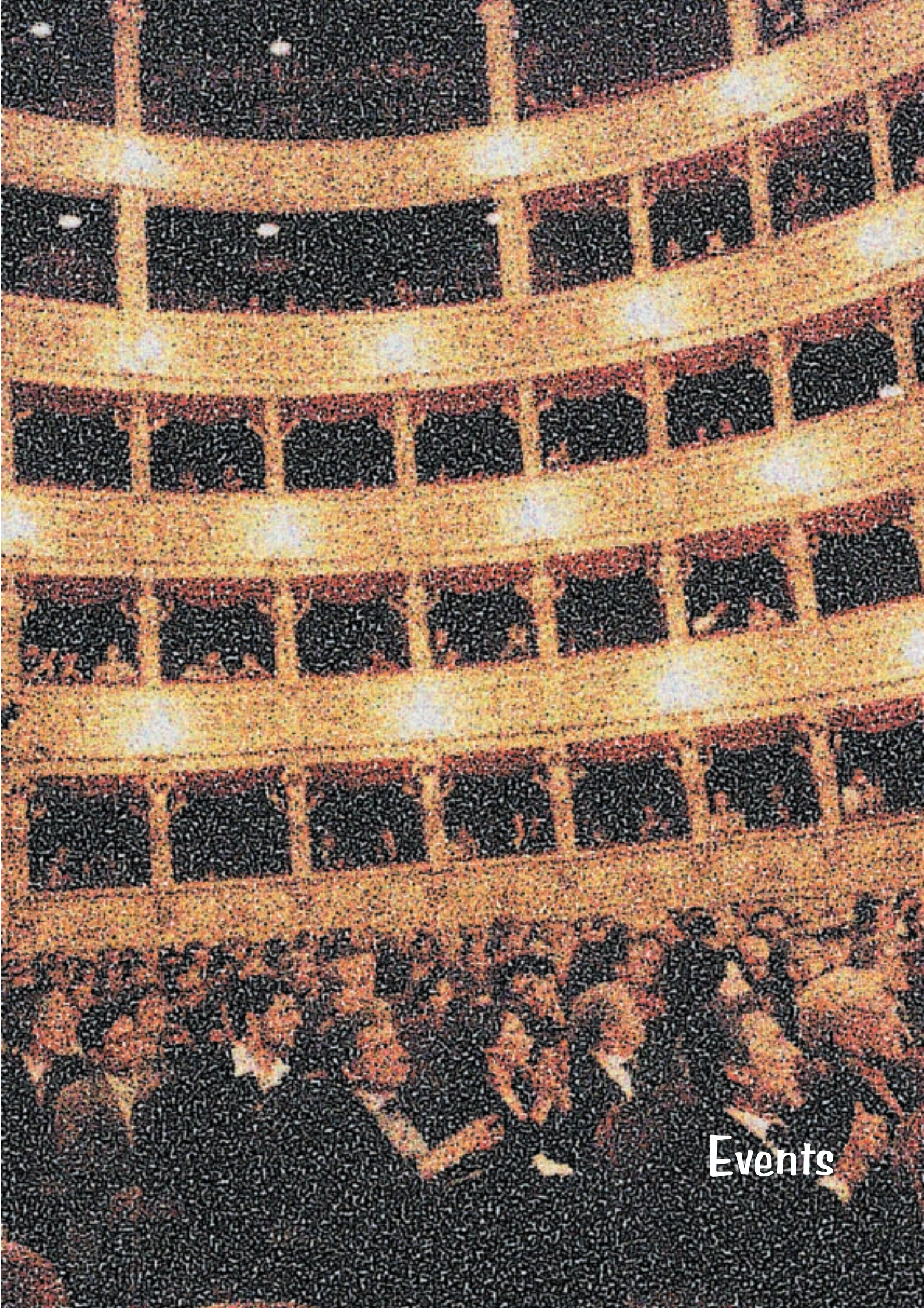

Events

Events

ICALEPCS '99

D. Bulfone,
Sincrotrone Trieste, Italy

The seventh biennial International Conference on Accelerator and Large Experimental Physics Control Systems (ICALEPCS'99), was organized by Sincrotrone Trieste. It took place from the 4th to the 8th of October 1999 at the "Stazione Marittima", a building recently restored as the Congress Center of the city of Trieste. ICALEPCS'99 was co-organised by the European Physical Society's (EPS) Interdivisional Group on Experimental Physics Control Systems (EPCS) and the Istituto Nazionale di Fisica Nucleare (INFN). The International Scientific Advisory Committee was chaired by D. Bulfone of Sincrotrone Trieste and A. Daneels of CERN. Almost 400 control specialists from 32 different countries covering Africa, America, Asia and Europe (figure 1) and representing 116 organisations (scientific institutes and industries) came together to exchange their views on the latest developments and new trends in control systems for accelerators and large Experimental Physics facilities. In the spirit of extending participation to the Conference, 38 participants coming from industrially emerging nations were given financial support to partially/totally cover participation expenses.

14 invited and 40 normal oral talks were given. 162 posters were presented during the three poster sessions. The distribution of the contributions submitted for the Conference Proceedings by origin world-wide is shown in figure 2.

The scientific and technical programme of ICALEPCS'99 covered the field of controls of particle accelerators, detectors, telescopes, nuclear fusion devices, nuclear reactors, etc. Traditionally dominated by the particle accelerators, ICALEPCS'99 saw many contributions also from the plasma physics, astronomical and particle detectors community. All aspects - hardware and software - of Experimental Physics control systems were considered. ICALEPCS'99 concentrated more specifically on how controls can contribute to the overall success of an Experimental Physics project. With this objective in mind, different technology and engineering issues were covered. State-of-the-art software and hardware technology were reviewed in terms of the possibilities they offer to deal with systems of increasing complexity and sophistication within restricted budgets and human resources.

Two pre-Conference workshops on EPICS and SOSH (SOftware SHaring) also took place within the scope of ICALEPCS'99. The Conference Industrial Programme included an industrial exhibition and parallel sessions for topical industrial seminars on state-of-the-art developments in technology that were of relevance to the subjects handled during the Conference. It saw the participation of some of the most distinguished companies in the field of electronics, informatics, networks and automation.

A Local Organizing Committee mainly formed by Sincrotrone Trieste staff and "the office" company endorsed the local organisation. ICALEPCS'99 benefited from the support of a number of sponsors. The main sponsors were Hewlett-Packard, the European Commission - DG XII, Telecom Italia, the Abdus Salam International Centre for Theoretical Physics (ICTP), Sincrotrone Trieste, Friul Computer, NT Nuove Tecnologie, Assicurazioni Generali, Banca Commerciale Italiana, Istituto Nazionale di Fisica Nucleare (INFN).

The ICALEPCS'99 Proceedings have been published in book (ISBN 88-87992-00-2) and CD-ROM (ISBN 88-87992-01-0) form. They are also available on the WWW at http://www.elettra.trieste.it/ICALEPCS99.

ICALEPCS (4-8 OCT. 1999)

Conference participants and ELETTRA staff in the Hall of the "Stazione Marittima"

Presentations at the "Stazione Marittima" of Trieste

ELETTRA staff at the "Stazione Marittima"

The concert at the town theatre "G. Verdi" organized for the Conference participants

Closing dinner at the "Villa Manin"

VII USERS' MEETING (29-30 Nov. 1999)

A Presentation held by ELETTRA Managing Director Massimo Altarelli

ELETTRA staff at the Conference dinner

The cake celebrating the Event

Visit of EUSJA Journalists

17 December 1999
Massimo Altarelli among EUSJA Journalists (European Union of Scientific Journalists' Associations) visiting ELETTRA during "ERA 2000" Exhibition

AREA Science Park

a world for research and innovation

AREA Science Park of Trieste is one of the main multi-sector science and technology parks in Europe: nearly 1400 specialised people work in more than 60 national and international research and hi-tech organizations which include public and private R&D labs, branch offices, innovative enterprises, training and educational centres. Their activities refer to a wide number of sectors, such as biotechnology, biomedical technologies, physics and new materials, electronics and electro-optics, informatics and multimedia systems, telematics and communication, environmental technologies.

Current contracts, where knowledge and market meet, concern chemical, pharmaceutical, automobile, environment food and space industries.

AREA Science Park holds the headquarters and the premises of some international excellence centres: among them the Sincrotrone Trieste, the company that manages the synchrotron radiation laboratory ELETTRA, stands out as one of the most advanced companies in the sector of research on materials.

Sincrotrone Trieste facilitates the access and the use of the ELETTRA scientific facilities to AREA Science Park tenants and its associates.

AREA Science Park is managed by a non-profit public consortium, Consorzio per l'AREA di ricerca, that is strongly committed to promote industrial research and market-oriented technologies, disseminate technological innovation through a close research-industry interaction and support the creation of innovative start-up companies. Its commitments also include financial support for research and educational projects, marketing, administrative and technical assistance, information/telematic services and promotional activities.

AREA
SciencePark

AREA Science Park
Padriciano 99, 34012 Trieste
Phone (39) 040 375 111 Fax (39) 040 226698
http://www.area.trieste.it
e-mail: info@area.trieste.it